UNIVERSIDADE
DA CORUÑA

E.T.S. DE INGENIERÍA DE
CAMINOS, CANALES Y PUERTOS

E.T.S. DE ENXEÑERÍA DE
CAMIÑOS, CANAIS E PORTOS

PROYECTO TÉCNICO

PROXECTO TÉCNICO

TITLE:

STUDY OF OPERATING CYCLES FOR UNDERGROUND HYDROGEN STORAGE IN SALT CAVERNS

AUTHOR:

FRANCISCO FIGUEIRAS VELO

DIRECTORS:

Dr. MANUEL ANDRÉS SOAGE QUINTÁNS
Dr. IGNASI COLOMINAS EZPONDA

DATE:

JULY 2024

Study of Operating Cycles for Underground Hydrogen Storage in Salt Caverns

Francisco Figueiras Velo

July 2024

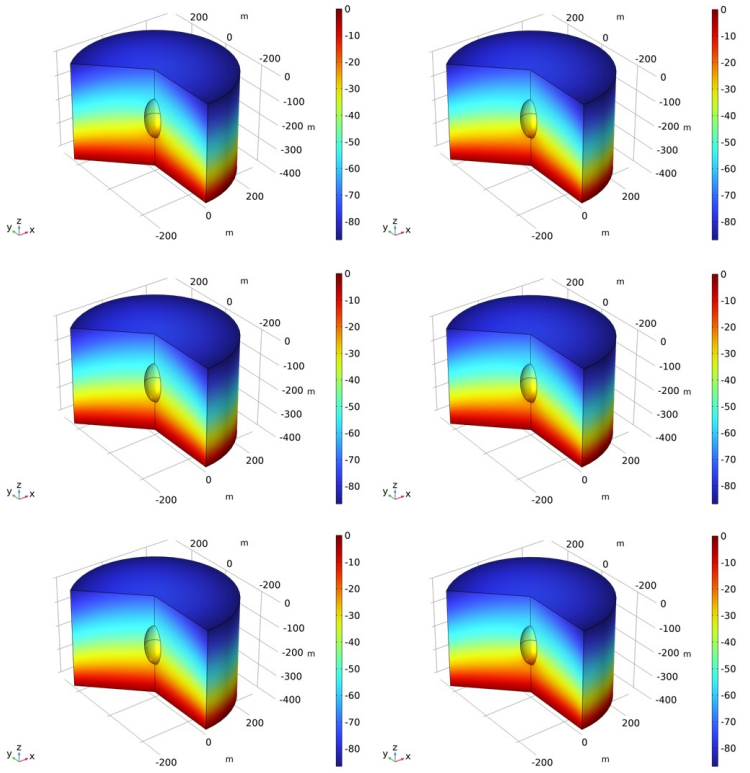

UNIVERSIDADE DA CORUÑA

Dedicado a Milagros, Juan Carlos, Carlos e Antía

Contents

List of Figures

List of Tables

Acknowledgements

I would like to thank my family and friends for their support during my college years. I would like to emphasize the role of my family, since these have not been the easiest years. I would also like to thank each and every one of my classmates for the many years and adverse moments experienced.

For the last, but not least, I would like to thank the Universidade da Coruña (UDC) and the Escola Técnica Superior de Enxeñeiros de Camiños, Canais e Portos (ETSECCP) of A Coruña for the training provided and the Grupo de Métodos Numéricos en Ingeniería (GMNI) for the opportunity to carry out this project. In particular, I would like to thank my teachers Andrés Soage and Ignasi Colominas for all the explanations and corrections they were able to give me.

Finally, to you, thank you for investing some of your time to enjoy this project, because at the end of the day, time is the most valuable thing we have.

This project has been funded by the following institutions:

- Spanish Government (FEDER and EU Next Generation funds): "Strategic projects oriented to the ecological and digital transition" "Plan de Recuperación, Transformación y Resiliencia" [TED2021-129991B-C31, TED2021-129805B-100].
- Spanish Government through FEDER funds of the European Union: grants for "Knowledge generation projects" [PID2021-125447OB-I00].
- Ministry of Universities of the Spanish Government (grant: Subsidies to Public Universities Research for the Requalification of the Spanish University System, "Margarita Salas" Grants Modality for the Training of Young Doctors, RD 289/2021 of April 20).
- Xunta de Galicia through "Grants for the consolidation and structuring of competitive research units of the Galician University System - Competitive reference group" [ED431C 2022/06].
- Universidade da Coruña and Fundación de la Ingeniería Civil de Galicia.

Abstract

The idea of using hydrogen as a source of energy is growing nowadays with the different initiatives adopted for the decarbonisation of the economy. Among the different procedures for obtaining hydrogen, the generation by hydrolysis of water using electricity supplied by renewable energy sources, also known as 'green hydrogen', stands out, which can contribute to changing the global energy model, particularly in transport.

Underground hydrogen storage can become a viable option compared to the use of above-ground metallic tanks, due to the permeability problems caused by the embrittlement of metallic structures in the presence of hydrogen, in addition to the safety challenges in storage and operations.

In this project, the conditioning and creation of salt caverns is being studied. These can be created by adapting galleries in disused salt mines or by building them from the surface; this is a possibility due to the low permeability of halite (salt rock). It is expected to efficiently confine hydrogen without leakage.

The research line presented here studies the structural stability of this type of storage facility, focusing on the hydrogen loading and unloading operating phases in cycles that may be very short (in the order of hours or days), throughout the 30-year lifetime of the operation. The operating cycles are composed of four different phases, arranged as follows: charging phase, holding phase at maximum pressure or working pressure, discharging phase, and holding phase at minimum pressure or cushion gas pressure. Currently, there is no generalised idea of the ideal duration of the phases that make up the operating cycles in order to obtain greater efficiency and safety in the cavern.

In this study, the influence of these cycles on the stability of the cavern has been analysed by means of numerical simulation, focusing on the duration times of each of the phases that make up the cavern. To this end, a series of numerical tests have been carried out, studying the weight of each of the phases of the operating cycle on the stability of the cavern.

Resumo

A idea de empregar hidróxeno como fonte de enerxía, está crecendo nos nosos días coas diferentes iniciativas adoptadas para a descarbonización da economía. Entre os diferentes procedementos de obtención destaca a xeración por hidrólise da auga mediante electricidade suministrada por fontes de enerxía renovables, tamén denominado "hidróxeno verde", o cal pode contribuir a cambiar o modelo enerxético mundial, en particular no transporte.

O almacenamento subterráneo de hidróxeno pódese convertir nunha opción viable fronte ó emprego de tanques metálicos en superficie, debido ós problemas de permeabilidade por fraxilización que presentan as estructuras metálicas fronte ao hidróxeno, ao que se unen os retos de seguridade no almacenamento e nas operacións.

Neste proyecto, estúdase o acondicionamento e creación de cavernas salinas, as cales poden orixinarse adaptando galerías de minas de sal en desuso ou executándoas dende a superficie; isto é unha posibilidade debido á baixa permeabilidade que presenta a halita (rocha de sal). Espérase que permita confinar de xeito eficiente o hidróxeno sen producirse filtracións.

A liña de investigación que se presenta estuda a estabilidade estructural deste tipo de almacenamento, centrándose nas fases de operación de carga e descarga de hidróxeno en ciclos que poden ser moi curtos (da orde de horas ou días), ao longo dos 30 anos de vida útil da explotación. Os ciclos de operación compóñense de catro fases diferentes, ordeadas do seguinte xeito: fase de carga, fase de mantemento a presión máxima ou presión de traballo, fase de descarga, e fase de mantemento a presión mínima ou presión de gas colchón. Actualmente, non existe unha idea xeralizada de cál é a duración ideal das fases que compoñen os ciclos de operación para obter maior eficiencia e seguridade na caverna.

Neste estudo, analizouse mediante simulación numérica, a influencia na estabilidade da caverna de ditos ciclos centrándonos nos tempos de duración de cada unha das fases que o compoñen. Para isto leváronse a cabo unha serie de ensaios numéricos, estudando o peso que presenta cada unha das fases do ciclo operativo na estabilidade da caverna.

Resumen

La idea de emplear hidrógeno como fuente de energía, está creciendo en nuestros días con las diferentes iniciativas adoptadas para la descarbonización de la economía. Entre los diferentes procedimientos de obtención destaca la generación por hidrólisis del agua mediante electricidad suministrada por fuentes de energía renovables, también denominado "hidrógeno verde", el cual puede contribuir a cambiar el modelo energético mundial, en particular en el transporte.

El almacenamiento subterráneo de hidrógeno se puede convertir en una opción viable frente al empleo de tanques metálicos en superficie, debido a problemas de permeabilidad por fragilización que presentan las estructuras metálicas frente al hidrógeno, a lo que se unen los retos de seguridad en el almacenamiento y en las operaciones.

En este proyecto, se estudia el acondicionamiento y creación de cavernas salinas, las cuales pueden originarse adaptando galerías de minas de sal en desuso o ejecutándolas desde la superficie; esto es una posibilidad debido a la baja permeabilidad que presenta la halita (roca de sal). Se espera que permita confinar de manera eficiente el hidrógeno sin producirse filtraciones.

La línea de investigación que se presenta estudia la estabilidad estructural de este tipo de almacenamiento, centrándose en las fases de operación de carga y descarga de hidrógeno en ciclos que pueden ser muy cortos (del orden de horas o días), a lo largo de los 30 años de vida útil de la explotación. Los ciclos de operación se componen de cuatro fases diferentes, ordenadas de la siguiente manera: fase de carga, fase de mantenimiento a presión máxima o presión de trabajo, fase de descarga, y fase de mantenimiento a presión mínima o presión de gas colchón. Actualmente, no existe una idea generalizada de cuál es la duración ideal de las fases que componen los ciclos de operación para obtener mayor eficiencia y seguridad en la caverna.

En este estudio, se ha analizado mediante simulación numérica, la influencia en la estabilidad de la caverna de dichos ciclos centrándonos en los tiempos de duración de cada una de las fases que lo componen. Para ello se han llevado a cabo una serie de ensayos numéricos, estudiando el peso que presenta cada una de las fases del ciclo operativo en la estabilidad de la caverna.

Chapter 1

Introduction

1.1 Hydrogen as energy source

Around 1500, Paracelsus observed that when iron filings were added to sulphuric acid, they gave off bubbles that were flammable. However, he did not know that this was a chemical element that had not been described at the time. In 1671, Robert Boyle carried out other tests in which, while conducting experiments between iron ingots and dilute acids, Boyle inadvertently created hydrogen gas; but he only knew it as "inflammable air". Under normal conditions (temperature: 25 °C; pressure: 1 atm), hydrogen is an odourless, colourless and highly flammable gas.

It was not until 1766 that Henry Cavendish first described hydrogen as a chemical element [Cavendish, 1766]; he also showed that hydrogen, in combination with oxygen, forms water. In 1783, Antoine Lavoisier named it hydrogen, or "water generator" (from hydro, water, and genos, generator). Later, in 1931, Harold Urey discovered deuterium. In 1934, Ernest Rutherford and his colleagues first produced tritium from deuterium [Suárez Alcántara, 2019].

Hydrogen is the most abundant element on Universe, but less than 1% is present as molecular hydrogen gas H_2 on Earth. The overwhelming majority is chemically bound as H_2O in water and some is bound to liquid or gaseous hydrocarbons. The clean way to produce hydrogen from water is to use renewable sources of energy in combination with photovoltaic cells and water electrolysis [Schlapbach and Züttel, 2001].

Hydrogen is likely to be the synthetic fuel of the future [Alsunousi and Kayabasi, 2024] because of its high calorific value [Olabi et al., 2021], Table 1.1, and the possibility of using hydrogen produced from renewable energies in a closed cycle [Jeje et al., 2024]. However, just as fossil fuels ushered in the industrial age, hydrogen will usher in an economic and technical revolution. Once investments in renewable energy production have been made, humans will be able to benefit from an environmentally clean energy economy based on hydrogen.

Hydrogen	Natural gas	Methane	Petrol	Coal
120 - 142	42 - 55	50 - 55	44 - 46	24

Table 1.1: *Comparison of calorific value obtained from different sources of energy in MJ/kg. Source: [WNA, 2020].*

The concept of a "Hydrogen Economy" (HE) originated in the early 1970s, as response to the first oil crisis [for Hydrogen and Technologies, 2003]. The Australian chemist John Bockris first used the phrase "Hydrogen Economy" [Bockris, 2013] and the first World Hydrogen Conference [Pangborn and Gregory, 1976] in 1976 identified hydrogen as a clean energy carrier for the future. After two decades of slow progress, the concept was re-launched at the end of the millennium in response to the increasing social concerns about global warming. This historical evolution shows that HE has never been a "first choice" but rather a response forced by the environmental and supplying concerns generated by the current "Fossil Fuels Economy" (FFE). Consequently, the strategy for the implementation of the HE needs to be adapted to the decay of the FFE in order to bridge the gap existing between both of them [Moliner et al., 2016].

Hydrogen will be stored in various forms depending on the application. We currently know of several efficient and safe ways to store hydrogen such as geological, liquified, or compressed storage. However, there are many other potential new materials and methods for storing hydrogen [Morris et al., 2019]. The challenge for materials science is to better understand the electronic behaviour of hydrogen interaction with other elements and especially with metals.

1.2 Hydrogen storage

Hydrogen has a very ambivalent behaviour to other elements, it occurs as anion (H^-) or cation (H^+) in ionic compounds; it participates with its electron to form covalent bonds e.g. with carbon; and it can even behave like a metal and form alloys at ambient temperature.

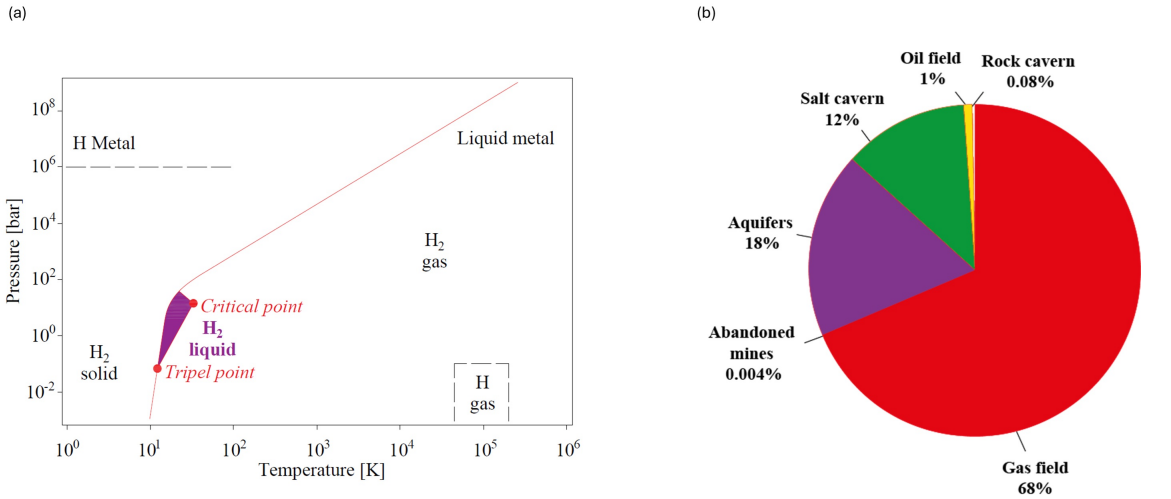

Figure 1.1: *Hydrogen phase diagram (a) and underground storage of gas in order of volume in Europe (b). Self-made figure based on [Züttel, 2004].*

The hydrogen molecule H_2 can be found in various forms depending on the temperature and the pressure, which are shown in the phase diagram at Figure 1.1. At low temperatures hydrogen is a solid with a density of 70.6 kg/m^3 at -262°C and is a gas at higher temperatures with a density of 0.089886 kg/m^3 at 0°C and a pressure of 0.1 MPa. A

small zone starting at the triple point and ending at the critical point exhibits the liquid hydrogen with a density of 70.8 kg/m^3 at -253°C [Weast, 1976]. At ambient temperature (298.15 K) hydrogen is a gas and can be described by the Van der Waals equation:

$$p(V) = \frac{nRT}{V - nb} - a \times \frac{n^2}{V^2} \tag{1.1}$$

where p is the gas pressure, V the volume, T the absolute temperature, n the number of moles, R the gas constant (R=8.314 J·K^{-1}·mol^{-1}), a is the dipole interaction or repulsion constant (a=2.476×10^{-2} m^6·Pa·mol^{-2}) and b is the volume occupied by the hydrogen molecules (b=2.661×10^{-5} m^3·mol^{-1}) [Weast, 1976]. The strong repulsion interaction between hydrogen molecules is responsible for the low critical temperature (T$_c$=33 K) of hydrogen gas. Hydrogen storage basically implies the reduction of the enormous volume of the hydrogen gas; 1 kg of hydrogen at ambient temperature and atmospheric pressure takes a volume of 11 m^3. In order to increase the hydrogen density in a storage system, work must either be applied to compress hydrogen, or the temperature has to be decreased below the critical temperature, or finally, the repulsion has to be reduced by the interaction of hydrogen with another material. The second important criterion for a hydrogen storage system is the reversibility of the hydrogen uptake and release [Züttel, 2004].

In terms of storage options, dense natural gas pipeline networks including integrated gas storages exist in Europe and other regions of the world. In order of volume, Figure 1.1, these gas storages in underground geological formations are almost exclusively located in depleted fields, aquifer formations or artificially constructed salt caverns. This experience can be applied to the selection of the appropriate storage typology for hydrogen, taking into account its particular characteristics.

1.2.1 Types of storage

A number of factors limit the maximum depth and pressure desirable for underground storage, including the costs of drilling wells or sinking shafts, the cost of compression, and the geothermal gradient, because high storage temperatures partially offset the volumetric efficiency gained by greater pressure [Foh et al., 1979]. Facilities for underground storage [Tarkowski, 2019] fall into two categories:

- Porous media storage [Lord et al., 2014], in which the gas occupies the naturally occurring pore space between mineral grains or crystals in sandstones or porous carbonates [Panfilov, 2010]. Here, we will treat as such both aquifers and depleted fields.

- Cavern storage [Thiyagarajan et al., 2022], in which the gas is contained in excavated or solution-mined cavities in dense rock. Here, we will treat as such salt caverns [Valle-Falcones et al., 2022], conventionally mined rock caverns and abandoned conventional mines.

Salt caverns

Salt caverns are artificially created cavities built in salt deposits. They are suitable for the storage of liquid hydrocarbons and in particular for gases under high pressure. Large amounts of gas can safely be stored due to large geometrical volumes and high storage pressures. Depending on the cavern depth, pressures of 20 MPa and above are common. Geometrical volumes reaching up to more than 1,000,000 m^3 can be constructed. The special properties of rock salt guarantee the long term stability and gas tightness of the cavities, when operated within suitable pressure ranges.

In terms of investment costs, about 28,000,000 € are estimated for the construction of a hydrogen storage cavern with about 500,000 m^3 of geometrical volume, in a top depth of about 1,000 m. Compared to other underground excavations very low specific construction costs are achieved because creation and operation of the caverns is done from above ground through only one single well bore, which is equipped with special piping and equipment. No technical installations are required underground except for this well.

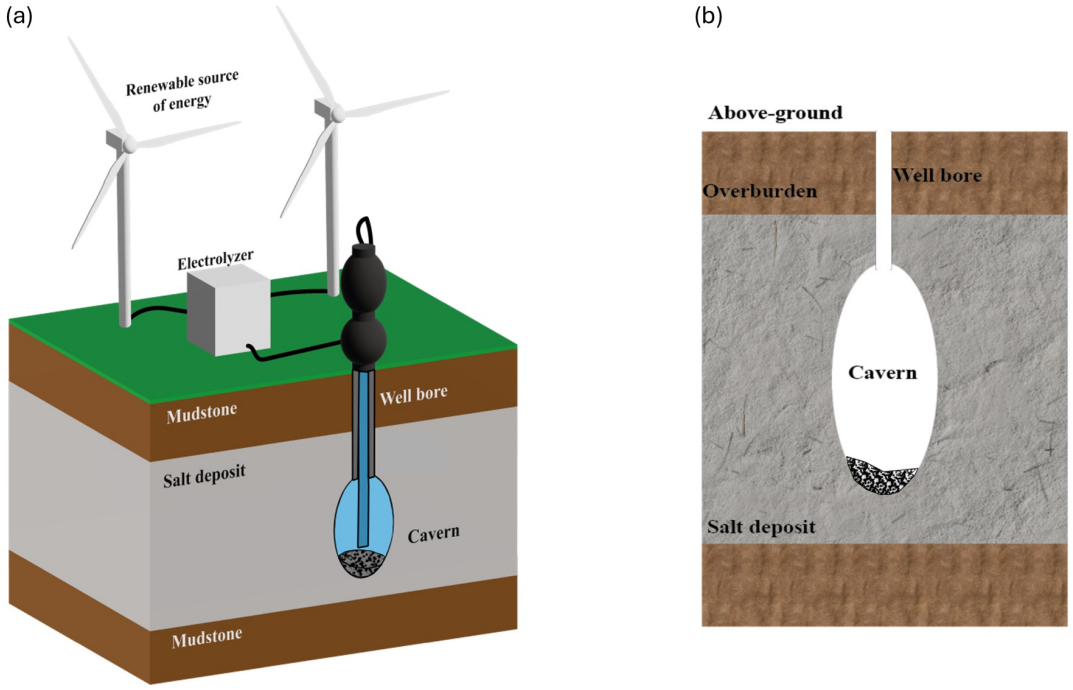

Figure 1.2: *Representation of a ellipsoidal salt cavern underground storage, where we can see a scheme of the "green hydrogen" production (a) and the rock salt cavern cross section (b). Self-made figures.*

Description of technology

Salt caverns are gas tight due to unique properties of the rock salt. Additionally, the salt pillars with large widths/thicknesses beneath, above and below the cavern respectively, which are required for the rock mechanical stability of the host rock, combine this gas tightness with thick layers of sealing salt, Figure 1.2.

Rock salt deposits can be structured in salt domes, salt diapirs and bedded salt. Depending on its occurrence the salt may be contaminated with insolubles, however, in

general this will not impair its tightness. Rock salt is for several reasons an ideal host rock for high pressure gas caverns:

- Tightness of rock salt for high pressure gases.
- Ability to construct large, unlined caverns.
- High storage pressures.
- Low specific costs due to construction completely from surface.

Applicable storage pressures depend on the cavern depth, operational scheme and range roughly between 80% and 30% of the lithostatic rock pressure [Ozarslan, 2012]. At a common cavern top depth of 1,000 m, this corresponds to a maximum pressure of some 18 MPa and a minimum pressure of about 6.5 MPa.

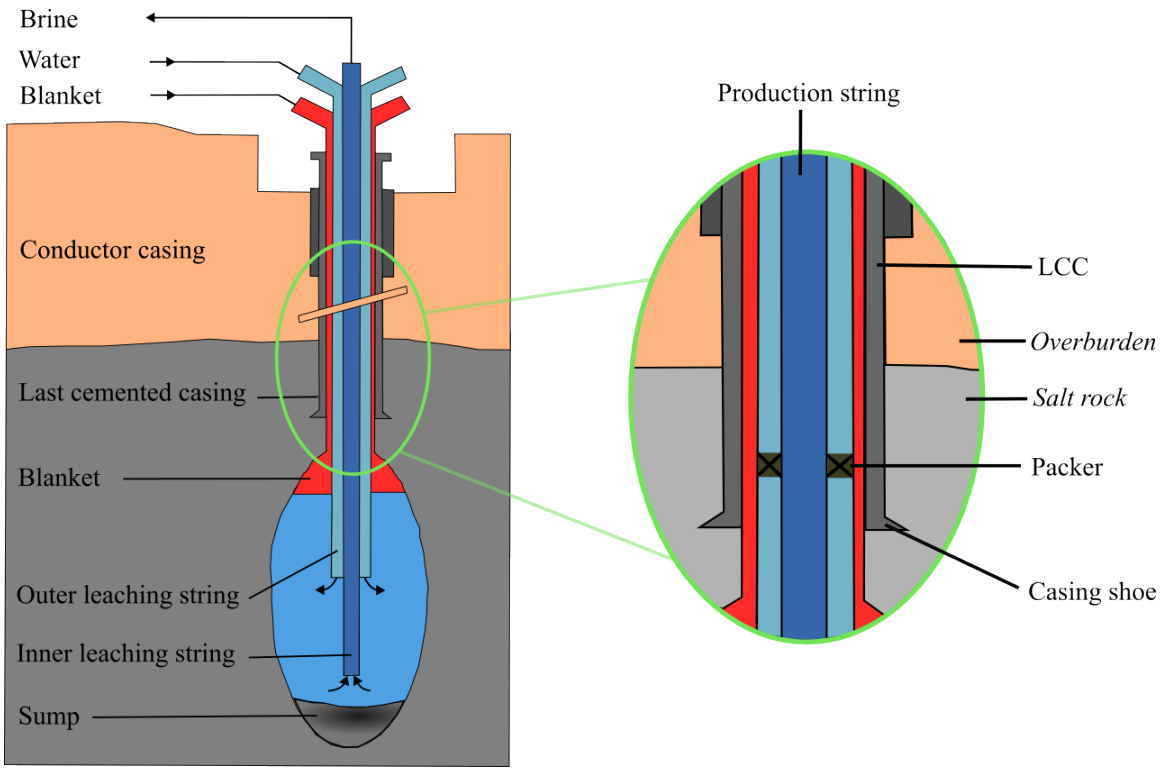

Figure 1.3: *Salt cavern with installed leaching string and blanket during leaching. Self-made figure based on [Arnold and Sitz, 1984].*

Construction

At first, a well section is each drilled and prepared for the conductor casing and the surface casing. The void between casing and rock and in between the casings is cemented to the surface [Ugarte and Salehi, 2021]. These cemented casings provide safe conditions to drill the access to the salt formation which is envisaged for leaching the storage cavern. Then a final casing is installed and also cemented to surface. This piping reaches into the salt formation (last cemented casing, LCC) to isolate the salt deposit in the roof of the

interval which is considered for the leaching process, Figure 1.3. Two additional pipes (leaching strings) are then concentrically hanged in the well and fixed in the well head. The well section below the LCC is leached by injecting water through the inner one of these leaching tubings. Rock salt is then dissolved by water and the resulting brine is displaced from the cavern via the inner annulus [Crotogino, 2022]. During leaching a blanket medium which has lower density than brine or water (commonly nitrogen or oil) is injected through the annulus between outer tubing and LCC. This prevents the salt in the upper part of the cavern from being accidently leached and helps to control the leaching process and thereby guides the cavern geometry development.

The cavern shape is controlled at regular intervals by sonar surveys. It depends on measurement results, the leaching tubings depth, the flow direction and the blanket depth can be changed to optimize the leaching process and to keep the cavern within permitted dimensions.

Prior to gas operations the gas production string and other elements of the so-called gas completion and the debrining string are installed, Figure 1.3. During the first fill of the cavern, gas is injected through the annulus between the production and debrining string, and in parallel, brine is produced out of the cavern through the debrining string. The debrining string has to be pulled out of the cavern under gas pressure when the brine is completely displaced (snubbing), and prior to normal gas injection and withdrawal operations.

The construction period (drilling to commissioning) takes up to five years, depending on cavern volume and leaching rate.

Operating procedure

Gas caverns are normally operated by compression and decompression between a minimum and a maximum pressure. Thus the gas inventory can be divided into working gas, which can be withdrawn from the cavern during normal operation, and cushion gas which must remain in the cavern to ensure its stability. Besides the maximum and minimum cavern pressure, the salt cavern operations are mainly restricted by the maximum pressure change rate per unit time to ensure stability, and also by the maximum flow velocities inside the well. Furthermore, so called re-healing times at higher storage pressures [AbuAisha and Billiotte, 2021] are required subsequent to times of very low pressures.

During the cavern lifetime some brine will always remain at the bottom of the cavern, as we can see at Figure 1.3 left, and water will evaporate in to the gas and increase its moisture. Gas drying is therefore required depending on the latter use of the hydrogen. No degeneration of natural gas or hydrogen has been reported so far, therefore the rock salt can be assumed as inert [Lankof et al., 2022]. Consequently, gas cleaning is not required.

Experience

Natural gas has been successfully stored in salt caverns in Europe and USA since the 1970s. The experience from more than 300 salt caverns in Europe utilised for natural gas storages can be largely applied to hydrogen storage projects.

In the 1970s, town gas with hydrogen fractions larger than 50% was successfully stored

in reservoir storages and salt caverns. However, no issues about biological or chemical degradation or other issues are reported in literature.

To date, pure hydrogen has been stored in three caverns: in Teesside (UK) since 1972 and in two caverns in Texas (USA) since 1983, see Table 1.2. Practical experience in UK and USA hydrogen caverns has shown that hydrogen can also be safely stored in salt caverns for long periods of time.

	Clemens (USA)	**Moss Bluff (USA)**	**Teeside (UK)**
Geology	Domal salt	Domal salt	Bedded salt
Stored fluid	Hydrogen	Hydrogen	Hydrogen
Commissioned	1983	2007	1972
Volume [m^3]	580,000	566,000	3 x 70,000
Reference depth [m]	930	822	350
Pressure range [MPa]	7 - 13.5	5.5 - 15.2	4.5

Table 1.2: *Existing storage in salt caverns. Source: [Kruck and Rudolph, 2013].*

Characteristic and performance

The feasible geometrical volume of salt caverns depends mainly on the thickness of the salt formation. The volume may range typically from 150,000 to 800,000 m^3. Under optimal conditions in a huge salt dome volumes even above 1,000,000 m^3 have already been achieved.

Operating pressures depend primarily on the cavern depth. The maximum pressures range from 10 to 27 MPa, the minimum pressures from 3.5 to 9 MPa respectively (orders of magnitude only).

For a common cavern volume of 500,000 m^3 and a casing shoe, Figure 1.3, depth of 1,000 m a pressure range of 18 to 6 MPa is suitable, which results in a working gas capacity of 4,000,000 kg hydrogen (47,000,000 m^3) and a cushion gas of 2,200,000 kg (26,000,000 m^3).

Depending on the cavern pressure, size and production tubing injection and withdrawal rates of more than 130,000 m^3/h or 105,000 kg/h are common for single storage salt caverns.

Aquifers

Aquifers are porous and permeable rock formations containing fresh water or commonly brine in the pore space. Typically such permeable rock formations are sandstones or carbonate rocks. In order to be suitable for gas storage, the aquifer needs to be overlain by a layer of impermeable cap rock. Such a cap rock could be tight shale, salt or an anhydrite layer.

Because of the barely predictable efforts for exploration and the required number of wells it can be assumed that the costs associated with the development of a hydrogen storage in an aquifer represents much larger uncertainties than the cost estimates for hydrogen storage in salt caverns or depleted hydrocarbon fields. In most cases the costs are expected to be higher than for the two other cases.

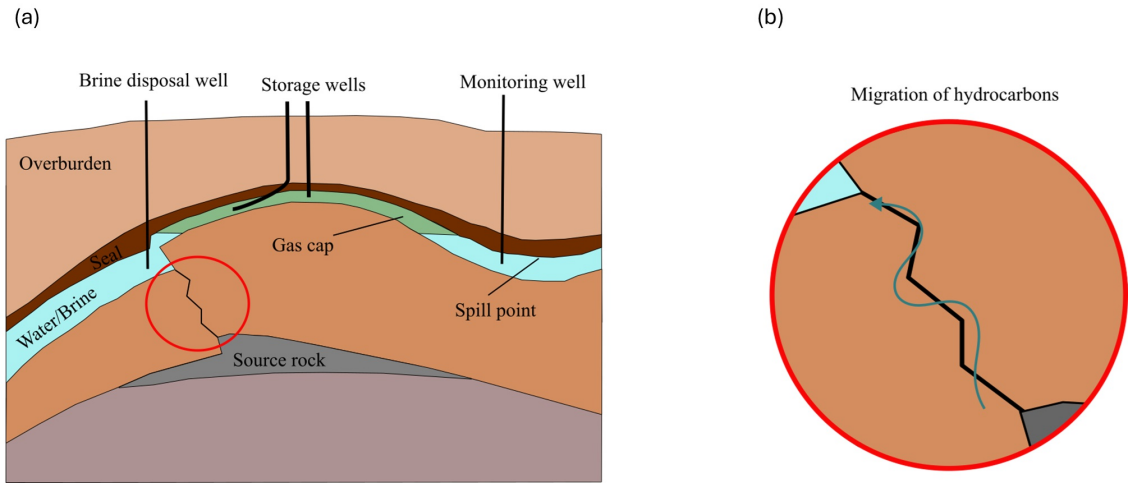

Figure 1.4: *Description of gas storage in an aquifer (a) and a schematic diagram showing a typical setup of a hydrocarbon reservoir (b). Self-made figures based on [Arnold and Sitz, 1984].*

Description of technology

To prevent the gas from rising upwards and migrating out of the storage, a 3D shape which is capable of containing the gas is required.

This "container" is known as a "geological trap", Figure 1.4. The size of the trap is defined by the spill point, which is the highest point where the structure is open to the connecting aquifer or the lowest point at which the storage is closed for the product.

In order to develop a gas storage within a suitable rock layer, a number of wells are drilled through the overlaying rock burden and the sealing caprock layer into the aquifer.

The wells are used to inject the storage medium into the pore space, which is initially filled with water or brine. Therefore, the capacity of the storage site is determined not only by the size of the container/trap and the porosity, but also by their distribution and therefore the amount of residual water that will remain in the pore space after gas is injected. The development of a suitable aquifer [Pfeiffer and Bauer, 2015] can take about four years.

Higher injection and withdrawal rates in aquifers can be achieved by using multiple injection/production wells or, sometimes, by using long horizontal wells, Figure 1.4. Nevertheless, low flow rates in aquifers are the reason this storage type is mainly used for seasonal storage, with only one annual storage cycle at steady injection and withdrawal rates.

Since the porosity of the reservoir and the behaviour of the liquid phase is the same for natural gas and hydrogen storage, differences between them can only arise from differences between natural gas and hydrogen itself.

Experience

Currently no data has been published of any storage of pure hydrogen in aquifers. Issues with biological and chemical reactions have to be investigated in order to apply these geological structures as hydrogen storage.

	Hähnlein (GER)	**Stenlille (DK)**
Geology	Late Tertiary II	Sandstone
Stored fluid	Natural Gas	Natural Gas
Commissioned	1960	1989
Volume [m^3]	-	-
Reference depth [m]	500	1,500
Pressure range [MPa]	3.9 - 5.3	15 - 17

Table 1.3: *Existing gas storage in aquifers. Source: [Kruck and Rudolph, 2013].*

Characteristic and performance

The applicable sizes of aquifers vary widely and enable storages volumes much larger than for salt caverns. The hydrogen is injected in the upper section of the aquifer structure, thus the storage has certain scalability of the utilised storage volume. The applied vertical extends and volume of the formation can therefore be increased successively. Nevertheless a certain gas volume must always be reached to avoid aspiration of formation water in the well bore.

Working gas capacities of aquifers for natural gas storage per storage site are in the order of hundred to thousand million cubic meters and could be in theory similar for hydrogen storage. However, the significant amount of unrecoverable gas which will remain in the formation is a vital problem when developing an aquifer storage.

Maximum gas withdrawal and injection rates per well depend on the rock permeability, the number of wells and the length of the well perforations as well as on volumetric extend and connectivity of the formation. Because of the higher mobility of hydrogen compared to natural gas the same or higher volumetric flow during injection and withdrawal are assumed to be feasible. High contents of water and impurities must be removed from the withdrawn gas [Talman, 2015], depending on the specific storage.

Depleted fields

Depleted oil and gas fields were filled with hydrocarbons in the past and a certain amount of these hydrocarbons have been produced (withdrawn). The advantages of depleted fields are that trap structures are well known from the time when the reservoir had been explored and tested and later when hydrocarbons were produced. Normally, the gas fields are not completely depleted and the remaining gas can be utilised as cushion gas. Furthermore, subsurface and surface installations already exist and may be used for later purposes. Hence, a conversion into underground gas storages may be possible with only limited exploration effort and investment as long as the above mentioned conditions are given. But this does not imply that all depleted fields are suitable for underground storage, especially not for hydrogen.

Description of technology

Conventional subsurface reservoirs hold hydrocarbons like oil or gas in geological traps. These geological traps consist normally of reservoir, seal and aquifer, see Figure 1.4.

The main element is the reservoir or the hydrocarbon accumulation, which is the container where the hydrocarbons are found in porous and permeable sediments or rocks. In typical reservoirs the hydrocarbons in the accumulation migrate from the source rock, underneath the reservoir, along geological pathways into the final reservoir.

The second element of the hydrocarbon trap is the seal, which covers the whole hydrocarbon reservoir. The top seals are often thick and tight shale horizons, tight, non-fractured carbonates or even tight salt layers.

The third part of the hydrocarbon trap is the aquifer underneath the reservoir. The saline formation waters provide in many cases the pressure support. This provides the full seal integrity; otherwise the hydrocarbons would penetrate the seal and would leak into the layers above the reservoir.

Construction

The simplest way for the construction of underground gas storages is the conversion of suitable depleted gas fields. Suitable fields need to fulfil certain prerequisites and need to provide certain subsurface properties to enable the successful storage and production of natural gas.

The available data and the understanding of the reservoir structure and behaviour demonstrate that the structure is large and capable enough to hold the gas in its porous and permeable horizons. Additionally the cover rock needs to separate the reservoir from shallower structures to prevent that gas can escape.

Operating procedure

To achieve proper withdrawal and injection rates of the wells, the reservoir zones encountered need to have good and connected porosities and high permeabilites. The reservoir should also be positioned in a certain depth to allow a wide pressure range for the applicable and aproved minimum and maximum injection and withdrawal pressures.

The performance and flexibility of the depleted fields used for underground storage can be improved if horizontal wells, which produce from large reservoir sections, are deployed for the injection and production.

As described for the aquifer storages a higher mobility of hydrogen can be assumed leading to similar or higher volumetric withdrawal and injection rates compared to natural gas storage. However, due to the low density of hydrogen this results in about one tenth of the mass flow of natural gas.

Experience

Natural gas is successfully stored in depleted reservoirs, which is the preferred method in Europe and across the world since the early 20th century due to the large storage capacities that can be realised. The first depleted gas field that was converted to an underground gas storage was a gas field in the Welland County, Ontario in Canada and started operation in 1915 [Bauer S. J. and Neal, 1997]. In 2008 there were 63 depleted fields present compared to 26 salt caverns sites (multiple caverns per site) and 22 aquifer storages in the EU area.

	Uelsen (GER)	**Rheden (GER)**
Geology	Sandstone	Dolomite
Stored fluid	Natural Gas	Natural Gas
Commissioned	1997	1993
Volume [m^3]	-	-
Reference depth [m]	1,500	1,900 - 2,100
Pressure range [MPa]	16.8	11 - 28

Table 1.4: *Existing gas storage in depleted fields. Source: [Kruck and Rudolph, 2013].*

Characteristic and performance

Depleted fields are commonly found in a depth range of several hundred meters to less than three-thousand meters. The average working gas volumes range between one million cubic meters to several thousand of cubic meters, at a minimum pressure regime between one megapascal to couple of megapascals up to maximum pressure regime of several tens megapascals.

The rates depend on the permeability and complexity of the storage formation and also the number and performance of the production wells depending on the specific site.

High contents of water and impurities must be removed from the withdrawn gas, depending on the specific storage. Therefore gas treatment processes need to be applied correspondingly.

Conventionally mined rock caverns

Conventionally mined rock caverns are underground cavities drifted using conventional mining techniques (shaft sinking, excavation of cavities by blasting or cutting). Mined rock caverns can be constructed in a certain range of geological formations. Those must allow the construction and operation of large, long term stable caverns. These formations need to be either widely intrinsically tight, which can be intensified by the existence or introduction of water. It could also be made tight by installing an engineered lining.

Rock caverns have been developed for the storage of liquid hydrocarbons like oil, gasoline and liquid petroleum gases. Most of these developments have been performed in Scandinavian countries, since they provide the suitable rock formations in large homogenous quantities. In a special application, a rock cavern has been used for a small sized high pressure natural gas storage in Sweden (Skallen), Figure 1.5, and a very large, but also very specific storage in Czechia (Haje) [Barták, 1999].

Description of technology

Rock caverns are drifted using mining methods. This means that they require one or more access drifts or shafts to deliver technical equipment, haul the excavated rock, transport personnel and enable the ventilation.

The geometry of the storage cavity has to take into consideration geological and geomechanical design criteria, and this determines the excavation method. Drifts with circular cross-sections can be drilled using full face tunnellers or by drilling and blasting.

Figure 1.5: *Rock cavern in Skallen (Sweden). Source: PV Magazine*

Gallery caverns are also excavated by drilling and blasting, but the material can be removed in some horizontal layers which enable the construction of higher caverns.

In general, the host rock must be strong enough to enable the construction of a selfsupporting cavern which is large enough to be economical. Rock bolts can be driven several metres into the rock during the construction of the cavern to prevent blocks of rock from falling of the roof. And shotcrete can be sprayed on to the cavern walls to stabilise unconsolidated rock [Glamheden and Curtis, 2006], and additional cement can be injected into the cavern walls if necessary via short boreholes.

For high pressure gas storages has to consider the tightness of the storage walls and additionally the tightness of the access shaft or ramp, which requires the installation of plugs as extra structures.

The host rock has to have a very low permeability to be able to operate the storage. The basis of rock mass has to be sufficiently tight to perform without making use of any of the additional sealing methods. It is also essential in such cases that there are no open fissures or faults near the planned underground cavity.

Experience

Projects for the storage of liquid hydrocarbons in unlined rock caverns have been pursued in the USA in particular, and in Europe (especially Scandinavia) since the 1950s. Some of the storages were affected by problems caused by bacterial contamination (foaming, disintegration, degeneration). There are currently no rock caverns constructed for the storage of hydrogen.

	Haje (CZ)	**Skallen (SWE)**
Geology	Granite	Gneiss
Stored fluid	Natural Gas	Natural Gas
Commissioned	1998	2004
Volume [m^3]	620,000	40,000
Reference depth [m]	950	115
Pressure range [MPa]	16.8	11 - 28

Table 1.5: *Existing gas storage in conventionally mined rock caverns. Source: [Kruck and Rudolph, 2013].*

Characteristic and performance

Rock caverns can reach large volumes (up to 1,000,000 m^3) if several galleries are drifted. Lined rock caverns have been realised with a volume of 40,000 m^3 each, while studies propose feasible volumes of up to 320,000 m^3 by combining several cylindrical caverns. It can withstand pressures of up to 23 MPa or even more. Furthermore, their very small minimum pressure requires only a small amount of cushion gas. Such a cavern would reach a working gas of 1,700,000 kg hydrogen (22,500,000 m^3) with only 200,000 kg (2,000,000 m^3) of cushion gas. Because lined rock caverns are less dependent on the host rock, pressure rates higher than for rock caverns and therefore more gas turnovers per year are feasible.

Since similar thermodynamic and rock mechanic limitations occur for salt and for lined rock caverns, a hydrogen mass flow of one tenth the natural gas mass can be assume. Therefore the possible hydrogen rate, related to the Skallen storage would be 3,600 kg/h.

Abandoned conventional mines

There are numerous abandoned conventional mines in various types of geological formations in Europe, that were not or only partially backfilled and which could, in theory, provide plenty of storage volume for gaseous media like hydrogen. These mines provide medium to large geometric volumes are often at depths between a few hundred metres to 1,000 metres or even deeper. This means that they are in general at a depth range suitable for the operating pressures required for hydrogen storage.

The storage option, abandoned mines, is very heterogeneous because of the different geology in which the mines were excavated and the different techniques that were applied to excavate the cavities. This should be done by considering the need to construct a sealing structure in the existing shafts. If necessary, the underground workings may be tightened.

Convert abandoned mines into storages could be associated with high risks because the tightness of the storage cannot be tested until all of the engineering work has been completed and the storage is gas filled. For this reason, in general, the integrity of most geological formations is questionable [Colas et al., 2023], which therefore rules out most potential candidates. Exceptions could be salt caverns whose conversion into hydrogen storages seems feasible, in the long term.

Description of technology

Because an existing mine is to be used, there is no way to influence the basic design of the mine body and the shafts any more. This makes it even more important to take great care in selecting a suitable mine for conversion into a gas storage. The following aspects must be taken into consideration during the selection process:

- The tunnelling and excavation method utilized should have caused as little damage as possible to the remaining rock mass.
- The use of milling, scraping or drilling tools is preferred for the drifting method to the use of drilling and blasting.
- Sealing the access drifts and shafts is expensive and every additional seal which has to be put into place increases the risk of an eventual leak.
- The mine must not exceed into adjoining rock formation which might have different rock mechanical properties or permeability.

During the conversion of the mine to a gas storage the seal of the production shafts and underground workings have to be installed. Pipes can be laid through the sealing structure for the gas operation [Arnold C. and T., 1998], although this is technically complicated and may represent another risk to the integrity of the structure.

When the mine is being filled for the first time, the air present after completion must somehow be replaced by the storage gas. To prevent the formation of a flammable or explosive mixture, the cavity can be flushed first with an inert gas, in this case N_2, to displace the oxygen before filling with hydrogen for the first time. Flushing is carried out under minimum pressure to use the smallest possible amount of gas.

Coal mines are also able to store gas. However, additionally to the volume of gas stored in the actual storage cavity, a large volume of additional gas can also be stored in the coal itself by sorption. In addition, coal constantly produces methane, and potentially other mine gases, depending on the storage pressure, and these gases will mix with the stored hydrogen.

Experience

The first storage of liquid hydrocarbons in abandoned mines took place in Sweden in 1947 - 1950, and although discussed subsequently for a number of different mines, has rarely actually been implemented since [Lu, 2010]. The Weeks Island salt mine in Louisiana (USA), which produced salt from 1902 to 1977 until mining continued in a neighbouring mine, was re-used as a crude oil storage [Bauer S. J. and Neal, 1997]. No abandoned mines have been used so far for the storage of pure hydrogen.

	Bernsdorf (GER)	**Norton Ohio (USA)**	**Leyden (USA)**
Geology	Potash	Limestone	Coal
Stored fluid	Natural Gas	Air	Natural Gas
Commissioned	1970	-	1961 - 1998
Volume [m^3]	40,000	10,990,000	5,100,000
Reference depth [m]	600	670	225
Pressure range [MPa]	1.2 - 3.6	5.5 - 11	1.7

Table 1.6: *Existing abandoned mine storages. Source: [Kruck and Rudolph, 2013].*

Characteristic and performance

Most of the discussed abandoned conventional mines provide very large geometric volumes. However, they cannot be altered to match the required dimensions.

They also provide low flexibility since the mine workings are not designed for dynamic pressure rates, but for static loads at ambient pressure. Additionally, the groundwater management or the water curtain technique reduces the feasible pressure rates and their bandwidth. The mines therefore require large cushion gas volumes and could probably perform best as seasonal storages.

The gas withdrawn from abandoned conventional mines will probably have a high water content due to groundwater management. Depending on the present host rock, also a degradation of hydrogen might occur which potentially leads to a loss of hydrogen and impurities from the products of biological or chemical reactions.

Pipe storage

Pipe storages are used to store natural gas and smooth out short-term demand peaks. The pipe storage built so far are not big enough to make any significant contribution to seasonal storage requirements.

The construction costs comprise mainly on the procurement costs for the steel pipes and the welding, as well as the earth moving work. The surface facilities largely are comprised of a compressor and the gas metering system because no gas treatment is required.

Because hydrogen pipelines, Figure 1.6, already exist and pipe storages have no significant differences to these pipelines, it is considered that storing hydrogen in pipe storages [Panfilov, 2016] is a soon achievable option.

Description of technology

The storage pipes are buried deep enough in the ground to enable the surface to be used, although this is subject to significant restrictions. The stability and the pressure range under which the storage can be operated are purely determined by the strength and thickness of the pipes.

The proportion of fixed costs is very small because it is only related to the surface facilities. Depending on how the storage is connected to the natural gas grid, the pipeline pressure could either define the minimum storage pressure or the gas could be produced from the storage at reduced pressure via a compressor.

Figure 1.6: *Pipe storage construction working. Source: Zürich Transport AG*

If large pressure rates occur during injection or withdrawal, this will change the temperature of the gas and the steel pipes and affect the length of the storage by thermal expansion. For this reason, the operation of a pipe storage involves maintaining a minimum pressure. It depends on the intended pressure range, it may be necessary to limit the length of the pipes or to enable the pipes to expand without damaging or hindering the operation.

No contamination or increase in the humidity of the gas in the storage is expected during standard operations. This means that no drying or purification equipment is required.

Experience

Natural gas pipe storages have widely been used since the 1980s primarily by municipal utilities for peak shaving on a weekly or daily basis. Some of these storages have been operating successfully for many decades.

There are no known pipe storages for storing hydrogen. However, hydrogen pipelines exist especially in chemical and petro industries.

	Urdorf (CH)	**Bocholt (GER)**	**Eymatt (CH)**
Geology	-	-	-
Stored fluid	Natural Gas	Natural Gas	Natural Gas
Commissioned	2012	2007	2007
Volume [m^3]	6,112	3,072	7,955
Reference depth [m]	-	-	-
Pressure range [MPa]	0.7 - 10	9	2.3 - 7

Table 1.7: *Existing pipe storages. Source: [Kruck and Rudolph, 2013].*

Characteristic and performance

The storage capacity of pipe storages is very small compared to other storage options. A maximum geometric volume of roughly 12,000 m^3 has been realised so far. Since the storage pipes are easily accessible, they can be extended by additional pipes after commissioning of the storage.

Due to very small minimum pressures, which can reach values of only 0.4 MPa, only little quantities of cushion gas is required. Working gas capacities of 42,000 kg hydrogen are feasible with only 4,200 kg cushion gas. Pipe storages provide a high flexibility and may reach injection and withdrawal rates of up to 90,000 m^3/h for natural gas which is in the same range as for salt caverns. Hydrogen rates of 7,400 kg/h appear to be feasible if the same pressure rate is.

With the given withdrawal rate the whole working gas may be withdrawn in just six hours. Therefore, storage pipes are commonly applied for peak shaving on a weekly or daily basis. As a matter of fact, they may have a very high number of turnovers per year, which helps to distribute the high specific construction costs to a large gas volume that might be stored in the pipes during the storages lifetime.

Another advantage is that no humidity or other impurities will accumulate in the stored hydrogen, since the gas is encapsulate by a technically designed surface.

Types of storage	Volume [m^3]	Reference depth [m]	Pressure range [MPa]	Production [kg/h]
Salt caverns	580,000	930	7 - 13.5	105,000
Aquifers	4,000,000	1,500	15 - 17	30,700
Depleted fields	1,000,000	1,500	16.5	40,400
Conventionally mined rock caverns	40,000	600	1 - 23	3,600
Abandoned conventional mines	135,000	600	1.24 - 5	3,600
Pipe storage	6,112	-	0.7 - 10	7,600

Table 1.8: *The information used in the present table is a sum of the data shown in previous tables. Source: [Kruck and Rudolph, 2013]*

1.3 Motivation and objectives

The objective of this Technical Project is to study the influence that hydrogen injection and withdrawal operations may have on underground storage facilities located in salt caverns.

The aim is to study stability, focusing on the displacements produced in the upper part of the cavern. This is due to the fact that injection/withdrawal operations as well as the construction of the cavern is carried out from this area.

Furthermore, due to the characteristics of the salt caverns and the location of the well, it is important to limit the maximum displacements in this area of the cavern. Crucial if we refer to hydrogen injection/extraction cycles. To this end, we will define a series of specific objectives to be met during the work:

1. Analysis of each of the phases that make up the operational cycle.
2. Verification of the influence of the duration of injection/extraction operations on stability.
3. Study of the cavern operating conditions for efficient hydrogen production.

1.4 State of art

Injection/extraction operations are an important part of the operation of any type of underground storage. A thorough study is needed to make the production of gases as efficient as possible while obtaining the highest yield. In the case of underground hydrogen storage there is no in-depth study on this topic.

The existing literature is mostly limited to specifying the operating cycles used to calculate the numerical models of the storage facilities without explaining their background; even so, there are studies that do advance this idea from different points, which are:

- Study of the ideal frequency (number of complete cycles per year) to operate the storage taking into account the mechanical response of the cavern to the stresses produced in the salt by the changes in pressures [Li et al., 2023].
- Study from the economic point of view, taking into account the maximum volumes that can be extracted without compromising the operability [Lysyy et al., 2021].
- Study of the gas flow, i.e., the importance of the injection and extraction flow rate is highlighted, as it is not the same throughout the useful life of the underground storage [Ershadnia et al., 2023].

It is worth mentioning that there is little literature that focuses entirely on the influence of the operating cycles of underground hydrogen storage in salt caverns, with resources occurring in the case of aquifers and depleted gas or oil reservoirs. The cycles used in the exploitation of underground reservoirs vary depending on the storage operator and the time of year, so no single configuration can be described as ideal. It depends on the energy demand requested by the market and also the type of field used for storage, an underground hydrogen storage project generally follows a cyclic operation with an alternate period of injection and withdrawal operations [Foh et al., 1979]. The possibility of more than one or additional cycles per year is very common during peak and fluctuating demand [Zivar et al., 2021].

The injection and production schedules can be derived from the supply and demand scenarios. The supply data is the hydrogen production rate from electrolysers that are powered by renewable resources, thereby has variability. Similarly, the demand scenario for hydrogen also exhibits variability. The difference between supply and demand data forms injection and production schedules. In [Salmachi et al., 2024] applies these ideas with a cycle of operation consists of 12 months of injection of cushion gas followed by a 12 month operation cycle on an hourly basis.

As another example, for the numerical modeling of the Suliszewo geological structure, different types of operation cycles have been used in order to determine: the maximum flow rate per unit time, the initial filling times or the amount of hydrogen recovered during the cycles. Cycles of 40 months have been proposed offering flowrates from 1 kg/s to 5 kg/s increasing with the passing of the months [Lubon and Tarkowski, 2020].

1.5 Document structure

In this chapter has put into context the current situation facing hydrogen as an energy source, and the possible options for its storage. It has also set out the objectives of this technical project for the study of operational cycles in underground storage in salt caverns. Therefore, the document has the following structure:

- In chapter 2: Materials and methods, will explain the numerical methods used to carry out the simulations, as well as the parameters defined for those simulations.

- In chapter 3: Results and discussion, will present and analyze the results obtained from the simulations with the different operating cycles used.
- In chapter 4: Conclusions and future research lines, presents the conclusions of the work and proposes future research lines to be developed.

Chapter 2

Materials and methods

2.1 Introduction

This chapter presents the means used for the execution of this project. Numerical simulation tools have been used to obtain the results from the solid mechanics problem, applying the finite element method (FEM). The formulation used to solve the problem will be presented later in this chapter, as well as the configuration and characteristics of the model considered.

The objectives of the structural analysis are the determination of the deformed geometry and the calculation of the stress-strain state of the cavern walls over time. The proposed approach considers small displacements, small displacement gradients, small deformations and creep. The elastic part of the stress-strain relation in the material is assumed to be linear. The calculations are performed using COMSOL Multiphysics® software [COMSOL AB, 2023], as described below.

In order to support the numerical results, a set of analytical calculations will be carried out using the same formulation. The material used in this calculation will be salt, which has the properties set out in Table 2.1.

E	30,000	MPa
ν	0.27	
ρ_{salt}	2,200	kg/m^3

Table 2.1: *Mechanic properties of the rock salt.*

Finally, the results will be compared and the correlation between both methods will be shown.

2.2 Mathematical model

The objectives of the structural analysis are the determination of the deformed geometry and the calculation of the stress-strain state of the cavern walls over time.

The mathematical model approach is based on solid mechanics. A kinematic model describes the motion of the particles of the solid as a function of the nodal displacements, a deformational model typifies the relative motions between nearby particles, splitting the

parts of the relative deformation that correspond to rotation and to strain (a stress-strain model stipulates the value of the internal stress). The mean objective consists on finding the nodal displacements that cause the rotations and strains that give rise to the stresses that satisfy the equilibrium equation by counteracting the applied external forces.

The deformation process is considered to be transient, so an incremental approach in combination with a time integration method will be required. That means, an incremental approach in combination with an iterative algorithm may be necessary to deal with the nonlinearity of the model.

Deformation is modeled using a Lagrangian description. The elastic part of the stress-strain relation in the material is assumed to be linear.

2.2.1 Kinematics

Let the deformable body (the cavern walls) be composed by the aggregation of material particles in such a large number that its texture is assumed to be continuous. Deformation is assumed to start at time $t = 0$ due to the application of external forces.

Let $\bar{r}_\circ$ be the initial coordinates of an arbitrary material particle before deformation starts. It is obvious that each particle can be identified by its initial (also called material) coordinates $\bar{r}_\circ$ while the values of the initial coordinates $\bar{r}_\circ$ of all the particles define the undeformed geometry.

Let $\bar{r}$ be the current coordinates of the material particle $\bar{r}_\circ$ under consideration at time $t > 0$. The values of the current coordinates $\bar{r}$ of all the particles define the current deformed geometry at time $t > 0$.

Consequently, there must be a mapping (to be determined) such that

$$\bar{r} = \bar{\chi}(\bar{r}_\circ, t). \tag{2.1}$$

For a given particle $\bar{r}_\circ$, expression (2.1) describes the particle motion over time. For a given time t, expression (2.1) describes the current positions of each and every material particle, i.e. the current deformation. Since the first objective of structural analysis is determination of deformation over time, obtaining function $\bar{\chi}(\bar{r}_\circ, t)$ in (2.1) could be considered as the main objective of the subsequent formulation.

Alternatively, Equation (2.1) can be rewritten as

$$\bar{r} = \bar{r}_\circ + \bar{u}(\bar{r}_\circ, t), \tag{2.2}$$

where $\bar{u}(\bar{r}_\circ, t)$ is the so-called displacement experienced by the material particle of initial coordinates $\bar{r}_\circ$ at time t, that is simply defined as

$$\bar{u}(\bar{r}_\circ, t) = \bar{\chi}(\bar{r}_\circ, t) - \bar{r}_\circ. \tag{2.3}$$

It is obvious that expressions (2.1) and (2.2) are equivalent, but the value of the displacement function $\bar{u}(\bar{r}_\circ, t)$ is more intuitive and easier to interpret than that of function $\bar{\chi}(\bar{r}_\circ, t)$. For this reason, obtaining function $\bar{u}(\bar{r}_\circ, t)$ will be considered as the main objective of the formulation from now on.

As expected in the treatment of this type of problems, reaching the analytical solution will only be possible in some simple academic cases. In the general case, therefore, it will be necessary to resort to a Computational Engineering approach.

In these kind of approaches, the exact solution $\bar{u}(\bar{r}_\circ, t)$ is discretized as

$$\bar{u}(\bar{r}_\circ, t) \approx \bar{u}^h(\bar{r}_\circ, t) = \sum_{\text{ip}=1,\text{np}} \bar{u}^{\text{ip}}(t)\ \phi_{\text{ip}}(\bar{r}_\circ)\ +\ \bar{u}^\Gamma(\bar{r}_\circ, t). \tag{2.4}$$

where the so-called trial functions $\phi_{\text{ip}}(\bar{r}_\circ)$ provide the spatial variation of the discretized solution $\bar{u}^h(\bar{r}_\circ, t)$, while the so-called nodal displacements $\bar{u}^{\text{ip}}(t)$ provide the time variation at each time step t. The inclusion of the last term $\bar{u}^\Gamma(\bar{r}_\circ, t)$ is an optional mechanism that could help to simplify the form of the boundary conditions in some cases.

The trial functions must be properly chosen so that the discretization type (2.4) can provide a sufficiently accurate approximation $\bar{u}^h(\bar{r}_\circ, t)$ to the exact solution $\bar{u}(\bar{r}_\circ, t)$. Common choices are piecewise polynomial functions. In turn, the nodal displacements $\bar{u}^{\text{ip}}(t)$ constitute the main unknowns of the discretized problem. Each index ip in (2.4) refers to a so-called node whose initial position is $\bar{r}_\circ^{\,\text{ip}}$. In general, the trial functions are defined in such a way that

$$\phi_{\text{ip}}(\bar{r}_\circ^{\,\text{jp}}) = \delta_{\text{ip}}^{\text{jp}}. \tag{2.5}$$

Thus, in the absence of the last term in (2.4) it is verified that

$$\bar{u}^h(\bar{r}_\circ^{\,\text{ip}}, t) = \bar{u}^{\text{ip}}(t), \tag{2.6}$$

which justifies the name (nodal displacement) given to $\bar{u}^{\text{ip}}(t)$.

When the nodes form a mesh, as in the Finite Element Method and its variants, the problem domain can be automatically fragmented into subdomains. This facilitates the definition of piecewise trial functions, which brings some notable computational advantages.

2.2.2 Deformation

With the aim of simplifying the formulation, both systems of coordinates $\bar{r}_\circ$ and $\bar{r}$ are assumed to be given with respect to the same usual orthogonal Cartesian basis $\{\vec{i}, \vec{j}, \vec{k}\}$ in the Euclidean space $\mathcal{R}^3$.

Let $\delta\bar{r}_\circ$ be the initial components of a so-called material vector that joins two nearby particles of initial coordinates $\bar{r}_\circ$ and $\bar{r}_\circ + \delta\bar{r}_\circ$ before deformation starts.

Let $\delta\bar{r}\big|_t$ be the current components of the material vector $\delta\bar{r}_\circ$ under consideration at time $t > 0$. From (2.1) it is easily seen that

$$\delta\bar{r}\big|_t = \bar{\chi}(\bar{r}_\circ + \delta\bar{r}_\circ, t) - \bar{\chi}(\bar{r}_\circ, t). \tag{2.7}$$

Since the particles under consideration are assumed to be close in space, both norms $\|\delta\bar{r}_\circ\|$ and $\|\delta\bar{r}\big|_t\|$ must be considered infinitesimal. From (2.7) it can be easily seen that

$$\delta\bar{r}\big|_t = \overbrace{\underset{\sim}{\mathcal{F}}(\bar{r}_\circ, t)\ \delta\bar{r}_\circ}^{\text{relative deformation}} + \mathcal{O}(\|\delta\bar{r}_\circ\|^2), \tag{2.8}$$

where

$$\underset{\sim}{\mathcal{F}}(\bar{r}_\circ, t) = \left[\frac{\partial}{\partial\bar{r}_\circ}\ \bar{\chi}(\bar{r}_\circ, t)\right] \tag{2.9}$$

is the so-called deformation gradient tensor. Taking into account (2.2), the deformation gradient tensor (2.9) can also be expressed as

$$\underset{\sim}{\mathcal{F}}(\bar{r}_\circ, t) = \underset{\sim}{\mathcal{I}} + \underset{\sim}{\mathcal{J}}(\bar{r}_\circ, t), \tag{2.10}$$

where

$$\underset{\sim}{\mathcal{J}}(\bar{r}_\circ, t) = \left[\frac{\partial}{\partial \bar{r}_\circ}\ \bar{u}(\bar{r}_\circ, t)\right] \tag{2.11}$$

is the so-called displacement gradient tensor. Expression (2.10) indicates that the deformation gradient tensor (2.9) and the displacement gradient tensor (2.11) contain essentially the same information. Therefore, they will be used in the formulation as appropriate at each step. Thus, substituting (2.10) in (2.8) gives

$$\delta\bar{r}\big|_t = \overbrace{\left(\underset{\sim}{\mathcal{I}} + \underset{\sim}{\mathcal{J}}(\bar{r}_\circ, t)\right)\ \delta\bar{r}_\circ}^{\text{relative deformation}} + \mathcal{O}(\|\delta\bar{r}_\circ\|^2), \tag{2.12}$$

which is the equivalent expression to (2.8) in terms of the displacement gradient tensor.

In this section the general case is assumed, in which the norm of the displacement gradient tensor $\|\underset{\sim}{\mathcal{J}}(\bar{r}_\circ, t)\|$ can be arbitrarily large in comparison to the norm of the unit tensor $\|\underset{\sim}{\mathcal{I}}\|$. Therefore, the deformation gradient tensor $\underset{\sim}{\mathcal{F}}(\bar{r}_\circ, t)$ may differ widely from the unit tensor $\underset{\sim}{\mathcal{I}}$ as a consequence of (2.10).

As a general rule, relative deformation may modify distances and angles between nearby material particles. As a consequence, the vicinity of each material particle may experience changes in volume, shape and orientation.

Expressions (2.8) and (2.12) describe the relative deformations that occur in the neighborhood of the material particle $\bar{r}_\circ$ by the effect of $\underset{\sim}{\mathcal{F}}(\bar{r}_\circ, t) = \left(\underset{\sim}{\mathcal{I}} + \underset{\sim}{\mathcal{J}}(\bar{r}_\circ, t)\right)$. Therefore, both the deformation gradient tensor and the displacement gradient tensor contain all the information concerning the change in volume, shape and orientation between instants $t = 0$ and $t > 0$ in the vicinity of each particle.

Indeed, from expression (2.8) it can be proven that a 3D differential region $d\Omega_\circ$ with initial differential volume $dV_\circ$ enclosing the material particle $\bar{r}_\circ$ experiences an expansion (or contraction) such that its current differential volume dV at time t is given by

$$dV\big|_t = \mathcal{F}(\bar{r}_\circ, t)\ dV_\circ \tag{2.13}$$

where

$$\mathcal{F}(\bar{r}_\circ, t) = \det\left(\underset{\sim}{\mathcal{F}}(\bar{r}_\circ, t)\right) = \det\left(\underset{\sim}{\mathcal{I}} + \underset{\sim}{\mathcal{J}}(\bar{r}_\circ, t)\right) \tag{2.14}$$

is the volume expansion factor.

Since the ratio between the current diferential volume dV and the initial differential volume $dV_\circ$ is necessarily positive, from expression (2.13) it follows immediately that the determinant (2.14) is always positive and consequently nonzero. Therefore, the deformation gradient tensor (2.9) is always non-singular and consequently invertible. Apart from fulfilling this condition, the deformation gradient tensor (2.9) can be a matrix of any type.

Expressions (2.13) and (2.14) imply that the determinant of the deformation gradient tensor must necessarily be greater than zero in any situation, since negative or zero values would be physically meaningless. This proves that the deformation gradient tensor is always an invertible matrix with positive determinant.

From expression (2.8) it can also be proven that a 2D differential surface $d\Gamma_\circ$ with initial differential area $dA_\circ$ and initial unit normal vector $\bar{n}_\circ$ enclosing the material particle $\bar{r}_\circ$ experiences an expansion (or contraction) such that the current differential area dA and the current unit normal vector $\bar{n}$ at time t are related to the initial values as

$$(dA\ \bar{n})|_t = \mathcal{F}(\bar{r}_\circ, t)\ \underset{\sim}{\mathcal{F}}^{-T}(\bar{r}_\circ, t)\ (dA_\circ\ \bar{n}_\circ). \tag{2.15}$$

The type of relative deformation that occurs in the neighborhood of the material particle $\bar{r}_\circ$ depends on the characteristics of the deformation gradient tensor $\underset{\sim}{\mathcal{F}}(\bar{r}_\circ, t)$.

When tensor $\underset{\sim}{\mathcal{F}}(\bar{r}_\circ, t)$ verifies

$$\underset{\sim}{\mathcal{F}}^{T}(\bar{r}_\circ, t) = \underset{\sim}{\mathcal{F}}^{-1}(\bar{r}_\circ, t) \quad \text{with} \quad \det\big(\underset{\sim}{\mathcal{F}}(\bar{r}_\circ, t)\big) = 1, \tag{2.16}$$

the relative deformation is said to be a rotation. We can verify that both, distances and angles between close material particles are not modified in this case. Therefore, this kind of deformation may change the orientation in space of any differential region enclosing the material particle $\bar{r}_\circ$, but shape and volume are left unaltered.

When tensor $\underset{\sim}{\mathcal{F}}(\bar{r}_\circ, t)$ verifies

$$\underset{\sim}{\mathcal{F}}^{T}(\bar{r}_\circ, t) = \underset{\sim}{\mathcal{F}}(\bar{r}_\circ, t) \quad \text{with} \quad \underset{\sim}{\mathcal{F}}(\bar{r}_\circ, t) \quad \text{positive definite}, \tag{2.17}$$

the relative deformation is said to be a stretch. It is easy to see that both distances and angles between close material particles may be modified in this case. Therefore, this kind of deformation may change the volume and shape of any differential region enclosing the material particle $\bar{r}_\circ$, but orientation in space is left unaltered. A first important particular type of stretch occurs when tensor $\underset{\sim}{\mathcal{F}}(\bar{r}_\circ, t)$ verifies (2.17) and

$$\det\big(\underset{\sim}{\mathcal{F}}(\bar{r}_\circ, t)\big) = 1. \tag{2.18}$$

This kind of relative deformation is said to be an isochoric stretch or a distortion. As in (2.17) distances and angles between close material particles may be modified in this case. Therefore, this kind of deformation may change the shape of any differential region enclosing the material particle $\bar{r}_\circ$, but volume is left unchanged (since the volume expansion factor is one) and orientation in space is left unaltered. As in (2.17) it can be shown that a differential sphere centered on each material particle is transformed into a differential ellipsoid with the same volume.

A second important particular type of stretch occurs when tensor $\underset{\sim}{\mathcal{F}}(\bar{r}_\circ, t)$ takes the form

$$\underset{\sim}{\mathcal{F}}(\bar{r}_\circ, t) = \big(\underset{\sim}{\mathcal{I}} + \eta(\bar{r}_\circ, t)\ \underset{\sim}{\mathcal{I}}\big), \tag{2.19}$$

This kind of relative deformation is said to be an isotropic stretch or a pure dilation. It can be easily seen that distances between close material particles are equally expanded (or

contracted) by the dilation factor $\eta(\bar{r}_\circ, t)$ independently of the direction in space, while angles remain unchanged in this case. Therefore, this kind of deformation may change the volume of any differential region enclosing the material particle $\bar{r}_\circ$, but shape and orientation in space are left unaltered.

From (2.19) it is immediate to see that the volume expansion factor is

$$\mathcal{F}(\bar{r}_\circ, t) = \big(1 + \eta(\bar{r}_\circ, t)\big)^n, \tag{2.20}$$

where n is the number of dimensions of the space. This kind of deformation transforms a differential sphere centered on each material point into another differential sphere, being $\eta(\bar{r}_\circ, t)$ the dilation factor of the radius.

In Computational Engineering methods, as explained above, the displacement is typically discretized as shown in (2.4). Introducing this approximation in (2.11) gives

$$\underset{\sim}{\mathcal{J}}(\bar{r}_\circ, t) \approx \underset{\sim}{\mathcal{J}}^h(\bar{r}_\circ, t) = \left[\frac{\partial}{\partial \bar{r}_\circ}\, \bar{u}^h(\bar{r}_\circ, t)\right] = \sum_{\text{ip}=1,\text{np}} \bar{u}^{\text{ip}}(t)\, \left[\frac{\partial}{\partial \bar{r}_\circ}\, \phi_{\text{ip}}(\bar{r}_\circ)\right] + \left[\frac{\partial}{\partial \bar{r}_\circ}\, \bar{u}^\Gamma(\bar{r}_\circ, t)\right], \tag{2.21}$$

which shows how the displacement gradient tensor is computed in numerical formulations.

2.2.3 Finite deformation theory

It can be proven that any invertible matrix $\underset{\sim}{\mathcal{F}}$ with positive determinant can be expressed in a unique multiplicative form by means of the so-called polar decomposition as

$$\underset{\sim}{\mathcal{F}} = \underset{\sim}{\mathcal{R}}(\underset{\sim}{\mathcal{I}} + \underset{\sim}{\mathcal{E}}), \qquad \text{with} \quad \begin{cases} \underset{\sim}{\mathcal{R}}^T = \underset{\sim}{\mathcal{R}}^{-1}, \quad \det(\underset{\sim}{\mathcal{R}}) = 1, \\ (\underset{\sim}{\mathcal{I}} + \underset{\sim}{\mathcal{E}})^T = (\underset{\sim}{\mathcal{I}} + \underset{\sim}{\mathcal{E}}), \quad (\underset{\sim}{\mathcal{I}} + \underset{\sim}{\mathcal{E}}) \text{ positive definite.} \end{cases} \tag{2.22}$$

Applying this concept, the deformation gradient tensor can be decomposed as

$$\underset{\sim}{\mathcal{F}}(\bar{r}_\circ, t) = \underset{\sim}{\mathcal{R}}(\bar{r}_\circ, t)\, \big(\underset{\sim}{\mathcal{I}} + \underset{\sim}{\mathcal{E}}(\bar{r}_\circ, t)\big), \tag{2.23}$$

where the relative deformation produced by tensor $\underset{\sim}{\mathcal{R}}(\bar{r}_\circ, t)$ is of rotation type, thus satisfying

$$\underset{\sim}{\mathcal{R}}^T(\bar{r}_\circ, t)\, \underset{\sim}{\mathcal{R}}(\bar{r}_\circ, t) = \underset{\sim}{\mathcal{I}} \quad \text{with} \quad \det\big(\underset{\sim}{\mathcal{R}}(\bar{r}_\circ, t)\big) = 1, \tag{2.24}$$

and the relative deformation produced by tensor $\big(\underset{\sim}{\mathcal{I}} + \underset{\sim}{\mathcal{E}}(\bar{r}_\circ, t)\big)$ is of stretch type, thus satisfying

$$\big(\underset{\sim}{\mathcal{I}} + \underset{\sim}{\mathcal{E}}(\bar{r}_\circ, t)\big)^T = \big(\underset{\sim}{\mathcal{I}} + \underset{\sim}{\mathcal{E}}(\bar{r}_\circ, t)\big) \quad \text{with} \quad \big(\underset{\sim}{\mathcal{I}} + \underset{\sim}{\mathcal{E}}(\bar{r}_\circ, t)\big) \text{ positive definite.} \tag{2.25}$$

As a consequence, we can see that

$$\det\big(\underset{\sim}{\mathcal{I}} + \underset{\sim}{\mathcal{E}}(\bar{r}_\circ, t)\big) = \mathcal{F}(\bar{r}_\circ, t). \tag{2.26}$$

In these terms, expressions (2.8) and (2.12) can be rewritten as

$$\delta\bar{r}\big|_t = \overbrace{\underset{\sim}{\mathcal{R}}(\bar{r}_\circ, t)}^{\text{rotation}} \quad \overbrace{\big(\underset{\sim}{\mathcal{I}} + \underset{\sim}{\mathcal{E}}(\bar{r}_\circ, t)\big)}^{\text{stretch}}\, \delta\bar{r}_\circ + \mathcal{O}(\|\bar{r}_\circ\|^2). \tag{2.27}$$

This expression shows that the neighborhood of the material particle $\bar{r}_\circ$ is first stretched by the effect of $\big(\underset{\sim}{\mathcal{I}} + \underset{\sim}{\mathcal{E}}(\bar{r}_\circ, t)\big)$ and then rotated as a whole by the effect of $\underset{\sim}{\mathcal{R}}(\bar{r}_\circ, t)$.

Indeed, the stretching effect caused by $\big(\underset{\sim}{\mathcal{I}} + \underset{\sim}{\mathcal{E}}(\bar{r}_\circ, t)\big)$ may modify distances and angles between material particles, but the rotation caused by $\underset{\sim}{\mathcal{R}}(\bar{r}_\circ, t)$ leaves them unaltered.

For this reason, the so-called Biot strain tensor $\underset{\sim}{\mathcal{E}}(\bar{r}_\circ, t)$ can be considered as the more natural and intuitive way of measuring strain in the vicinity of the position of any given material particle $\bar{r}_\circ$ at time t.

From expression (2.27), tensor $\big(\underset{\sim}{\mathcal{I}} + \underset{\sim}{\mathcal{E}}(\bar{r}_\circ, t)\big)$ accounts for the changes in volume and shape that give rise to internal forces, while tensor $\underset{\sim}{\mathcal{R}}(\bar{r}_\circ, t)$ accounts for the subsequent change of the orientation of stresses in space. However, it might be useful to make further progress in an attempt to separate the parts of tensor $\big(\underset{\sim}{\mathcal{I}} + \underset{\sim}{\mathcal{E}}(\bar{r}_\circ, t)\big)$ that explain the change in volume and the change in shape. To achieve this, the last term of the right hand side in (2.23) is decomposed as

$$\big(\underset{\sim}{\mathcal{I}} + \underset{\sim}{\mathcal{E}}(\bar{r}_\circ, t)\big) = \big(\underset{\sim}{\mathcal{I}} + \underset{\sim}{\mathcal{E}}_{\!d}(\bar{r}_\circ, t)\big)\ \big(\underset{\sim}{\mathcal{I}} + \eta(\bar{r}_\circ, t)\ \underset{\sim}{\mathcal{I}}\big) \tag{2.28}$$

with

$$\underset{\sim}{\mathcal{E}}_{\!d}(\bar{r}_\circ, t) = \frac{1}{1 + \eta(\bar{r}_\circ, t)}\ \big(\underset{\sim}{\mathcal{E}}(\bar{r}_\circ, t) - \eta(\bar{r}_\circ, t)\ \underset{\sim}{\mathcal{I}}\big) \tag{2.29}$$

and

$$\eta(\bar{r}_\circ, t) = \big(\mathcal{F}(\bar{r}_\circ, t)\big)^{1/n} - 1, \tag{2.30}$$

where n is the number of dimensions of the space.

The relative deformation produced by tensor $\big(\underset{\sim}{\mathcal{I}} + \eta(\bar{r}_\circ, t)\ \underset{\sim}{\mathcal{I}}\big)$ is of pure dilation (or isotropic stretch) type with

$$\det\big(\underset{\sim}{\mathcal{I}} + \eta(\bar{r}_\circ, t)\ \underset{\sim}{\mathcal{I}}\big) = \mathcal{F}(\bar{r}_\circ, t). \tag{2.31}$$

Taking this into account and substituting (2.28) in (2.26) leads to

$$\det\big(\underset{\sim}{\mathcal{I}} + \underset{\sim}{\mathcal{E}}_{\!d}(\bar{r}_\circ, t)\big) = 1. \tag{2.32}$$

Therefore, it is immediate to see that the relative deformation produced by tensor $\big(\underset{\sim}{\mathcal{I}} + \underset{\sim}{\mathcal{E}}_{\!d}(\bar{r}_\circ, t)\big)$ is of distortion (or isochoric stretch) type, thus satisfying

$$\big(\underset{\sim}{\mathcal{I}} + \underset{\sim}{\mathcal{E}}_{\!d}(\bar{r}_\circ, t)\big)^{\,T} = \big(\underset{\sim}{\mathcal{I}} + \underset{\sim}{\mathcal{E}}_{\!d}(\bar{r}_\circ, t)\big) \quad \text{with} \quad \big(\underset{\sim}{\mathcal{I}} + \underset{\sim}{\mathcal{E}}_{\!d}(\bar{r}_\circ, t)\big) \quad \text{positive definite.} \tag{2.33}$$

Substituting (2.28) in (2.23) leads to

$$\underset{\sim}{\mathcal{F}}(\bar{r}_\circ, t) = \underset{\sim}{\mathcal{R}}(\bar{r}_\circ, t)\ \big(\underset{\sim}{\mathcal{I}} + \underset{\sim}{\mathcal{E}}_{\!d}(\bar{r}_\circ, t)\big)\ \big(\underset{\sim}{\mathcal{I}} + \eta(\bar{r}_\circ, t)\ \underset{\sim}{\mathcal{I}}\big). \tag{2.34}$$

In these terms, expressions (2.8) and (2.27) can be rewritten as

$$\delta\bar{r}\big|_t = \overbrace{\underset{\sim}{\mathcal{R}}(\bar{r}_\circ, t)}^{\text{rotation}}\ \overbrace{\big(\underset{\sim}{\mathcal{I}} + \underset{\sim}{\mathcal{E}}_{\!d}(\bar{r}_\circ, t)\big)}^{\text{isochoric stretch – distorsion}}\ \overbrace{\big(\underset{\sim}{\mathcal{I}} + \eta(\bar{r}_\circ, t)\ \underset{\sim}{\mathcal{I}}\big)}^{\text{pure dilation}}\ \delta\bar{r}_\circ\ + \mathcal{O}(\|\delta\bar{r}_\circ\|^2), \tag{2.35}$$

This expression shows that the vicinity of the material particle $\bar{r}_\circ$ is first dilated by the effect of $\left(\underset{\sim}{\mathcal{I}} + \eta(\bar{r}_\circ, t)\ \underset{\sim}{\mathcal{I}}\right)$, then distorted by the effect of $\left(\underset{\sim}{\mathcal{I}} + \underset{\sim\sim}{\mathcal{E}}_d(\bar{r}_\circ, t)\right)$ and finally rotated as a whole by the effect of $\underset{\sim\sim}{\mathcal{R}}(\bar{r}_\circ, t)$. For this reason tensor $\underset{\sim\sim}{\mathcal{E}}_d(\bar{r}_\circ, t)$ receives the names of distortion tensor or deviatoric strain tensor.

Tensors $\left(\underset{\sim}{\mathcal{I}} + \eta(\bar{r}_\circ, t)\ \underset{\sim}{\mathcal{I}}\right)$ and $\left(\underset{\sim}{\mathcal{I}} + \underset{\sim\sim}{\mathcal{E}}_d(\bar{r}_\circ, t)\right)$ account respectively for the change in volume and the change in shape that give rise to internal forces, while tensor $\underset{\sim\sim}{\mathcal{R}}(\bar{r}_\circ, t)$ accounts exclusively for the change in orientation of stresses in space.

Expression (2.34) separates the information regarding the rotation, distortion and dilation produced by the relative deformation, what is necessary to formulate suitable constitutive equations for Cauchy-elastic materials.

To this end, it is essential to be able to perform polar decomposition (2.22) efficiently. In the context of a Finite Element Method implementation, decomposition (2.34) must be performed at each integration point and repeated for each time step, what multiplies the chances of failure and makes the overall computational cost highly unpredictable.

Other strain tensors get to extract the information regarding the distortion and dilation due to the deformation, but at the cost of losing the information regarding the rotation. In particular, the Green strain tensor $\underset{\sim}{E}(\bar{r}_\circ, t)$ is defined as

$$\underset{\sim}{E}(\bar{r}_\circ, t) = \frac{1}{2}\left(\underset{\sim}{\mathcal{F}}^T(\bar{r}_\circ, t)\,\underset{\sim}{\mathcal{F}}(\bar{r}_\circ, t) - \underset{\sim}{\mathcal{I}}\right). \tag{2.36}$$

Substituting (2.10) in (2.36) gives the alternative expression

$$\underset{\sim}{E}(\bar{r}_\circ, t) = \frac{1}{2}\left(\underset{\sim\sim}{\mathcal{J}}(\bar{r}_\circ, t) + \underset{\sim\sim}{\mathcal{J}}^T(\bar{r}_\circ, t) + \underset{\sim\sim}{\mathcal{J}}^T(\bar{r}_\circ, t)\ \underset{\sim\sim}{\mathcal{J}}(\bar{r}_\circ, t)\right). \tag{2.37}$$

From (2.8) it can be seen that

$$\delta\bar{r}\big|_t{}^T\,\delta\bar{r}\big|_t - \delta\bar{r}_\circ^T\,\delta\bar{r}_\circ = 2\ \delta\bar{r}_\circ^T\ \underset{\sim}{E}(\bar{r}_\circ, t)\ \delta\bar{r}_\circ\ +\ \mathcal{O}(\|\delta\bar{r}_\circ\|^3). \tag{2.38}$$

Substituting (2.23) in (2.36) it can be seen that

$$\underset{\sim}{E}(\bar{r}_\circ, t) = \frac{1}{2}\left(\left(\underset{\sim}{\mathcal{I}} + \underset{\sim}{\mathcal{E}}(\bar{r}_\circ, t)\right)^2 - \underset{\sim}{\mathcal{I}}\right). \tag{2.39}$$

Alternatively, substituting (2.34) in (2.36) gives the equivalent expression

$$\underset{\sim}{E}(\bar{r}_\circ, t) = \frac{1}{2}\left(\left(1 + \eta(\bar{r}_\circ, t)\right)^2\ \left(\underset{\sim}{\mathcal{I}} + \underset{\sim\sim}{\mathcal{E}}_d(\bar{r}_\circ, t)\right)^2 - \underset{\sim}{\mathcal{I}}\right). \tag{2.40}$$

Expression (2.39) shows that the Green strain tensor (2.36) retains the information regarding the stretching due to the deformation but the information regarding the rotation is lost.

Since the determinant (2.14) can be easily computed, expression (2.40) provides a way to separate the information regarding the distortion and dilation due to the deformation.

Finally, from (2.39) it can be easily seen that

$$\underset{\sim}{E}(\bar{r}_\circ, t) = \underset{\sim}{\mathcal{E}}(\bar{r}_\circ, t)\ \left(\underset{\sim}{\mathcal{I}} + \frac{1}{2}\,\underset{\sim}{\mathcal{E}}(\bar{r}_\circ, t)\right). \tag{2.41}$$

This expression indicates that the difference between the Green strain tensor $\underset{\sim}{E}(\bar{r}_\circ, t)$ and the Biot Strain tensor $\underset{\sim}{\mathcal{E}}(\bar{r}_\circ, t)$ is negligible when $\|\underset{\sim}{\mathcal{E}}(\bar{r}_\circ, t)\| << \|\underset{\sim}{\mathcal{I}}\|$. When this conditions holds, the material is said to be in a small strain regime. In particular, this happens when the infinitesimal deformation theory is applied.

Expressions (2.39) and (2.41) are equivalent, since both give the Green strain tensor $\underset{\sim}{E}(\bar{r}_\circ, t)$ in terms of the Biot strain tensor $\underset{\sim}{\mathcal{E}}(\bar{r}_\circ, t)$ and either of them can be easily reversed, which allows to write the Biot strain tensor $\underset{\sim}{\mathcal{E}}(\bar{r}_\circ, t)$ in terms of the Green strain tensor $\underset{\sim}{E}(\bar{r}_\circ, t)$ as

$$\underset{\sim}{\mathcal{E}}(\bar{r}_\circ, t) = \big((\underset{\sim}{\mathcal{I}} + 2\ \underset{\sim}{E}(\bar{r}_\circ, t))^{1/2} - \underset{\sim}{\mathcal{I}}\big). \tag{2.42}$$

The evaluation of expression (2.42) implies the extraction of the square root of the third order matrix $(\underset{\sim}{\mathcal{I}} + 2\ \underset{\sim}{E}(\bar{r}_\circ, t))$. This matrix is necessarily positive definite by construction. In fact, expression (2.42) allows to perform the polar decomposition (2.23), since once the Biot strain tensor $\underset{\sim}{\mathcal{E}}(\bar{r}_\circ, t)$ has been obtained, the rotation tensor $\underset{\sim}{\mathcal{R}}(\bar{r}_\circ, t)$ can be easily cleared at expression (2.23), which gives

$$\underset{\sim}{\mathcal{R}}(\bar{r}_\circ, t) = \underset{\sim}{\mathcal{F}}(\bar{r}_\circ, t)\ \big(\underset{\sim}{\mathcal{I}} + \underset{\sim}{\mathcal{E}}(\bar{r}_\circ, t)\big)^{-1}. \tag{2.43}$$

Finally, it is important to note that finite relative deformations are multiplicative, since the combined effect of the finite relative deformations produced first by tensor $\underset{\sim}{\mathcal{F}_1}(\bar{r}_\circ, t) = \underset{\sim}{\mathcal{I}} + \underset{\sim}{\mathcal{J}_1}(\bar{r}_\circ, t)$ and then by tensor $\underset{\sim}{\mathcal{F}_2}(\bar{r}_\circ, t) = \underset{\sim}{\mathcal{I}} + \underset{\sim}{\mathcal{J}_2}(\bar{r}_\circ, t)$ is equivalent to the finite relative deformation produced by the product

$$\underset{\sim}{\mathcal{F}}(\bar{r}_\circ, t) = \underset{\sim}{\mathcal{F}_2}(\bar{r}_\circ, t)\ \underset{\sim}{\mathcal{F}_1}(\bar{r}_\circ, t) = \big(\underset{\sim}{\mathcal{I}} + \underset{\sim}{\mathcal{J}_2}(\bar{r}_\circ, t)\big)\ \big(\underset{\sim}{\mathcal{I}} + \underset{\sim}{\mathcal{J}_1}(\bar{r}_\circ, t)\big). \tag{2.44}$$

In view of (2.44), finite relative deformations do not commute. Moreover, the equivalent deformation gradient tensor can be expressed as

$$\underset{\sim}{\mathcal{F}}(\bar{r}_\circ, t) = \big(\underset{\sim}{\mathcal{I}} + \underset{\sim}{\mathcal{J}}(\bar{r}_\circ, t)\big) \quad \text{with} \quad \underset{\sim}{\mathcal{J}}(\bar{r}_\circ, t) = \underset{\sim}{\mathcal{J}_1}(\bar{r}_\circ, t) + \underset{\sim}{\mathcal{J}_2}(\bar{r}_\circ, t) + \underset{\sim}{\mathcal{J}_2}(\bar{r}_\circ, t)\ \underset{\sim}{\mathcal{J}_1}(\bar{r}_\circ, t), \tag{2.45}$$

which gives the general expression for the equivalent displacement gradient tensor $\underset{\sim}{\mathcal{J}}(\bar{r}_\circ, t)$.

2.2.4 Infinitesimal deformation theory

In this section, it is assumed that the norm $\|\underset{\sim}{\mathcal{J}}(\bar{r}_\circ, t)\|$ of the gradient displacement tensor is sufficiently small compared to the norm $\|\underset{\sim}{\mathcal{I}}\|$ of the unit tensor so that some suitable approximations can be considered acceptable. Therefore, the deformation gradient tensor $\underset{\sim}{\mathcal{F}}(\bar{r}_\circ, t)$ should not differ much from the unit tensor $\underset{\sim}{\mathcal{I}}$.

The basic assumption is

$$\|\underset{\sim}{\mathcal{J}}(\bar{r}_\circ, t)\| << \|\underset{\sim}{\mathcal{I}}\|, \tag{2.46}$$

For this condition to be satisfied, the absolute value of the coefficients of the displacement gradient tensor $\underset{\sim}{\mathcal{J}}(\bar{r}_\circ, t)$ must be sufficiently small in comparison to the unit. In particular, this implies

$$\big|\mathrm{tr}\big(\underset{\sim}{\mathcal{J}}(\bar{r}_\circ, t)\big)\big| << 1. \tag{2.47}$$

In these conditions, a number of suitable approximations can be applied, namely:

$$\det\big(\underset{\sim}{\mathcal{I}} + \underset{\sim}{\mathcal{J}}(\bar{r}_\circ, t)\big) \;\approx\; \Big(1 + \operatorname{tr}\big(\underset{\sim}{\mathcal{J}}(\bar{r}_\circ, t)\big)\Big), \tag{2.48}$$

$$\Big(1 + \operatorname{tr}\big(\underset{\sim}{\mathcal{J}}(\bar{r}_\circ, t)\big)\Big)^{\pm 1/n} \;\approx\; \Big(1 \pm \frac{1}{n}\;\operatorname{tr}\big(\underset{\sim}{\mathcal{J}}(\bar{r}_\circ, t)\big)\Big), \tag{2.49}$$

$$\big(\underset{\sim}{\mathcal{I}} + \underset{\sim}{\mathcal{J}}(\bar{r}_\circ, t)\big)^{-1} \;\approx\; \big(\underset{\sim}{\mathcal{I}} - \underset{\sim}{\mathcal{J}}(\bar{r}_\circ, t)\big), \tag{2.50}$$

and

$$\underset{\sim}{\mathcal{F}}(\bar{r}_\circ, t) = \underset{\sim}{\mathcal{R}}(\bar{r}_\circ, t)\;\big(\underset{\sim}{\mathcal{I}} + \underset{\sim}{\mathcal{E}}(\bar{r}_\circ, t)\big) \;\approx\; \underset{\sim}{\widehat{\mathcal{R}}}(\bar{r}_\circ, t)\;\big(\underset{\sim}{\mathcal{I}} + \underset{\sim}{\widehat{\mathcal{E}}}(\bar{r}_\circ, t)\big), \tag{2.51}$$

where

$$\underset{\sim}{\mathcal{R}}(\bar{r}_\circ, t) \approx \underset{\sim}{\widehat{\mathcal{R}}}(\bar{r}_\circ, t) = \underset{\sim}{\mathcal{I}} + \frac{1}{2}\;\big(\underset{\sim}{\mathcal{J}}(\bar{r}_\circ, t) - \underset{\sim}{\mathcal{J}}^T(\bar{r}_\circ, t)\big), \tag{2.52}$$

and

$$\underset{\sim}{\mathcal{E}}(\bar{r}_\circ, t) \approx \underset{\sim}{\widehat{\mathcal{E}}}(\bar{r}_\circ, t) = \frac{1}{2}\;\big(\underset{\sim}{\mathcal{J}}(\bar{r}_\circ, t) + \underset{\sim}{\mathcal{J}}^T(\bar{r}_\circ, t)\big). \tag{2.53}$$

Basically, (2.48) comes from the fact that the absolute value of the coefficients of the displacement gradient tensor $\underset{\sim}{\mathcal{J}}(\bar{r}_\circ, t)$ are very small in comparison to the unit, while (2.49) is a direct consequence of the Taylor expansion of $f(x) = (1+x)^a$ for values of variable x such that $|x| << 1$.

On the other hand, (2.50) can be proven by neglecting the higher order error terms in

$$\big(\underset{\sim}{\mathcal{I}} + \underset{\sim}{\mathcal{J}}(\bar{r}_\circ, t)\big)\;\big(\underset{\sim}{\mathcal{I}} - \underset{\sim}{\mathcal{J}}(\bar{r}_\circ, t)\big) = \underset{\sim}{\mathcal{I}} - \big(\underset{\sim}{\mathcal{J}}(\bar{r}_\circ, t)\big)^2 = \underset{\sim}{\mathcal{I}} \;+\; \mathcal{O}(\|\underset{\sim}{\mathcal{J}}(\bar{r}_\circ, t)\|^2). \tag{2.54}$$

Similarly, (2.51), (2.52) and (2.53) can be proven by substituting (2.52) and (2.53) in (2.23), (2.24) and (2.25) and checking that the established conditions are fulfilled when the higher order error terms are neglected.

In these terms, expressions (2.23) and (2.27) can be approximated respectively as

$$\underset{\sim}{\mathcal{F}}(\bar{r}_\circ, t) \;\approx\; \underset{\sim}{\widehat{\mathcal{R}}}(\bar{r}_\circ, t)\;\big(\underset{\sim}{\mathcal{I}} + \underset{\sim}{\widehat{\mathcal{E}}}(\bar{r}_\circ, t)\big) \tag{2.55}$$

and

$$\delta\bar{r}|_t \;\approx\; \overbrace{\underset{\sim}{\widehat{\mathcal{R}}}(\bar{r}_\circ, t)}^{\text{approx. rotation}}\;\overbrace{\big(\underset{\sim}{\mathcal{I}} + \underset{\sim}{\widehat{\mathcal{E}}}(\bar{r}_\circ, t)\big)}^{\text{approx. stretch}}\;\delta\bar{r}_\circ \;+\; \mathcal{O}(\|\delta\bar{r}_\circ\|^2). \tag{2.56}$$

Some further consequences of the approximations (2.48)–(2.53) are

$$\underset{\sim}{\mathcal{E}}_d(\bar{r}_\circ, t) \;\approx\; \underset{\sim}{\widehat{\mathcal{E}}}_d(\bar{r}_\circ, t) = \big(\underset{\sim}{\widehat{\mathcal{E}}}(\bar{r}_\circ, t) - \widehat{\eta}(\bar{r}_\circ, t)\;\underset{\sim}{\mathcal{I}}\big) \tag{2.57}$$

and

$$\eta(\bar{r}_\circ, t) \;\approx\; \widehat{\eta}(\bar{r}_\circ, t) = \frac{1}{n}\operatorname{tr}\big(\underset{\sim}{\mathcal{J}}(\bar{r}_\circ, t)\big), \tag{2.58}$$

where n is the number of dimensions of the space.

Also,

$$\operatorname{tr}\big(\underset{\sim}{\widehat{\mathcal{E}}}(\bar{r}_\circ, t)\big) = \operatorname{tr}\big(\underset{\sim}{\mathcal{J}}(\bar{r}_\circ, t)\big) \tag{2.59}$$

and

$$\mathrm{tr}\big(\widehat{\underset{\sim}{\mathcal{E}}}_d(\bar{r}_\circ,t)\big)=0. \tag{2.60}$$

Then, expressions (2.34) and (2.35) can be approximated respectively as

$$\underset{\sim}{\mathcal{F}}(\bar{r}_\circ,t)\;\approx\;\big(\underset{\sim}{\mathcal{I}}+\widehat{\underset{\sim}{\mathcal{R}}}(\bar{r}_\circ,t)\big)\;\big(\underset{\sim}{\mathcal{I}}+\widehat{\underset{\sim}{\mathcal{E}}}_d(\bar{r}_\circ,t)\big)\;\big(\underset{\sim}{\mathcal{I}}+\widehat{\eta}(\bar{r}_\circ,t)\;\underset{\sim}{\mathcal{I}}\big) \tag{2.61}$$

and

$$\delta\bar{r}\big|_t=\overbrace{\overbrace{\widehat{\underset{\sim}{\mathcal{R}}}(\bar{r}_\circ,t)}^{\text{approx. rotation}}\;\overbrace{\big(\underset{\sim}{\mathcal{I}}+\widehat{\underset{\sim}{\mathcal{E}}}_d(\bar{r}_\circ,t)\big)}^{\text{approx. isochoric stretch – distorsion}}\;\overbrace{\big(\underset{\sim}{\mathcal{I}}+\widehat{\eta}(\bar{r}_\circ,t)\;\underset{\sim}{\mathcal{I}}\big)\;\delta\bar{r}_\circ}^{\text{approx. pure dilation}}}^{}+\mathcal{O}(\|\delta\bar{r}_\circ\|^2), \tag{2.62}$$

Taking into account (2.46) and (2.53) leads to

$$\|\underset{\sim}{\mathcal{E}}(\bar{r}_\circ,t)\|\approx\|\widehat{\underset{\sim}{\mathcal{E}}}\|<<\|\underset{\sim}{\mathcal{I}}\|, \tag{2.63}$$

which implies that the material is necessarily in a small strain regime when the infinitesimal deformation theory is applied, as advanced at the end of the previous section. In accordance with the above, expression (2.37) reduces to

$$\underset{\sim}{E}(\bar{r}_\circ,t)\approx\tfrac{1}{2}\,\big(\underset{\sim}{\mathcal{J}}(\bar{r}_\circ,t)+\underset{\sim}{\mathcal{J}}^T(\bar{r}_\circ,t)\big)=\widehat{\underset{\sim}{\mathcal{E}}}(\bar{r}_\circ,t) \tag{2.64}$$

which proves that the Green strain tensor $\underset{\sim}{E}(\bar{r}_\circ,t)$, the Biot strain tensor $\underset{\sim}{\mathcal{E}}(\bar{r}_\circ,t)$ and the infinitesimal Biot strain tensor $\widehat{\underset{\sim}{\mathcal{E}}}(\bar{r}_\circ,t)$ are indistinguishable in the framework of the infinitesimal deformation theory.

Note that all the approximations given above allow full linearization of the deformation analysis of the problem. Moreover, approximations (2.52) and (2.53) provide a direct and explicit procedure for performing the approximated polar decomposition (2.51) in consistency with the order of approximation of the theory. These facts greatly facilitates both, the analytical manipulation and the numerical implementation of the deformation analysis in this case.

Finally, it is important to note that infinitesimal relative deformations are (approximately) additive, since in this case (2.45) reduces to

$$\underset{\sim}{\mathcal{F}}(\bar{r}_\circ,t)\approx\big(\underset{\sim}{\mathcal{I}}+\widehat{\underset{\sim}{\mathcal{J}}}(\bar{r}_\circ,t)\big)\;\;\text{with}\;\;\widehat{\underset{\sim}{\mathcal{J}}}(\bar{r}_\circ,t)=\underset{\sim}{\mathcal{J}}_1(\bar{r}_\circ,t)+\underset{\sim}{\mathcal{J}}_2(\bar{r}_\circ,t). \tag{2.65}$$

In view of (2.65), infinitesimal relative deformations commute. From (2.65) it also follows immediately that when several infinitesimal relative deformations occur sequentially, the infinitesimal Biot strain tensors add up.

2.2.5 Incremental deformation theory

As stated above, expressions (2.8) and (2.12) describe the relative deformations that occur in the neighborhood of the material particle $\bar{r}_\circ$ over time, thus providing the current configuration at time t in terms of the initial configuration at time $t = 0$.

In this section, we seek to explain how the process progresses over time, providing the current configuration at time $(t + dt)$ in terms of the current configuration at time t.

Differentiation of expression (2.8) with respect to t gives

$$\left(\frac{\partial}{\partial t}\ \delta\bar{r}|_t\right) = \left[\frac{\partial}{\partial t}\ \underset{\sim}{\mathcal{F}}(\bar{r}_\circ, t)\right]\ \delta\bar{r}_\circ\ +\ \mathcal{O}(\|\delta\bar{r}_\circ\|^2). \tag{2.66}$$

On the other hand, from (2.8) it can be easily shown that

$$\delta\bar{r}_\circ = \underset{\sim}{\mathcal{F}}^{-1}(\bar{r}_\circ, t)\ \delta\bar{r}|_t\ +\ \mathcal{O}(\|\delta\bar{r}_\circ\|^2). \tag{2.67}$$

Then, substitution of (2.67) in (2.66) gives

$$\left(\frac{\partial}{\partial t}\ \delta\bar{r}|_t\right) = \underset{\sim}{\ell}\,(\bar{r}_\circ, t)\ \delta\bar{r}|_t\ +\ \mathcal{O}(\|\delta\bar{r}_\circ\|^2), \tag{2.68}$$

where

$$\underset{\sim}{\ell}\,(\bar{r}_\circ, t) = \left[\frac{\partial}{\partial t}\ \underset{\sim}{\mathcal{F}}(\bar{r}_\circ, t)\right]\ \underset{\sim}{\mathcal{F}}^{-1}(\bar{r}_\circ, t) \tag{2.69}$$

is the so-called velocity gradient tensor.

Finally, substitution of (2.68) in the obvious expression

$$\delta\bar{r}|_{t+dt} = \delta\bar{r}|_t + \left(\frac{\partial}{\partial t}\ \delta\bar{r}|_t\right)\ dt, \tag{2.70}$$

gives

$$\delta\bar{r}|_{t+dt} = \overbrace{\left(\underset{\sim}{\mathcal{I}} + \underset{\sim}{\ell}\,(\bar{r}_\circ, t)\ dt\right)\ \delta\bar{r}|_t}^{\text{differential relative deformation}} + \mathcal{O}(\|\delta\bar{r}_\circ\|^2), \tag{2.71}$$

Comparison of expressions (2.12) and (2.71) shows that the differential term $\left(\underset{\sim}{\ell}\,(\bar{r}_\circ, t)\ dt\right)$ plays the role of the gradient displacement tensor $\underset{\sim}{\mathcal{J}}(\bar{r}_\circ, t)$ in the finite deformation theory. Consequently, the approximations (2.48)–(2.53), (2.56) and (2.58) proposed in the infinitesimal deformation theory become exact.

On the other hand, from (2.8) it can be easily seen that

$$\mathcal{O}(\|\delta\bar{r}|_t\|^2) = \mathcal{O}(\|\delta\bar{r}_\circ\|^2). \tag{2.72}$$

Therefore, expression (2.71) can be rewritten as

$$\delta\bar{r}|_{t+dt} = \overbrace{\left(\underset{\sim}{\mathcal{I}} + \underset{\sim}{\ell}\,(\bar{r}_\circ, t)\ dt\right)\ \delta\bar{r}|_t}^{\text{differential relative deformation}} + \mathcal{O}\left(\left\|\delta\bar{r}|_t\right\|^2\right), \tag{2.73}$$

In these conditions, the following equalities can be posed:

$$\det\big(\underset{\sim}{\mathcal{I}} + \underset{\sim}{\ell}\,(\bar{r}_{\circ}, t)\; dt\big) = \Big(1 + \mathrm{tr}\big(\underset{\sim}{\ell}\,(\bar{r}_{\circ}, t)\big)\; dt\Big), \tag{2.74}$$

$$\Big(1 + \mathrm{tr}\big(\underset{\sim}{\ell}\,(\bar{r}_{\circ}, t)\; dt\big)\Big)^{\pm 1/n} = \Big(1 \pm \frac{1}{n}\;\mathrm{tr}\big(\underset{\sim}{\ell}\,(\bar{r}_{\circ}, t)\big)\; dt\Big), \tag{2.75}$$

$$\big(\underset{\sim}{\mathcal{I}} + \underset{\sim}{\ell}\,(\bar{r}_{\circ}, t)\; dt\big)^{-1} = \big(\underset{\sim}{\mathcal{I}} - \underset{\sim}{\ell}\,(\bar{r}_{\circ}, t)\; dt\big), \tag{2.76}$$

and

$$\big(\underset{\sim}{\mathcal{I}} + \underset{\sim}{\ell}\,(\bar{r}_{\circ}, t)\; dt\big) = \big(\underset{\sim}{\mathcal{I}} + \underset{\sim}{\omega}(\bar{r}_{\circ}, t)\; dt\big)\;\big(\underset{\sim}{\mathcal{I}} + \underset{\sim}{d}(\bar{r}_{\circ}, t)\; dt\big), \tag{2.77}$$

where

$$\underset{\sim}{\omega}(\bar{r}_{\circ}, t) = \frac{1}{2}\;\Big(\underset{\sim}{\ell}\,(\bar{r}_{\circ}, t) - \underset{\sim}{\ell}^{\,T}(\bar{r}_{\circ}, t)\Big), \tag{2.78}$$

is the so-called spin tensor, and

$$\underset{\sim}{d}(\bar{r}_{\circ}, t) = \frac{1}{2}\;\Big(\underset{\sim}{\ell}\,(\bar{r}_{\circ}, t) + \underset{\sim}{\ell}^{\,T}(\bar{r}_{\circ}, t)\Big) \tag{2.79}$$

is the so-called rate of deformation tensor.

Basically, (2.74) comes from the fact that all coefficients in $\big(\underset{\sim}{\ell}\,(\bar{r}_{\circ}, t)\; dt\big)$ are differential. For its part, (2.75) is a direct consequence of the Taylor expansion of $f(x) = (1+x)^a$ for values of variable x such that $|x| << 1$.

On the other hand, (2.76) comes from

$$\big(\underset{\sim}{\mathcal{I}} + \underset{\sim}{\ell}\,(\bar{r}_{\circ}, t)\; dt\big)\;\big(\underset{\sim}{\mathcal{I}} - \underset{\sim}{\ell}\,(\bar{r}_{\circ}, t)\; dt\big) = \underset{\sim}{\mathcal{I}}. \tag{2.80}$$

Similarly, the decomposition (2.77) of tensor $\big(\underset{\sim}{\mathcal{I}} + \underset{\sim}{\ell}\,(\bar{r}_{\circ}, t)\; dt\big)$ can be easily proven by just substituting (2.78) and (2.79) in

$$\big(\underset{\sim}{\mathcal{I}} + \underset{\sim}{\omega}(\bar{r}_{\circ}, t)\; dt\big)\;\big(\underset{\sim}{\mathcal{I}} + \underset{\sim}{d}(\bar{r}_{\circ}, t)\; dt\big) = \Big(\underset{\sim}{\mathcal{I}} + \big(\underset{\sim}{\omega}(\bar{r}_{\circ}, t) + \underset{\sim}{d}(\bar{r}_{\circ}, t)\big)\; dt\Big). \tag{2.81}$$

The same principles that justify (2.74) apply to the cases of the spin tensor and the rate of deformation tensor. Thus,

$$\det\big(\underset{\sim}{\mathcal{I}} + \underset{\sim}{\omega}(\bar{r}_{\circ}, t)\; dt\big) = \Big(1 + \mathrm{tr}\big(\underset{\sim}{\omega}(\bar{r}_{\circ}, t)\big)\; dt\Big) \tag{2.82}$$

and

$$\det\big(\underset{\sim}{\mathcal{I}} + \underset{\sim}{d}(\bar{r}_{\circ}, t)\; dt\big) = \Big(1 + \mathrm{tr}\big(\underset{\sim}{d}(\bar{r}_{\circ}, t)\big)\; dt\Big). \tag{2.83}$$

From definitions (2.78) and (2.79) it is immediate to see that

$$\mathrm{tr}\big(\underset{\sim}{\omega}(\bar{r}_{\circ}, t)\big) = 0 \tag{2.84}$$

and

$$\mathrm{tr}\big(\underset{\sim}{d}(\bar{r}_{\circ}, t)\big) = \mathrm{tr}\big(\underset{\sim}{\ell}\,(\bar{r}_{\circ}, t)\big). \tag{2.85}$$

Therefore, substituting (2.84) in (2.82) gives

$$\det\big(\underset{\sim}{\mathcal{I}} + \underset{\sim}{\omega}(\bar{r}_{\circ}, t)\; dt\big) = 1 \tag{2.86}$$

while substituting (2.85) in (2.83) gives

$$\det\big(\underset{\sim}{\mathcal{I}} + \underset{\sim}{d}(\bar{r}_\circ, t)\ dt\big) = \Big(1 + \mathrm{tr}\big(\underset{\sim}{\ell}\,(\bar{r}_\circ, t)\big)\ dt\Big). \tag{2.87}$$

Recalling (2.86) and taking into account that the spin tensor (2.78) is skew-symmetric it can be proven that

$$\big(\underset{\sim}{\mathcal{I}} + \underset{\sim}{\omega}(\bar{r}_\circ, t)\ dt\big)^{T}\big(\underset{\sim}{\mathcal{I}} + \underset{\sim}{\omega}(\bar{r}_\circ, t)\ dt\big) = \underset{\sim}{\mathcal{I}} \quad \text{with} \quad \det\big(\underset{\sim}{\mathcal{I}} + \underset{\sim}{\omega}(\bar{r}_\circ, t)\ dt\big) = 1, \tag{2.88}$$

which shows that the differential relative deformation produced by tensor $\big(\underset{\sim}{\mathcal{I}} + \underset{\sim}{\omega}(\bar{r}_\circ, t)\ dt\big)$ is of rotation type.

On the other hand, taking into account that the rate of deformation tensor (2.79) is symmetric it is easy to prove

$$\big(\underset{\sim}{\mathcal{I}} + \underset{\sim}{d}(\bar{r}_\circ, t)\ dt\big)^{T} = \big(\underset{\sim}{\mathcal{I}} + \underset{\sim}{d}(\bar{r}_\circ, t)\ dt\big) \quad \text{with} \quad \big(\underset{\sim}{\mathcal{I}} + \underset{\sim}{d}(\bar{r}_\circ, t)\ dt\big) \quad \text{positive definite}, \tag{2.89}$$

which shows that the differential relative deformation produced by tensor $\big(\underset{\sim}{\mathcal{I}} + \underset{\sim}{d}(\bar{r}_\circ, t)\ dt\big)$ is of stretch type.

Therefore, the spin tensor (2.78) and the rate of deformation tensor (2.79) provide a direct and explicit procedure for performing the exact polar decomposition of tensor $\big(\underset{\sim}{\mathcal{I}} + \underset{\sim}{\ell}\,(\bar{r}_\circ, t)\ dt\big)$ as in (2.77), namely

$$\big(\underset{\sim}{\mathcal{I}} + \underset{\sim}{\ell}\,(\bar{r}_\circ, t)\ dt\big) = \big(\underset{\sim}{\mathcal{I}} + \underset{\sim}{\omega}(\bar{r}_\circ, t)\ dt\big)\ \big(\underset{\sim}{\mathcal{I}} + \underset{\sim}{d}(\bar{r}_\circ, t)\ dt\big). \tag{2.90}$$

In these terms, expression (2.73) can be rewritten as

$$\delta\bar{r}|_{t+dt} = \overbrace{\big(\underset{\sim}{\mathcal{I}} + \underset{\sim}{\omega}(\bar{r}_\circ, t)\ dt\big)}^{\text{differential rotation}}\ \overbrace{\big(\underset{\sim}{\mathcal{I}} + \underset{\sim}{d}(\bar{r}_\circ, t)\ dt\big)}^{\text{differential stretch}}\ \delta\bar{r}|_t + \mathcal{O}\big(\big\|\delta\bar{r}|_t\big\|^2\big). \tag{2.91}$$

This expression shows that the vicinity of the material particle $\bar{r}_\circ$ is first stretched by the effect of $\big(\underset{\sim}{\mathcal{I}} + \underset{\sim}{d}(\bar{r}_\circ, t)\ dt\big)$ and then rotated as a whole by the effect of $\big(\underset{\sim}{\mathcal{I}} + \underset{\sim}{\omega}(\bar{r}_\circ, t)\ dt\big)$.

The information provided by expression (2.91) is very relevant, but less revealing than it appears at first glance. In short, tensor $\big(\underset{\sim}{\mathcal{I}} + \underset{\sim}{d}(\bar{r}_\circ, t)\ dt\big)$ accounts for the differential stretching that occurs between time t and time $(t + dt)$, while tensor $\big(\underset{\sim}{\mathcal{I}} + \underset{\sim}{\omega}(\bar{r}_\circ, t)\ dt\big)$ accounts for the differential rotation that occurs between time t and time $(t+dt)$. However, neither the rate of deformation tensor $\underset{\sim}{d}(\bar{r}_\circ, t)$ is the time derivative of the Biot strain tensor $\underset{\sim}{\mathcal{E}}(\bar{r}_\circ, t)$, nor the spin tensor $\underset{\sim}{\omega}(\bar{r}_\circ, t)$ is the time derivative of the rotation tensor $\underset{\sim}{\mathcal{R}}(\bar{r}_\circ, t)$.

As in the case of the finite deformation theory, it might be useful to make further progress in an attempt to separate the parts of tensor $\big(\underset{\sim}{\mathcal{I}} + \underset{\sim}{d}(\bar{r}_\circ, t)\ dt\big)$ that explain the differential change in volume and the differential change in shape.

To achieve this, the last term of the right hand side in (2.77) is decomposed as

$$\big(\underset{\sim}{\mathcal{I}} + \underset{\sim}{d}(\bar{r}_\circ, t)\ dt\big) = \big(\underset{\sim}{\mathcal{I}} + \underset{\approx}{d_d}(\bar{r}_\circ, t)\ dt\big)\ \big(\underset{\sim}{\mathcal{I}} + h(\bar{r}_\circ, t)\ \underset{\sim}{\mathcal{I}}\ dt\big) \tag{2.92}$$

with

$$\underset{\sim}{\underset{\sim}{d}}_d(\bar{r}_\circ, t) = \big(\underset{\sim}{\underset{\sim}{d}}(\bar{r}_\circ, t) - h(\bar{r}_\circ, t)\ \underset{\sim}{\underset{\sim}{\mathcal{I}}}\big) \tag{2.93}$$

and

$$h(\bar{r}_\circ, t) = \frac{1}{n}\ \mathrm{tr}\big(\underset{\sim}{\underset{\sim}{d}}(\bar{r}_\circ, t)\big), \tag{2.94}$$

where n is the number of dimensions of the space.

It can be seen that the differential relative deformation produced by tensor $\big(\underset{\sim}{\underset{\sim}{\mathcal{I}}} + h(\bar{r}_\circ, t)\ \underset{\sim}{\underset{\sim}{\mathcal{I}}}\ dt\big)$ is of pure dilation (or isotropic stretch) type with

$$\det\big(\underset{\sim}{\underset{\sim}{\mathcal{I}}} + h(\bar{r}_\circ, t)\ \underset{\sim}{\underset{\sim}{\mathcal{I}}}\ dt\big) = \Big(1 + \mathrm{tr}\big(\underset{\sim}{\ell}\,(\bar{r}_\circ, t)\big)\ dt\Big). \tag{2.95}$$

Taking this into account and substituting (2.92) in (2.87) leads to

$$\det\big(\underset{\sim}{\underset{\sim}{\mathcal{I}}} + \underset{\sim}{\underset{\sim}{d}}_d(\bar{r}_\circ, t)\ dt\big) = 1. \tag{2.96}$$

Now it is immediate to see that the differential relative deformation produced by tensor $\big(\underset{\sim}{\underset{\sim}{\mathcal{I}}} + \underset{\sim}{\underset{\sim}{d}}_d(\bar{r}_\circ, t)\ dt\big)$ is of distortion (or isochoric stretch) type, thus satisfying

$$\big(\underset{\sim}{\underset{\sim}{\mathcal{I}}} + \underset{\sim}{\underset{\sim}{d}}_d(\bar{r}_\circ, t)\ dt\big)^{\,T} = \big(\underset{\sim}{\underset{\sim}{\mathcal{I}}} + \underset{\sim}{\underset{\sim}{d}}_d(\bar{r}_\circ, t)\ dt\big) \quad \text{with} \quad \big(\underset{\sim}{\underset{\sim}{\mathcal{I}}} + \underset{\sim}{\underset{\sim}{d}}_d(\bar{r}_\circ, t)\ dt\big) \quad \text{positive definite.} \tag{2.97}$$

Substituting (2.92) in (2.90) leads to

$$\Big(\underset{\sim}{\underset{\sim}{\mathcal{I}}} + \underset{\sim}{\ell}\,(\bar{r}_\circ, t)\ dt\Big) = \Big(\underset{\sim}{\underset{\sim}{\mathcal{I}}} + \underset{\sim}{\omega}(\bar{r}_\circ, t)\ dt\Big)\ \big(\underset{\sim}{\underset{\sim}{\mathcal{I}}} + \underset{\sim}{\underset{\sim}{d}}_d(\bar{r}_\circ, t)\ dt\big)\ \big(\underset{\sim}{\underset{\sim}{\mathcal{I}}} + h(\bar{r}_\circ, t)\ \underset{\sim}{\underset{\sim}{\mathcal{I}}}\ dt\big). \tag{2.98}$$

In these terms, expressions (2.73) and (2.91) can be rewritten as

$$\delta\bar{r}|_{t+dt} = \overbrace{\big(\underset{\sim}{\underset{\sim}{\mathcal{I}}} + \underset{\sim}{\omega}(\bar{r}_\circ, t)\ dt\big)}^{\text{differential rotation}}\ \overbrace{\big(\underset{\sim}{\underset{\sim}{\mathcal{I}}} + \underset{\sim}{\underset{\sim}{d}}_d(\bar{r}_\circ, t)\ dt\big)}^{\text{differential isochoric stretch – distorsion}}\ \overbrace{\big(\underset{\sim}{\underset{\sim}{\mathcal{I}}} + h(\bar{r}_\circ, t)\ \underset{\sim}{\underset{\sim}{\mathcal{I}}}\ dt\big)}^{\text{differential pure dilation}}\ \delta\bar{r}|_t + \mathcal{O}\big(\|\delta\bar{r}|_t\|^2\big). \tag{2.99}$$

This expression shows that the neighborhood of the material particle $\bar{r}_\circ$ is first dilated by the effect of $\big(\underset{\sim}{\underset{\sim}{\mathcal{I}}} + h(\bar{r}_\circ, t)\ \underset{\sim}{\underset{\sim}{\mathcal{I}}}\ dt\big)$, then distorted by the effect of $\big(\underset{\sim}{\underset{\sim}{\mathcal{I}}} + \underset{\sim}{\underset{\sim}{d}}_d(\bar{r}_\circ, t)\ dt\big)$ and then rotated as a whole by the effect of $\big(\underset{\sim}{\underset{\sim}{\mathcal{I}}} + \underset{\sim}{\omega}(\bar{r}_\circ, t)\ dt\big)$. For this reason tensor $\underset{\sim}{\underset{\sim}{d}}_d(\bar{r}_\circ, t)$ receives the name of rate of deviatoric deformation tensor.

Once again, the information provided by expression (2.99) is very relevant, but less revealing than it appears at first glance. In short, tensors $\big(\underset{\sim}{\underset{\sim}{\mathcal{I}}} + h(\bar{r}_\circ, t)\ \underset{\sim}{\underset{\sim}{\mathcal{I}}}\ dt\big)$ and $\big(\underset{\sim}{\underset{\sim}{\mathcal{I}}} + \underset{\sim}{\underset{\sim}{d}}_d(\bar{r}_\circ, t)\ dt\big)$ account respectively for the differential dilation and the differential distortion that occur between time t and time $(t+dt)$, while tensor $\big(\underset{\sim}{\underset{\sim}{\mathcal{I}}} + \underset{\sim}{\omega}(\bar{r}_\circ, t)\ dt\big)$ accounts for the differential rotation that occurs between time t and time $(t+dt)$. Scalar tensor $h(\bar{r}_\circ, t)$ is the time derivative of the dilation factor $\eta(\bar{r}_\circ, t)$. However, neither the rate of deviatoric

deformation tensor $\underset{\sim\sim}{d}_d(\bar{r}_\circ, t)$ is the time derivative of the deviatoric strain tensor $\underset{\sim\sim}{\mathcal{E}}_d(\bar{r}_\circ, t)$, nor the spin tensor $\underset{\sim\sim}{\omega}(\bar{r}_\circ, t)$ is the time derivative of the rotation tensor $\underset{\sim\sim}{\mathcal{R}}(\bar{r}_\circ, t)$.

Finally, unlike finite relative deformations, incremental relative deformations are exactly additive and consequently commutative, since the combined effect of the incremental relative deformations produced first by tensor $\left(\underset{\sim}{\mathcal{I}} + \underset{\sim}{\ell}_1(\bar{r}_\circ, t)\ dt\right)$ and then by tensor $\left(\underset{\sim}{\mathcal{I}} + \underset{\sim}{\ell}_2(\bar{r}_\circ, t)\ dt\right)$ is equivalent to the incremental relative deformation produced by the product

$$\left(\underset{\sim}{\mathcal{I}} + \underset{\sim}{\ell}\,(\bar{r}_\circ, t)\ dt\right) = \left(\underset{\sim}{\mathcal{I}} + \underset{\sim}{\ell}_2(\bar{r}_\circ, t)\ dt\right)\ \left(\underset{\sim}{\mathcal{I}} + \underset{\sim}{\ell}_1(\bar{r}_\circ, t)\ dt\right) = \Big(\underset{\sim}{\mathcal{I}} + \left(\underset{\sim}{\ell}_1(\bar{r}_\circ, t) + \underset{\sim}{\ell}_2(\bar{r}_\circ, t)\right)\ dt\Big). \tag{2.100}$$

In view of (2.100) it is obvious that incremental relative deformations commute. Moreover, the combined velocity gradient tensor can be expressed as

$$\underset{\sim}{\ell}\,(\bar{r}_\circ, t) = \underset{\sim}{\ell}_1(\bar{r}_\circ, t) + \underset{\sim}{\ell}_2(\bar{r}_\circ, t). \tag{2.101}$$

From (2.101) it also follows immediately that when several incremental relative deformations occur sequentially, the rate of deformation tensors add up.

2.2.6 Stress

Let $d\Gamma_\circ$ be a differential piece of surface in the undeformed geometry enclosing the material particle $\bar{r}_\circ$. Let $dA_\circ$ be its initial differential area and let $\bar{n}_\circ$ be its initial unit normal vector.

Let $d\Gamma$ be the current differential piece of surface in the deformed geometry at time t. Let dA be its current differential area and let $\bar{n}$ be its its current unit normal vector $\bar{n}$.

Let $\bar{\sigma}(\bar{r}_\circ, t, \bar{n})$ be the current stress vector (internal force per unit area) acting on $d\Gamma$ at time t. As it is known, the so-called Cauchy stress tensor $\sigma(\bar{r}_\circ, t)$ allows to express the stress vector as

$$\bar{\sigma}(\bar{r}_\circ, t, \bar{n}) = \underset{\sim}{\sigma}(\bar{r}_\circ, t)\ \bar{n}\big|_t \tag{2.102}$$

so that the differential internal force acting on $d\Gamma$ is

$$d\bar{f}\big|_t = \bar{\sigma}(\bar{r}_\circ, t, \bar{n})\ dA\big|_t = \underset{\sim}{\sigma}(\bar{r}_\circ, t)\ (dA\ \bar{n})\big|_t \tag{2.103}$$

Except in the case of exotic materials, it can be shown that the conservation of angular momentum implies that the Cauchy stress tensor must be necessarily symmetric, i.e.

$$\underset{\sim}{\sigma}^T(\bar{r}_\circ, t) = \underset{\sim}{\sigma}(\bar{r}_\circ, t). \tag{2.104}$$

Finally, the Cauchy stress tensor $\underset{\sim}{\sigma}(\bar{r}_\circ, t)$ can be decomposed as the sum of an isotropic part (pressure) and a deviatoric part (shear) in the form

$$\underset{\sim}{\sigma}(\bar{r}_\circ, t) = \overbrace{p(\bar{r}_\circ, t)\ \underset{\sim}{\mathcal{I}}}^{\text{pressure}} + \overbrace{\underset{\sim\sim}{\sigma}_d(\bar{r}_\circ, t)}^{\text{shear}}, \qquad \text{with} \quad \begin{cases} p(\bar{r}_\circ, t) = \dfrac{1}{n}\ \mathrm{tr}\big(\underset{\sim}{\sigma}(\bar{r}_\circ, t)\big), \\ \underset{\sim\sim}{\sigma}_d(\bar{r}_\circ, t) = \big(\underset{\sim}{\sigma}(\bar{r}_\circ, t) - p(\bar{r}_\circ, t)\ \underset{\sim}{\mathcal{I}}\big), \end{cases} \tag{2.105}$$

where n is the number of dimensions of the space.

Broadly speaking, the current value $\underset{\sim}{\sigma}(\bar{r}_\circ, t)$ of the stress tensor associated to each material particle $\bar{r}_\circ$ at time t will depend on the stress-strain history of the material in the region near the particle. In turn, the stress-strain history is the internal response to the external forces (including inertial effects, if any) acting on the material over time.

The relationships that describe the evolution of stresses in terms of the evolution of relative deformations are called constitutive equations and are characteristic of each given material. Note that the presented description of the Cauchy stress tensor is Lagrangian (or material), since the tensor is defined in terms of the initial coordinates of the material particle being considered, although both vector $\bar{n}$ and stress vector $\bar{\sigma}(\bar{r}_\circ, t)$ correspond to the deformed geometry.

Other stress tensors are intended to provide the differential internal force (2.103) in terms of different configurations. In particular, the second Piola-Kirchhoff stress tensor is defined as

$$\underset{\sim}{S}(\bar{r}_\circ, t) = \underset{\sim}{\mathcal{F}}(\bar{r}_\circ, t)\ \underset{\sim}{\mathcal{F}}^{-1}(\bar{r}_\circ, t)\ \underset{\sim}{\sigma}(\bar{r}_\circ, t)\ \underset{\sim}{\mathcal{F}}^{-T}(\bar{r}_\circ, t). \tag{2.106}$$

The above expression allows the calculation of the second Piola-Kirchhoff stress tensor from the Cauchy stress tensor. In addition, expression (2.106) shows that the second Piola-Kirchhoff stress tensor $\underset{\sim}{S}(\bar{r}_\circ, t)$ is symmetric as long as the Cauchy stress tensor $\underset{\sim}{\sigma}(\bar{r}_\circ, t)$ is symmetric too. Inverting this relationship gives

$$\underset{\sim}{\sigma}(\bar{r}_\circ, t) = \frac{1}{\mathcal{F}(\bar{r}_\circ, t)}\ \underset{\sim}{\mathcal{F}}(\bar{r}_\circ, t)\ \underset{\sim}{S}(\bar{r}_\circ, t)\ \underset{\sim}{\mathcal{F}}^{T}(\bar{r}_\circ, t), \tag{2.107}$$

what allows the calculation of the Cauchy stress tensor from the second Piola-Kirchhoff stress tensor. Taking into account (2.15) it is straightforward to show that the differential internal force (2.103) acting on $d\Gamma$ can be expressed as

$$d\bar{f}|_t = \underset{\sim}{\mathcal{F}}(\bar{r}_\circ, t)\ d\bar{f}_\circ|_t \tag{2.108}$$

where

$$d\bar{f}_\circ|_t = \bar{s}(\bar{r}_\circ, t, \bar{n}_\circ)\ dA_\circ \tag{2.109}$$

and

$$\bar{s}(\bar{r}_\circ, t, \bar{n}_\circ) = \underset{\sim}{S}(\bar{r}_\circ, t)\ \bar{n}_\circ. \tag{2.110}$$

Expressions (2.108)–(2.110) show that the second Piola-Kirchhoff stress tensor $\underset{\sim}{S}(\bar{r}_\circ, t)$ allows for expressing the differential internal force (2.103) in terms of the differential area and the unit normal vector in the initial configuration.

Expressions (2.106) and (2.107) show that there is a biunivocal relationship between the second Piola-Kirchhoff stress tensor and the Cauchy Green stress tensor, so that either of them can be used as a basis for establishing the formulation.

As we shall see below, it is possible to write the structural analysis problem in terms of the Cauchy stress tensor $\underset{\sim}{\sigma}(\bar{r}_\circ, t)$ and the tensors (rotation $\underset{\sim}{\mathcal{R}}(\bar{r}_\circ, t)$ and Biot strain $\underset{\sim}{\mathcal{E}}(\bar{r}_\circ, t)$) emerging from the deformation gradient tensor (2.9) by means of decomposition (2.23) of the deformation gradient. But it is also possible, in effect, to rewrite the problem in terms of the second Piola-Kirchhoff stress tensor $\underset{\sim}{S}(\bar{r}_\circ, t)$ and the Green strain tensor

$\underset{\sim}{E}(\bar{r}_{\circ},t)$ defined in (2.36). The latter approach has the advantage that it does not require performing polar decomposition (2.22).

Also significantly, by taking into account approximations (2.48) and (2.50) it is easy to show that when assumption (2.46) is fulfilled, expressions (2.106) and (2.107) reduce to

$$\underset{\sim}{S}(\bar{r}_{\circ},t) \approx \underset{\sim}{\sigma}(\bar{r}_{\circ},t), \tag{2.111}$$

what proves that the second Piola-Kirchhoff stress tensor $\underset{\sim}{S}(\bar{r}_{\circ},t)$ and the Cauchy stress tensor $\underset{\sim}{\sigma}(\bar{r}_{\circ},t)$ are indistinguishable in the framework of the infinitesimal deformation theory.

Substituting (2.26) and (2.23) in (2.106) leads to a first alternative expression for the second Piola-Kirchhoff stress tensor

$$\underset{\sim}{S}(\bar{r}_{\circ},t) = \det\big(\underset{\sim}{\mathcal{I}}+\underset{\sim}{\mathcal{E}}(\bar{r}_{\circ},t)\big)\,\big(\underset{\sim}{\mathcal{I}}+\underset{\sim}{\mathcal{E}}(\bar{r}_{\circ},t)\big)^{-1}\,\underset{\sim}{\mathcal{R}}^{T}(\bar{r}_{\circ},t)\,\underset{\sim}{\sigma}(\bar{r}_{\circ},t)\,\underset{\sim}{\mathcal{R}}(\bar{r}_{\circ},t)\,\big(\underset{\sim}{\mathcal{I}}+\underset{\sim}{\mathcal{E}}(\bar{r}_{\circ},t)\big)^{-1} \tag{2.112}$$

in terms of the Biot strain tensor $\underset{\sim}{\mathcal{E}}(\bar{r}_{\circ},t)$ and the rotation tensor $\underset{\sim}{\mathcal{R}}(\bar{r}_{\circ},t)$.

And finally, substituting (2.20) and (2.34) in (2.106) leads to a second alternative expression for the second Piola-Kirchhoff stress tensor

$$\underset{\sim}{S}(\bar{r}_{\circ},t) = \big(1+\eta(\bar{r}_{\circ},t)\big)^{n-2}\,\big(\underset{\sim}{\mathcal{I}}+\underset{\sim}{\mathcal{E}}_{d}(\bar{r}_{\circ},t)\big)^{-1}\,\underset{\sim}{\mathcal{R}}^{T}(\bar{r}_{\circ},t)\,\underset{\sim}{\sigma}(\bar{r}_{\circ},t)\,\underset{\sim}{\mathcal{R}}(\bar{r}_{\circ},t)\,\big(\underset{\sim}{\mathcal{I}}+\underset{\sim}{\mathcal{E}}_{d}(\bar{r}_{\circ},t)\big)^{-1} \tag{2.113}$$

in terms of the dilation factor $\eta(\bar{r}_{\circ},t)$, the distortion tensor $\underset{\sim}{\mathcal{E}}_{d}(\bar{r}_{\circ},t)$ and the rotation tensor $\underset{\sim}{\mathcal{R}}(\bar{r}_{\circ},t)$.

In static or quasi-static problems, the external and internal forces (stresses) must be in equilibrium. The equilibrium equation is a particularization of Euler's Conservation Equation. In solid mechanics it is commonly known as Cauchy's Equation.

In general, it will be necessary to take into account the changes in density induced by the deformation. For this, it will be necessary to impose the continuity equation in addition to the equilibrium equation. The continuity equation is another particularization of Euler's Equation. In static or quasi-static problems of solid mechanics and in the absence of other effects, the continuity equation can be integrated analytically. Also, depending on the nature of the problem it may be necessary to take into account other variables (e.g. temperature), which would require the imposition of the corresponding additional equations (e.g. the heat transfer equation).

As it was seen above, relative deformation in the vicinity of a material particle is the combined effect of dilation, distortion and rotation. Intuitively it is postulated that dilation and distortion can lead to changes in the stress value, while rotation should only contribute to change the orientation of the stress in space.

In elastic materials the relative deformation in the vicinity of each point determine the stress, independently on the deformation history. Therefore, when the stress disappears the deformation is reversed. In plastic materials part of the relative deformation in the vicinity of each point can increase arbitrarily and become permanent when a certain maximum stress level is reached. Therefore, even when the stress disappears part of the relative deformation can remain, In these conditions, not only the actual deformation but also the deformation history is relevant to determine the current strain-stress state of

the material. The relations that connect the relative deformation and the stress are the so-called constitutive equations.

2.2.7 Equilibrium and continuity equations for static and quasi-static problems

The equilibrium equation (i.e., the equation of conservation of linear momentum) is originally stated from the Eulerian (or spatial) descriptions of the magnitudes involved.

Let $f(\bar{r}_\circ, t)$ be the Lagrangian (or material) description (i.e., a function defined in terms of the initial coordinates $\bar{r}_\circ$ of the material particle being considered and the time t) of an arbitrary magnitude (whether scalar, vector, matrix or higher order). Let $f_{_E}(\bar{r}, t)$ be the Eulerian (or spatial) description of the same magnitude (i.e., a function defined in terms of the spatial coordinates $\bar{r}$ and the time t).

Taking into account (2.1), the relation between the two descriptions, Lagrangian and Eulerian, of the same magnitude is given by the expression

$$f(\bar{r}_\circ, t) = f_{_E}(\bar{r}, t)\Big|_{\bar{r} = \bar{\chi}(\bar{r}_\circ, t)}. \tag{2.114}$$

Let $\underset{\sim\sim}{\sigma}_{_E}(\bar{r}, t)$ be the Eulerian (or spatial) counterpart of the Lagrangian (or material) description of the Cauchy stress tensor $\underset{\sim}{\sigma}(\bar{r}_\circ, t)$, according to (2.114).

When the time variation is very slow and the inertial terms are considered to be negligible, as in this case where the problem is said to be of a quasi-static type. In these cases, the equilibrium equation reduces to

$$\overline{\mathrm{div}}\big(\underset{\sim\sim}{\sigma}_{_E}(\bar{r}, t)\big) + \bar{b}_{_E}(\bar{r}, t) = \bar{0}, \tag{2.115}$$

where $\bar{b}_{_E}(\bar{r}, t)$ represents the external force per unit volume acting at point $\bar{r}$.

The above equation does not include the terms corresponding to time variations. Therefore, (2.115) is only valid in the strict sense when the problem is static. However, it is assumed that it can be used as an accurate and suitable simplification of the complete equilibrium equation when the problem is quasi-static.

In Computational Engineering, differential equation (2.115) is reformulated as an integral equation by the application of the weighted residual method. Then, the order of derivation of the resultant expression is reduced by applying the divergence theorem. The result is said to be a weak form of equation (2.115). Since the description of the involved variables is originally Lagrangian, it is most convenient to perform the necessary transformations to rewrite equation (2.115) in terms of the Lagrangian descriptions of the Cauchy stress tensor $\underset{\sim}{\sigma}(\bar{r}_\circ, t)$ and the external force $\bar{b}(\bar{r}_\circ, t)$. If this is done, the polar decomposition of the deformation gradient tensor $\underset{\sim}{\mathcal{F}}(\bar{r}_\circ, t)$ is mandatory since the work-conjugate strain tensor in this case is the Biot strain tensor $\underset{\sim}{\mathcal{E}}(\bar{r}_\circ, t)$. Equivalently, equation (2.115) can be rewritten in terms of the second Piola-Kirchhoff stress tensor $\underset{\sim}{S}(\bar{r}_\circ, t)$ and the external force $\bar{b}(\bar{r}_\circ, t)$. The work-conjugate strain tensor in this case is the Green strain tensor $\underset{\sim}{E}(\bar{r}_\circ, t)$, what excludes the need for performing the polar decomposition.

On the other hand, it can be shown that imposing the rotational equilibrium equation is equivalent to the condition (2.104). Therefore, the need to impose this equation is avoided if the symmetry of the Cauchy stress tensor is imposed when the constitutive equation is defined. In this kind of static or quasi-static problems of solid mechanics, and in the absence of other effects, the continuity equation can be integrated analytically.

Indeed, if $\rho(\bar{r}_o, t)$ is the Lagrangian description of the density it is obvious that

$$\rho(\bar{r}_o, t)\ dV|_t = \rho(\bar{r}_o, 0)\ dV_0. \tag{2.116}$$

Then, taking (2.13) into account leads immediately to the expression for the density

$$\rho(\bar{r}_o, t) = \frac{1}{\mathcal{F}(\bar{r}_o, t)}\ \rho(\bar{r}_o, 0) \tag{2.117}$$

in terms of the determinant of the deformation gradient tensor $\mathcal{F}(\bar{r}_o, t)$.

2.2.8 Constitutive equations in elasticity

A material is said to be of type Cauchy-elastic, or simply elastic, when the stress tensor is determined by the current relative deformations in the vicinity of each point, not depending on the deformation history nor on the rate at wich the deformation progresses.

Since relative deformations are determined by the deformation gradient tensor $\underset{\sim}{\mathcal{F}}$, the constitutive equation of an elastic material takes the general form

$$\underset{\sim}{\sigma} = \underset{\sim}{\psi}(\underset{\sim}{\mathcal{F}}) \qquad \text{with} \quad \underset{\sim}{\psi}^T(\underset{\sim}{\mathcal{F}}) = \underset{\sim}{\psi}(\underset{\sim}{\mathcal{F}}). \tag{2.118}$$

It seems obvious that an arbitrary rotation superimposed on the deformation tensor should not alter the magnitude of the stress tensor given in (2.118), but only its orientation in space. Therefore, tensorial function $\underset{\sim}{\psi}(\underset{\sim}{\mathcal{F}})$ given in (2.118) must verify the so-called objectivity condition

$$\underset{\sim}{\psi}(\underset{\sim}{Q}\ \underset{\sim}{\mathcal{F}}) = \underset{\sim}{Q}\ \underset{\sim}{\psi}(\underset{\sim}{\mathcal{F}})\ \underset{\sim}{Q}^T \qquad \forall \underset{\sim}{Q}\ \ / \ \ \underset{\sim}{Q}^T = \underset{\sim}{Q}^{-1}. \tag{2.119}$$

Objectivity is often confused with frame-invariance, i.e. the validity of the same form of the equation for any orthogonal Cartesian basis $\{\vec{i}, \vec{j}, \vec{k}\}$ in the Euclidean space $\mathcal{R}^3$. The authentic frame-invariance requires that all involved magnitudes are of tensorial character, but also that function $\underset{\sim}{\psi}(\underset{\sim}{\mathcal{F}})$ is linear or depends exclusively on the invariants of tensor $\underset{\sim}{\mathcal{F}}$. As will be evident, these conditions are met in the case of linear elasticity.

In view of (2.23) it is evident that the constitutive equations type (2.118) can be expressed alternatively in terms of the Biot strain tensor $\underset{\sim}{\mathcal{E}}$ and the rotation tensor $\underset{\sim}{\mathcal{R}}$. In this case, the objectivity condition (2.119) forces the constitutive equation of an elastic material to have the specific form

$$\underset{\sim}{\sigma} = \underset{\sim}{\mathcal{R}}\ \underset{\sim}{\beta}(\underset{\sim}{\mathcal{E}})\ \underset{\sim}{\mathcal{R}}^T \qquad \text{with} \quad \underset{\sim}{\beta}^T(\underset{\sim}{\mathcal{E}}) = \underset{\sim}{\beta}(\underset{\sim}{\mathcal{E}}), \quad \underset{\sim}{\beta}(\underset{\sim\sim}{\mathcal{E}}_{pre}) = \underset{\sim\sim}{\sigma}_{pre}, \tag{2.120}$$

where $\underset{\sim\sim}{\mathcal{E}}_{pre}$ and $\underset{\sim\sim}{\sigma}_{pre}$ are, respectively the pre-existing values, if applicable, of the Biot strain tensor and the Cauchy stress tensor before the strain under consideration was produced.

Substituting (2.120) in (2.112) gives

$$\underset{\sim}{S} = \det\left(\underset{\sim}{\mathcal{I}} + \underset{\sim}{\mathcal{E}}\right)\ \left(\underset{\sim}{\mathcal{I}} + \underset{\sim}{\mathcal{E}}\right)^{-1}\ \underset{\sim}{\beta}(\underset{\sim}{\mathcal{E}})\ \left(\underset{\sim}{\mathcal{I}} + \underset{\sim}{\mathcal{E}}\right)^{-1} \tag{2.121}$$

According to (2.41) the Green strain tensor $\underset{\sim}{E}$ can be expressed in terms of the Biot strain tensor $\underset{\sim}{\mathcal{E}}$ as

$$\underset{\sim}{E} = \underset{\sim}{\mathcal{E}}\ \left(\underset{\sim}{\mathcal{I}} + \frac{1}{2}\ \underset{\sim}{\mathcal{E}}\right). \tag{2.122}$$

By inverting (2.122) the Biot strain tensor $\underset{\sim}{\mathcal{E}}$ can be expressed in terms of the Green strain tensor $\underset{\sim}{E}$ as

$$\underset{\sim}{\mathcal{E}} = \left((\underset{\sim}{\mathcal{I}} + 2\,\underset{\sim}{E})^{1/2} - \underset{\sim}{\mathcal{I}}\right). \tag{2.123}$$

Therefore, the constitutive equation type (2.120) of an elastic material can also be expressed as

$$\underset{\sim}{S} = \underset{\sim}{\Psi}(\underset{\sim}{E}) \qquad \text{with} \quad \underset{\sim}{\Psi}^{T}(\underset{\sim}{E}) = \underset{\sim}{\Psi}(\underset{\sim}{E}). \tag{2.124}$$

where the second Piola-Kirchhoff stress tensor $\underset{\sim}{S}$ is given in terms of the Green strain tensor $\underset{\sim}{E}$ by the function

$$\underset{\sim}{\Psi}(\underset{\sim}{E}) = \det\left(\underset{\sim}{\mathcal{I}} + 2\,\underset{\sim}{E}\right)^{-1/2}\ (\underset{\sim}{\mathcal{I}} + 2\,\underset{\sim}{E})^{-1/2}\ \underset{\sim}{\beta}(\underset{\sim}{\mathcal{E}})\ (\underset{\sim}{\mathcal{I}} + 2\,\underset{\sim}{\mathcal{E}})^{-1/2} \quad \text{with } \underset{\sim}{\mathcal{E}} = \left(\left(\underset{\sim}{\mathcal{I}} + 2\,\underset{\sim}{E}\right)^{1/2} - \underset{\sim}{\mathcal{I}}\right). \tag{2.125}$$

Solving the function $\underset{\sim}{\beta}(\underset{\sim}{\mathcal{E}})$ in terms of function $\underset{\sim}{\Psi}(\underset{\sim}{E})$in (2.125) gives

$$\underset{\sim}{\beta}(\underset{\sim}{\mathcal{E}}) = \det\left(\underset{\sim}{\mathcal{I}} + \underset{\sim}{\mathcal{E}}\right)^{-1}\ (\underset{\sim}{\mathcal{I}} + \underset{\sim}{\mathcal{E}})\ \underset{\sim}{\Psi}(\underset{\sim}{E})\ (\underset{\sim}{\mathcal{I}} + \underset{\sim}{\mathcal{E}}) \quad \text{with } \underset{\sim}{E} = \underset{\sim}{\mathcal{E}}\ \left(\underset{\sim}{\mathcal{I}} + \frac{1}{2}\ \underset{\sim}{\mathcal{E}}\right), \tag{2.126}$$

what proves that expressions (2.120) and (2.124) are equivalent. As a consequence, constitutive equations type (2.124) are automatically objective.

In the so-called hyperelastic models the second Piola-Kirchhoff stress tensor $\underset{\sim}{S}$ is obtained by taking derivatives of a suitable stored elastic energy function $\mathcal{W}(\underset{\sim}{E})$ of the Green strain tensor $\underset{\sim}{E}$ in the form

$$\underset{\sim}{S} = \underset{\sim}{\Psi}(\underset{\sim}{E}) = \frac{\partial}{\partial \underset{\sim}{E}}\ \mathcal{W}(\underset{\sim}{E}). \tag{2.127}$$

On the other hand, a material is said to be of type linear elastic when function $\underset{\sim}{\beta}(\underset{\sim}{\mathcal{E}})$ in (2.120) is linear. In this case, function $\underset{\sim}{\beta}(\underset{\sim}{\mathcal{E}})$ takes the general form

$$\underset{\sim}{\beta}(\underset{\sim}{\mathcal{E}}) = \underset{\sim}{C} : \underset{\sim}{\mathcal{E}}, \tag{2.128}$$

where $\underset{\sim}{C}$ and $\underset{\sim}{\mathcal{E}}$ are the components of a 4th-order constant tensor and a 2nd-order tensor, respectively, type

$$\underset{\sim}{C} = \left[c^{\,i}{}_{j\alpha}{}^{\beta}\right], \qquad \underset{\sim}{\mathcal{E}} = \left[\varepsilon^{\,\alpha}{}_{\beta}\right]. \tag{2.129}$$

From (2.27) and (2.102) it follows that matrices $\underset{\sim}{\mathcal{E}}$ and $\underset{\sim}{\sigma}$ are the contravariant-covariant expressions of the Biot strain tensor and the Cauchy stress tensor respectively. The colon symbol (:) in (2.129) stands for the double-dot tensor product or double contraction, so that the unrotated Cauchy stress tensor can be written in index notation using Einstein summation convention as

$$\underset{\sim}{\beta}(\underset{\sim}{\mathcal{E}}) = \left[c^{i}{}_{j\alpha}{}^{\beta} \;\; \varepsilon^{\alpha}{}_{\beta} \right]. \tag{2.130}$$

A quite simple constitutive model can be stated as

$$\underset{\sim}{\beta}(\underset{\sim}{\mathcal{E}}) = K\ (\mathcal{F}-1)\ \underset{\sim}{I} + 2\ \mu\ \underset{\sim\sim}{\mathcal{E}}_{d}, \qquad \text{with} \quad \begin{cases} \mathcal{F} = \det(\underset{\sim}{\mathcal{I}} + \underset{\sim}{\mathcal{E}}) \\ \underset{\sim\sim}{\mathcal{E}}_{d} = \dfrac{1}{1+\eta}\ (\underset{\sim}{\mathcal{E}} - \eta\ \underset{\sim}{\mathcal{I}}), \\ \eta = (\mathcal{F})^{1/n} - 1, \end{cases} \tag{2.131}$$

where the unrotated Cauchy stress tensor is obtained as the sum of an isotropic part (pressure) that is proportional to the unitary change in volume $(\mathcal{F}-1)$ and a deviatoric part (shear) that is proportional to the deviatoric strain tensor $\underset{\sim\sim}{\mathcal{E}}_{d}$ given in (2.29). Parameters K and μ in (2.131) receive the names of bulk modulus and Lame's second parameter, respectively.

In such a case, (2.118) takes the form

$$\underset{\sim}{\beta}(\underset{\sim}{\mathcal{E}}) \approx \underset{\sim}{\beta}(\widehat{\underset{\sim}{\mathcal{E}}}) \tag{2.132}$$

in terms of the infinitesimal Biot strain tensor $\widehat{\underset{\sim}{\mathcal{E}}}$ given in (2.53). Substituting approximations (2.58) and (2.46) in (2.132) and taking

$$\lambda = K - 2\mu/n, \tag{2.133}$$

where n is the number of dimensions of the space, expression (2.132) can be rewritten in the compact form

$$\underset{\sim}{\beta}(\widehat{\underset{\sim}{\mathcal{E}}}) = \lambda\ \operatorname{tr}(\widehat{\underset{\sim}{\mathcal{E}}})\ \underset{\sim}{I} + 2\ \mu\ \widehat{\underset{\sim}{\mathcal{E}}}, \tag{2.134}$$

where the constants λ and μ are the so-called Lame's parameters. The above expression is clearly a particular case (isotropic) of the general linear elastic model (2.130).

2.2.9 Procedures for solving elasticity problems

If the problem is static, it is only necessary to solve it once, since its solution is constant in time. On the oposite, if the problem is quasi-static, it will be necessary to solve it as if it were static for each instant of time in which we wish to know the solution.

The term linear elasticity refers to the class of problems in which the displacements (2.3) are small, the condition (2.46) is verified. So, the infinitesimal deformation theory can be applied, and function $\underset{\sim}{\beta}(\underset{\sim}{\mathcal{E}})$ in the constitutive equation (2.120) is linear, so that it can be written in the form (2.128).

Although it is mathematically possible, situations in which the displacements (2.3) are small but the displacement gradients (2.11) are not infinitesimal do not occur in reality.

Moreover, when the displacement gradients are infinitesimal the aproximation (2.53) can be applied, so the Biot strain tensor $\underset{\sim}{\mathcal{E}}$ is infinitesimal as well. Under these conditions it is reasonable to use a constitutive model type (2.120) in which the function $\underset{\sim}{\beta}(\underset{\sim}{\mathcal{E}})$ is linear. Thus, in practice it is sufficient that the displacements (2.3) are small for the problem to be of linear elasticity.

To get the solution to a linear elasticity problem at a given time t by means of a Computational Engineering method, the following steps can be carried out:

1. The values of the nodal displacements $\bar{u}^{\text{ip}}(t)$ are considered as unknowns.
2. The displacements $\bar{u}(\bar{r}_{\text{o}}, t)$ are approximated as shown in (2.4).
3. The displacement gradient tensor $\underset{\sim\sim}{\mathcal{J}}(\bar{r}_{\text{o}}, t)$ is formulated as shown in (2.21).
4. The rotation tensor $\underset{\sim\sim}{\mathcal{R}}(\bar{r}_{\text{o}}, t)$ is approximated as shown in (2.52).
5. The Biot strain tensor $\underset{\sim}{\mathcal{E}}(\bar{r}_{\text{o}}, t)$ is approximated as shown in (2.53).
6. The dilation factor $\eta(\bar{r}_{\text{o}}, t)$ is approximated as shown in (2.58).
7. The Cauchy stress tensor $\underset{\sim}{\sigma}(\bar{r}_{\text{o}}, t)$ is formulated as shown in (2.120). The effect of the rotation tensor can be neglected, since it gives rise to higher order infinitesimals, so the constitutive equation (2.120) reduces to

$$\underset{\sim}{\sigma} = \underset{\sim}{\beta}(\underset{\sim}{\mathcal{E}}) \qquad \text{with} \quad \underset{\sim}{\beta}^{T}(\underset{\sim}{\mathcal{E}}) = \underset{\sim}{\beta}(\underset{\sim}{\mathcal{E}}), \quad \underset{\sim}{\beta}(\underset{\sim\sim}{\mathcal{E}_{pre}}) = \underset{\sim\sim}{\sigma_{pre}}, \tag{2.135}$$

   where

$$\underset{\sim}{\beta}(\underset{\sim}{\mathcal{E}}) = \underset{\sim}{\mathcal{C}} : \underset{\sim}{\mathcal{E}}, \tag{2.136}$$

8. The above information is introduced in the weak form of the equilibrium equation (2.115). At this point the approximation $\bar{r} \approx \bar{r}_{\text{o}}$ can be applied, since the displacements $\bar{u}(\bar{r}_{\text{o}}, t)$ are small. This approach is equivalent to ignoring the deformation when establishing the equilibrium. In other words, the equilibrium is established in the non-deformed geometry.
9. Since all the above formulations are linear, the result is a linear system of equations whose unknowns are precisely the nodal displacements $\bar{u}^{\text{ip}}(t)$. Therefore, solving this linear system will solve the problem.

The term non linear elasticity refers to the class of problems in which the displacements (2.3) are not small, or the condition (2.46) is not verified, so that the finite deformation theory must be applied, or function $\underset{\sim}{\beta}(\underset{\sim}{\mathcal{E}})$ in the constitutive equation (2.120) is not linear, so that it can not be written in the form (2.128).

Although it is mathematically possible, situations in which the displacements (2.3) are not small but the displacement gradients (2.11) are infinitesimal are unfrequent in reality. Moreover, when the displacement gradients are not infinitesimal the aproximation (2.53) can not be applied, so the Biot strain tensor $\mathcal{E}$ is not infinitesimal as a general rule. Under

these conditions it might be unreasonable to use a constitutive model type (2.120) in which the function $\underset{\sim}{\beta}(\underset{\sim}{\mathcal{E}})$ is linear. Thus, in practice it is sufficient that the displacements (2.3) are large for the problem to be a full non linear elasticity problem.

To get the solution to the elasticity problem at a given time t by means of a Computational Engineering method, the following steps can be carried out:

1. Starting values are estimated for the nodal displacements $\bar{u}^{\text{ip}}(t)$.
2. The approximated solution $\bar{u}^h(\bar{r}_\circ, t)$ is constructed as shown in (2.4).
3. The displacement gradient tensor $\underset{\sim}{\mathcal{J}}(\bar{r}_\circ, t)$ is calculated as shown in (2.21).
4. The deformation gradient tensor $\underset{\sim}{\mathcal{F}}(\bar{r}_\circ, t)$ is calculated as shown in (2.10).
5. The volume expansion factor $\mathcal{F}(\bar{r}_\circ, t)$ is calculated as shown in (2.14).
6. The Green strain tensor $\underset{\sim}{E}(\bar{r}_\circ, t)$ is calculated as shown in (2.36).
7. The second Piola-Kirchhoff stress tensor $\underset{\sim}{S}(\bar{r}_\circ, t)$ is calculated by means of a suitable constitutive equation as shown in (2.124).
8. With the above information, it is checked whether the weak form of the equilibrium equation (2.115) is verified within certain tolerances.
9. If the above check fails, the value of the nodal displacements $\bar{u}^{\text{ip}}(t)$ are corrected by adding suitable increments $\Delta\bar{u}^{\text{ip}}(t)$.
10. Steps 2 to 9 are iterated until convergence.

The variables involved in steps 2–7 must be calculated for the initial coordinates $\bar{r}_\circ$ of each integration point, since this is the information required to perform step number 8.

I

2.2.10 Rate of strain and rate of elastic stress

From (2.8) and (2.102) it follows that matrices $\underset{\sim}{\mathcal{F}}$ and $\underset{\sim}{\sigma}$ are the contravariant-covariant expressions of the deformation gradient tensor and the Cauchy stress tensor respectively. Thus,

$$\underset{\sim}{\mathcal{F}} = \left[F^{\alpha}{}_{\beta}\right], \qquad \underset{\sim}{\sigma} = \left[\sigma^{i}{}_{j}\right]. \tag{2.137}$$

Taking derivatives in (2.118) gives

$$d\underset{\sim}{\sigma} = \frac{\partial \underset{\sim}{\psi}}{\partial \underset{\sim}{\mathcal{F}}} \; : \; d\underset{\sim}{\mathcal{F}}, \tag{2.138}$$

where the derivative of the function $\underset{\sim}{\psi}(\underset{\sim}{\mathcal{F}})$ with respect to the deformation gradient tensor $\underset{\sim}{\mathcal{F}}$ is expressed as the 4th-order tensor

$$\frac{\partial \underset{\sim}{\psi}}{\partial \underset{\sim}{\mathcal{F}}} = \left[\frac{\partial \psi^{\,i}{}_{j}}{\partial F^{\,\alpha}{}_{\beta}}\right]. \tag{2.139}$$

The colon symbol ":" in (2.138) stands for the double-dot tensor product or double contraction, so that the equivalent expression to (2.138) in index notation can be written using Einstein summation convention as

$$d\sigma^{\,i}{}_{j} = \frac{\partial \psi^{\,i}{}_{j}}{\partial F^{\,\alpha}{}_{\beta}}\; dF^{\,\alpha}{}_{\beta}. \tag{2.140}$$

Consequently, if the deformation gradient tensor $\underset{\sim}{\mathcal{F}}$ undergoes a variation

$$d\underset{\sim}{\mathcal{F}} = \dot{\underset{\sim}{\mathcal{F}}}\; dt \tag{2.141}$$

between time t and time $(t + dt)$, the Cauchy stress tensor $\underset{\sim}{\sigma}$ will undergo a variation

$$d\underset{\sim}{\sigma} = \dot{\underset{\sim}{\sigma}}\; dt \tag{2.142}$$

in the same time interval, where the Cauchy stress rate $\dot{\underset{\sim}{\sigma}}$ can be written in terms of the deformation gradient rate $\dot{\underset{\sim}{\mathcal{F}}}$ as

$$\dot{\underset{\sim}{\sigma}} = \frac{\partial \underset{\sim}{\psi}}{\partial \underset{\sim}{\mathcal{F}}} \;:\; \dot{\underset{\sim}{\mathcal{F}}}. \tag{2.143}$$

The equivalent expression to (2.143) in index notation can be written using Einstein summation convention as

$$\dot{\sigma}^{\,i}{}_{j} = \frac{\partial \psi^{\,i}{}_{j}}{\partial F^{\,\alpha}{}_{\beta}}\; dF^{\,\alpha}{}_{\beta}, \tag{2.144}$$

In a similar way, from (2.38) and (2.108)–(2.110) it follows that matrices $\underset{\sim}{E}$ and $\underset{\sim}{S}$ are the covariant-covariant and contravariant-covariant expressions respectively of the Green strain tensor and the second Piola-Kirchhoff stress tensor. Thus,

$$\underset{\sim}{E} = \left[E_{\,\alpha\beta}\right], \qquad \underset{\sim}{S} = \left[S^{\,i}{}_{j}\right]. \tag{2.145}$$

Taking derivatives in (2.36) gives

$$d\underset{\sim}{E} = \frac{1}{2}\left(d\underset{\sim}{\mathcal{F}}^{T}\,\underset{\sim}{\mathcal{F}} + \underset{\sim}{\mathcal{F}}^{T}\,d\underset{\sim}{\mathcal{F}}\right) \tag{2.146}$$

Therefore, if the deformation gradient tensor $\underset{\sim}{\mathcal{F}}$ undergoes a variation type (2.141) between time t and time $(t + dt)$, the Green strain tensor $\underset{\sim}{E}$ will undergo a variation

$$d\underset{\sim}{E} = \dot{\underset{\sim}{E}}\; dt \tag{2.147}$$

in the same time interval, where

$$\dot{E} = \frac{1}{2}\left(\dot{\underset{\sim}{\mathcal{F}}}^T \underset{\sim}{\mathcal{F}} + \underset{\sim}{\mathcal{F}}^T \dot{\underset{\sim}{\mathcal{F}}}\right). \tag{2.148}$$

Taking derivatives in (2.124) gives

$$d\underset{\sim}{S} = \frac{\partial \underset{\sim}{\Psi}}{\partial \underset{\sim}{E}} \;:\; d\underset{\sim}{E}, \tag{2.149}$$

where the derivative of the function $\underset{\sim}{\Psi}(\underset{\sim}{E})$ with respect to the Green strain tensor $\underset{\sim}{E}$ is expressed as the 4th-order tensor

$$\frac{\partial \underset{\sim}{\Psi}}{\partial \underset{\sim}{E}} = \left[\frac{\partial \Psi^{\,i}{}_{j}}{\partial E_{\,\alpha\beta}}\right]. \tag{2.150}$$

The colon symbol ":" in (2.149) stands for the double-dot tensor product or double contraction. The equivalent expression to (2.149) in index notation can be written using Einstein summation convention as

$$dS^{\,i}{}_{j} = \frac{\partial \Psi^{\,i}{}_{j}}{\partial E_{\,\alpha\beta}}\, dE_{\,\alpha\beta}. \tag{2.151}$$

Consequently, if the Green strain tensor $\underset{\sim}{E}$ undergoes a variation

$$d\underset{\sim}{E} = \dot{\underset{\sim}{E}}\, dt \tag{2.152}$$

between time t and time $(t + dt)$, the second Piola-Kirchhoff stress tensor $\underset{\sim}{S}$ will undergo a variation

$$d\underset{\sim}{S} = \dot{\underset{\sim}{S}}\, dt \tag{2.153}$$

in the same time interval, where the second Piola-Kirchhoff stress rate $\dot{\underset{\sim}{S}}$ can be written in terms of the Green strain rate $\dot{\underset{\sim}{E}}$ as

$$\dot{\underset{\sim}{S}} = \frac{\partial \underset{\sim}{\Psi}}{\partial \underset{\sim}{E}} \;:\; \dot{\underset{\sim}{E}}. \tag{2.154}$$

The equivalent expression to (2.153) in index notation can be written using Einstein summation convention as

$$\dot{S}^{\,i}{}_{j} = \frac{\partial \Psi^{\,i}{}_{j}}{\partial E_{\,\alpha\beta}}\, dE_{\,\alpha\beta}. \tag{2.155}$$

As it was shown above, the Green strain tensor $\underset{\sim}{E}$ and the infinitesimal Biot strain tensor $\underset{\sim}{\mathcal{E}}$ on the one hand, and the second Piola-Kirchhoff stress tensor $\underset{\sim}{S}$ and the Cauchy stress tensor $\underset{\sim}{\sigma}$ on the other hand are indistinguishable from each other in the framework of the infinitesimal deformation theory. In this case, equations (2.143) and (2.154) will give essentially equivalent results. The strain rate and stress rate concepts enable an alternative incremental approach for solving the elastic problem. Thus, to get the solution to the elasticity problem at time $t + dt$ from the solution at time t by means of a Computational Engineering method, the following steps can be carried out:

1. The values of the nodal displacements rate $\dot{\bar{u}}^{\text{ip}}(t)$ are considered as unknowns.

2. The displacements rate $\dot{\bar{u}}(\bar{r}_{\text{o}}, t)$ is approximated by taking derivatives in (2.4) as

$$\dot{\bar{u}}(\bar{r}_{\text{o}}, t) \approx \dot{\bar{u}}^{h}(\bar{r}_{\text{o}}, t) = \sum_{\text{ip}=1,\text{np}} \dot{\bar{u}}^{\text{ip}}(t)\ \phi_{\text{ip}}(\bar{r}_{\text{o}})\ +\ \dot{\bar{u}}^{\Gamma}(\bar{r}_{\text{o}}, t). \tag{2.156}$$

3. The displacement gradient tensor rate $\dot{\underset{\sim}{\underset{\sim}{\mathcal{J}}}}(\bar{r}_{\text{o}}, t)$ is formulated by taking derivatives in (2.21) as

$$\dot{\underset{\sim}{\underset{\sim}{\mathcal{J}}}}(\bar{r}_{\text{o}}, t) \approx \dot{\underset{\sim}{\underset{\sim}{\mathcal{J}}}}^{h}(\bar{r}_{\text{o}}, t) = \left[\frac{\partial}{\partial \bar{r}_{\text{o}}}\ \dot{\bar{u}}^{h}(\bar{r}_{\text{o}}, t)\right] = \sum_{\text{ip}=1,\text{np}} \dot{\bar{u}}^{\text{ip}}(t)\ \left[\frac{\partial}{\partial \bar{r}_{\text{o}}}\ \phi_{\text{ip}}(\bar{r}_{\text{o}})\right] + \left[\frac{\partial}{\partial \bar{r}_{\text{o}}}\ \dot{\bar{u}}^{\Gamma}(\bar{r}_{\text{o}}, t)\right], \tag{2.157}$$

4. The deformation gradient tensor rate $\dot{\underset{\sim}{\mathcal{F}}}(\bar{r}_{\text{o}}, t)$ is formulated by taking derivatives in (2.10) as

$$\dot{\underset{\sim}{\mathcal{F}}}(\bar{r}_{\text{o}}, t) = \dot{\underset{\sim}{\underset{\sim}{\mathcal{J}}}}(\bar{r}_{\text{o}}, t), \tag{2.158}$$

5. The volume expansion factor rate $\dot{\mathcal{F}}(\bar{r}_{\text{o}}, t)$ is formulated by taking derivatives in (2.14) as

$$\mathcal{F}(\bar{r}_{\text{o}}, t) = \frac{\partial}{\partial t}\ \det\big(\underset{\sim}{\mathcal{F}}(\bar{r}_{\text{o}}, t)\big) \tag{2.159}$$

6. The volume expansion factor rate $\dot{\mathcal{F}}(\bar{r}_{\text{o}}, t)$ is formulated by taking derivatives in (2.14) as

$$\mathcal{F}(\bar{r}_{\text{o}}, t) = \frac{\partial}{\partial t}\ \det\big(\underset{\sim}{\mathcal{F}}(\bar{r}_{\text{o}}, t)\big) \tag{2.160}$$

7. The Green strain tensor rate $\dot{\underset{\sim}{E}}(\bar{r}_{\text{o}}, t)$ is formulated as shown in (2.148).

8. The second Piola-Kirchhoff stress tensor rate $\dot{\underset{\sim}{S}}(\bar{r}_{\text{o}}, t)$ is formulated as shown in (2.154).

9. The above information is introduced in the weak form of the equilibrium equation (2.115) at time $(t + dt)$, assuming it is verified at time t.

10. Since all the above formulations are linear, the result is a linear system of equations whose unknowns are precisely nodal displacements rate $\dot{\bar{u}}^{\text{ip}}(t)$. Therefore, solving this linear system will solve the problem at this step. A time integration scheme is necessary to proceed beyond this point.

Note that the incremental problem is linear, which is an advantage. In addition, possible inelastic effects can be taken into account when performing steps 6 and 7.

2.2.11 Creep

Creep is the viscous deformation in the form of slow flow that some solid materials undergo when subjected to stress.The deformation due to creep is inelastic, since it is permanent. The COMSOL creep model used to perform the analysis is the so-called Norton Law. As it will be explained in more detail below, this creep model takes the form

$$\dot{\mathcal{E}}_{cr}(\bar{r}_o, t) = \alpha(\bar{r}_o, t)\ \underset{\sim\sim}{\sigma}_d(\bar{r}_o, t), \tag{2.161}$$

where $\underset{\sim\sim}{\sigma}_d$ is the deviatoric part of the Cauchy stress tensor, and α is a parameter that depends on several properties of the material, including its temperature and the value of the Von Mises stress at the given point.

Equation (2.137) describes how the inelastic strain tends to evolve with time. However, the time derivative of the strain at the given point will not necessarily match the value of the right-hand side of this equation. The reason is that the particle in which vicinity creep occurs is not isolated, but surrounded by more material or constrained by boundary conditions. Therefore, the creep described by equation (2.137) will be counteracted by a readjustment of the stresses, which will also contribute to the strain value.

According to the incremental deformation theory, the relation between a material vector at time t and the same material vector at time $(t+dt)$ is given by expression (2.71) as

$$\delta\bar{r}|_{t+dt} = \overbrace{\left(\underset{\sim}{\mathcal{I}} + \underset{\sim}{\ell}\,(\bar{r}_o, t)\ dt\right)\ \delta\bar{r}|_t}^{\text{differential relative deformation}} + \mathcal{O}(\|\delta\bar{r}_o\|^2), \tag{2.162}$$

where the velocity gradient tensor $\underset{\sim}{\ell}\,(\bar{r}_o, t)$ is given by expression (1,2,3,4) as

$$\underset{\sim}{\ell}\,(\bar{r}_o, t) = \dot{\underset{\sim}{\mathcal{F}}}(\bar{r}_o, t)\ \underset{\sim}{\mathcal{F}}^{-1}(\bar{r}_o, t) \tag{2.163}$$

It is assumed that after each increase in creep deformation there will be an elastic readjustment of the deformation. Taking into account (2.100), the combination of both effects can be written as

$$\left(\underset{\sim}{\mathcal{I}} + \underset{\sim}{\ell}\,(\bar{r}_o, t)\ dt\right) = \left(\underset{\sim}{\mathcal{I}} + \underset{\sim\sim}{\ell_{el}}(\bar{r}_o, t)\ dt\right)\ \left(\underset{\sim}{\mathcal{I}} + \dot{\mathcal{E}}_{cr}(\bar{r}_o, t)\ dt\right) \tag{2.164}$$

Also, from (2.164) and taking into account (2.101) it is immediately clear that

$$\underset{\sim}{\ell}\,(\bar{r}_o, t) = \underset{\sim\sim}{\ell_{el}}(\bar{r}_o, t) + \dot{\mathcal{E}}_{cr}(\bar{r}_o, t). \tag{2.165}$$

Substituting (2.165) in (2.163) and Solving the deformation gradient tensor rate $\dot{\underset{\sim}{\mathcal{F}}}(\bar{r}_o, t)$ gives

$$\dot{\underset{\sim}{\mathcal{F}}}(\bar{r}_o, t) = \overbrace{\underset{\sim\sim}{\ell_{el}}(\bar{r}_o, t)\ \underset{\sim}{\mathcal{F}}(\bar{r}_o, t)}^{\text{elastic part}} + \overbrace{\dot{\mathcal{E}}_{cr}(\bar{r}_o, t)\ \underset{\sim}{\mathcal{F}}(\bar{r}_o, t)}^{\text{inelastic part}}. \tag{2.166}$$

In essence, the above expression shows that the deformation gradient tensor rate is composed of two parts: an elastic part, which gives rise to a stress rate and is reversible, and an inelastic part, which is due to creep and is permanent.

Therefore, the part of the deformation gradient tensor rate $\dot{\underset{\sim}{\mathcal{F}}}(\bar{r}_o, t)$ that gives rise to a stress rate can be written as

$$\left(\dot{\underset{\sim}{\mathcal{F}}}(\bar{r}_o, t)\right)_{el} = \underset{\sim}{\ell_{el}}(\bar{r}_o, t)\ \underset{\sim}{\mathcal{F}}(\bar{r}_o, t) = \dot{\underset{\sim}{\mathcal{F}}}(\bar{r}_o, t) - \dot{\mathcal{E}}_{cr}(\bar{r}_o, t)\ \underset{\sim}{\mathcal{F}}(\bar{r}_o, t). \tag{2.167}$$

Consequently, to take creep into account in the incremental approach outlined in the previous section, it is sufficient to use the correction (2.168) when evaluating the expression (2.148), in the sixth step.

An alternative to the previous approach is to decompose the deformation gradient tensor at each time t in the multiplicative form

$$\underset{\sim}{\mathcal{F}}(\bar{r}_o, t) = \underset{\sim}{\mathcal{F}_{el}}(\bar{r}_o, t)\underset{\sim}{\mathcal{F}_{inel}}(\bar{r}_o, t), \tag{2.168}$$

being

$$\underset{\sim}{\mathcal{F}_{inel}}(\bar{r}_o, t + dt) = \left(\underset{\sim}{\mathcal{I}} + \dot{\mathcal{E}}_{cr}(\bar{r}_o, t)\ dt\right)\ \underset{\sim}{\mathcal{F}_{inel}}(\bar{r}_o, t). \tag{2.169}$$

The reasoning that justifies the factorization (2.168) consists in proposing that permanent deformations accumulate in the form given by (2.169) while elastic deformations are reversible. Thus at each time step the elastic part of the deformation gradient tensor $\underset{\sim}{\mathcal{F}_{el}}(\bar{r}_o, t)$ is calculated as

$$\underset{\sim}{\mathcal{F}_{el}}(\bar{r}_o, t) = \underset{\sim}{\mathcal{F}}(\bar{r}_o, t)\underset{\sim}{\mathcal{F}_{inel}}^{-1}(\bar{r}_o, t), \tag{2.170}$$

where the inelastic part of the deformation gradient tensor $\underset{\sim}{\mathcal{F}_{inel}}(\bar{r}_o, t)$ must be computed by integrating (2.169) over time. Consequently, to take creep into account in the iterative approach outlined in section 2.2.9, it is sufficient to use the correction (2.170) when evaluating the expression (2.36), in the seventh step.

2.3 Numerical model configuration

In this study, we propose an ellipsoidal cavern shape embedded in a 500 m depth salt deposit. The semi-major axis b is 80 m long and the semi-minor axis a is 37.3 m long, which give us a volume of 1 million m^3. The thickness of the stratum is 400 m, so the top of the cavern is located at a depth of 620 m and the bottom at 780 m. The geometry is shown in Figure 2.1.

A 2D linear elastic axi-symmetric model has been used to solve the solid mechanics problem, taking into account the creep time deformation. Norton's power law with Arrhenius equations has been used for the creep, see equation (2.171).

$$\dot{\varepsilon}_{cr} = A \cdot \left(\frac{\sigma_{eff}}{\sigma_{ref}}\right)^n \cdot exp\left[\frac{-Q}{RT}\right] \tag{2.171}$$

The creep strain rate in equation (2.171) has a dependency on T temperature, A material constant defining a creep-temperature relation (A=3.125×$10^{-6}$$s^{-1}$), $\left(\frac{\sigma_{eff}}{\sigma_{ref}}\right)$ the total uniaxial stress for the respective time, n stress exponent (n=4), Q activation energy (Q=54,000 J mol^{-1}) and R the gas constant (R=8.314 $JK^{-1}mol^{-1}$).

The idea of using this more simplified model is that we are assuming that the response of the cavern to certain long operating cycles is similar or analogous to the responses generated by short operating cycles. In this way, the main objective is to optimise computational time.

The problem is solved using the Finite Element Method with a mesh of 1567 triangular elements, where 109 are edge elements and 7 are vertex elements. The minimum quality of an element is 0.597 and the average is 0.9, see Figure 2.1.

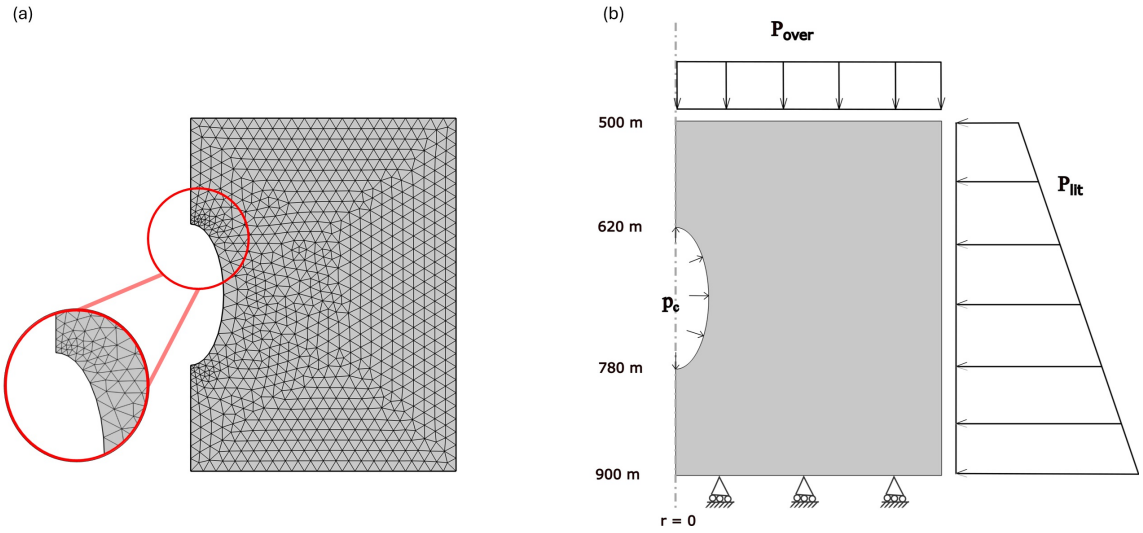

Figure 2.1: *(a) Mesh of the cavern 2D model. (b) Numerical 2D model of the ellipsoidal cavern.*

Initially we supose that the model is static, that means zero displacement and zero velocity.

$$u(t=0)=0 \qquad \frac{\partial u}{\partial x}(t=0)=0 \tag{2.172}$$

For the boundary conditions we stablish the following, see Figure 2.1:

- At the upper boundary of the model there is a pressure coming from the soil layer, called overburden pressure, P_{over}. It is applied as a linear pressure law of value $P_{over}=\rho_{salt}\cdot g\cdot z$, being ρ_{salt} the density of the rock salt, g the acceleration of gravity and z the depth.

- At the right boundary of the model a trapezoidal pressure law, called lithostatic pressure, P_{lit}, is applied. This law represents the pressures exerted laterally by the soil layers at the depth of the cavern, see Figure 2.1. Its value is obtained in the same way as the P_{over}: $P_{lit}=\rho_{salt}\cdot g\cdot z$.The value of the P_{lit} at the starting depth of the stratum is equal to that of the P_{over}.

- At the lower boundary of the model, a roller condition is applied that allows lateral deformation of the model, while fixing its vertical displacement.

- At the left boundary, excluding the cavity boundary, we define the symmetry condition of the model.

- At the cavity boundary, we define the internal pressure at the cavern, p_c.

The geothermal gradient is taking into account. Its value increases with depth at a rate of 0.03 K/m, from 293.15 K at the surface. The temperature at the top of the cavern will be 311.75 K, and at the bottom it will be 316.55 K.

Operating cycles

The operating cycle consists of four phases, in order: charge, holding at Working Gas Pressure (WGP), discharge and holding at Cushion Gas Pressure (CGP), see the shape of an unitary cycle in Figure 2.2.

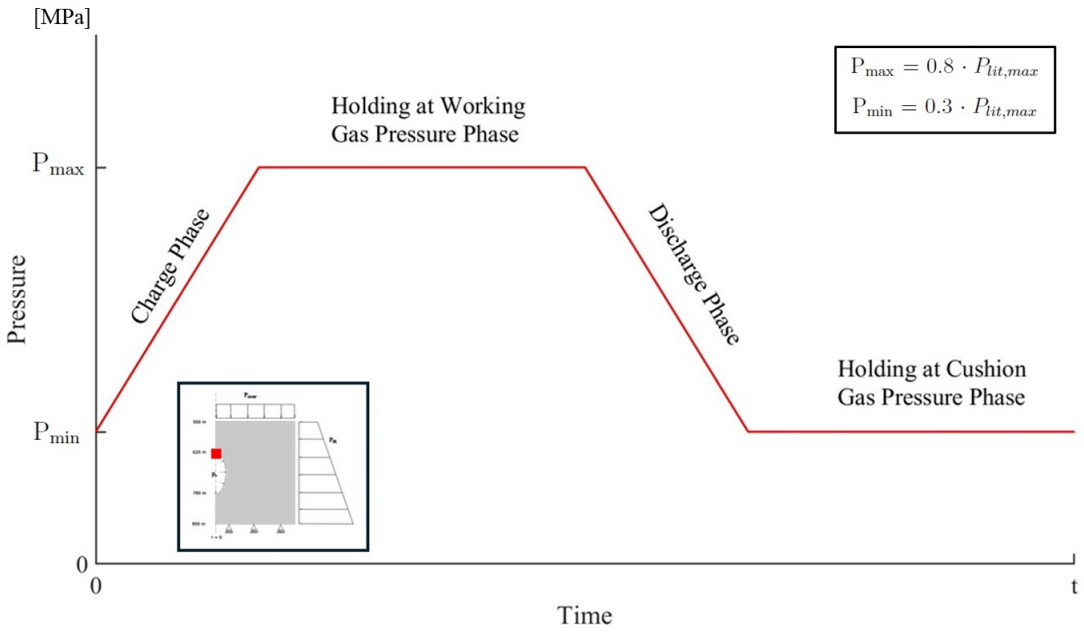

Figure 2.2: *Phases of an unitary operation cycle.*

A single cycle has a complete duration, including all four phases together, of hours, days, weeks, months or years, depending on the purpose to which the underground hydrogen storage is to be applied. Such cycles are repeated over time, affecting the structural integrity and thus the lifetime of the installation. For this reason, it is important to study its design.

The pressure inside the cavern varies over time, depending on the injection/withdrawal cycle. The lower limit of the internal pressure is the cushion gas pressure (CGP), which is limited to the 30% of the maximum lithostatic pressure on the salt layer. The upper limit is the so-called working gas pressure (WGP), which is limited to th 80% of the maximum lithostatic pressure [Ozarslan, 2012]. The WGP has a value of 13.46 MPa and the CGP has a value of 5.05 MPa.

The obtained results will be compared with the response of the cavern to a certain reference cycle, see Figure 3.1. In this cycle, the charge and discharge phases are 20 days long each, and the holding at WGP and holding at CGP phases are 90 days long each as well. The cycles used in this study are presented in Table 2.2.

Analysed phase	Time duration (days)			
	Charge	Holding at WGP	Discharge	Holding at CGP
Charge	40	90	20	90
	60	90	20	90
	80	90	20	90
Holding at WGP	20	68	20	90
	20	45	20	90
	20	23	20	90
Discharge	20	90	40	90
	20	90	60	90
	20	90	80	90
Holding at CGP	20	90	20	68
	20	90	20	45
	20	90	20	23

Table 2.2: *Operating cycles used in the numerical simulations. We define the time duration of each phase for the different phase analysis.*

2.4 Example of application

In this section, the problem to be solved for the validation of the results obtained by numerical simulation is presented. For this purpose, a simplified 3D problem is described, which will be used to compare the results obtained by both methods.

Description

Consist of a circular section pillar composed of halite, see Figure 2.3, with the properties exposed in the Table 2.1. It has a diameter of 1 m and a height of 2 m.

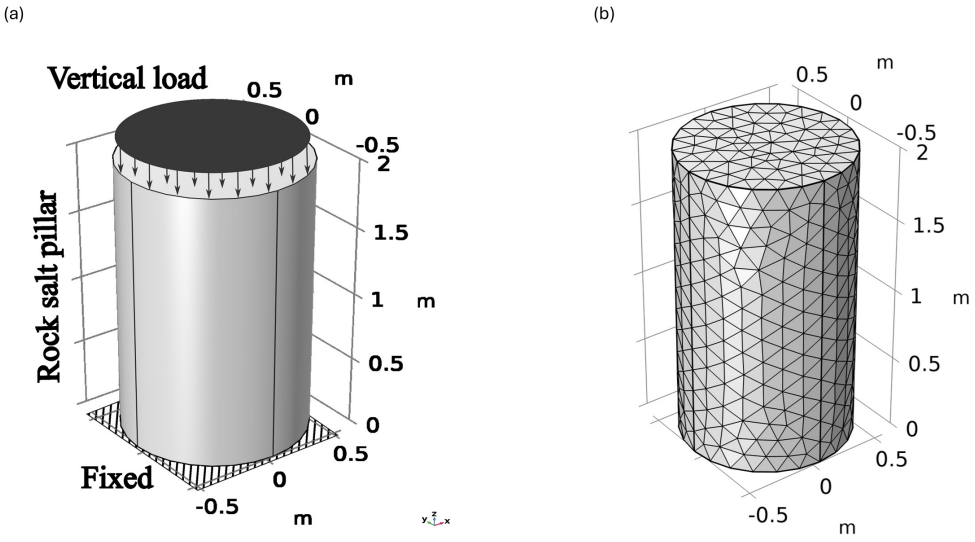

Figure 2.3: *(a) Rock salt pillar 3D model. (b) Rock salt pillar 3D mesh.*

Initially it is assumed static, i.e., zero velocity and zero displacement. As for the boundary conditions, the column is fixed at its base. At the opposite end, a uniform constant pressure is applied throughout the section, see Figure 2.3.

Since the constant pressure is applied in only one direction (Figure 2.3), the formulation can be articulated for a one-dimensional case. This is because the column response will be similar to the one-dimensional one, even though it is a 3D model.

The problem is solved using the Finite Element Method with a mesh of 8255 tetrahedra, where 1020 are triangular elements, 100 are edge elements and 8 are vertex elements. The minimum quality of an element is 0.2687, the average is 0.6681 and the element volume ratio is 0.09486, see Figure 2.3.

For the resolution of the analytical case, the following formulation has been used, where first the deformation relationship is established in equation

$$\varepsilon = \varepsilon_{el} + \varepsilon_{cr} \tag{2.173}$$

Since the response can be assimilated to 1D, the total deformations ε show the following form:

$$\varepsilon = \frac{\Delta L}{L} \tag{2.174}$$

The elastic or recoverable deformation is shown in the equation (2.175) in the form of the simplified Hooke's law

$$\varepsilon_{el} = \frac{\sigma_{eff}}{E} \tag{2.175}$$

where the σ_{eff} will be the value that is varied in the different tests.

As for the creep deformation, it is integrated in time giving as a result the expression

$$\varepsilon_{cr} = \int_{t_0}^{t} \dot{\varepsilon}_{cr} dt = \dot{\varepsilon}_{cr}(t - t_0) \tag{2.176}$$

where we obtain the creep deformation multiplied by the elapsed time t, given that we start from rest $t_0 = 0$. The creep expression results from substituting (2.171) in (2.176).

Therefore, the displacement produced on the top face of the column is obtained by clearing ΔL from the expression (2.174). Then, the equation (2.174) is substituted into that expression (2.173).

$$\Delta L = L\Big[\varepsilon_{el} + \dot{\varepsilon}_{cr} \cdot t\Big] \tag{2.177}$$

The final expression of the displacements results from substituting in (2.177), the equations (2.175) and (2.171).

$$\Delta L = L\Big[\frac{\sigma_{eff}}{E} + A{\cdot}\Big(\frac{\sigma_{eff}}{\sigma_{ref}}\Big)^{n} \cdot exp\Big[\frac{-Q}{RT}\Big] \cdot t\Big] \tag{2.178}$$

In the calculations carried out we have varied σ_{eff} by assigning values of {5,7,9,11,13,15} MPa, being σ_{ref}=1 MPa. To fully define the problem it is necessary to establish a calculation temperature, which has been the one obtained at the top of the cavern T = 311.75 K.

The duration will be five years in total, showing the comparison in shorter periods such as weeks, months and years. The time period t, entered in equation (2.178), must be in seconds.

Analytic vs. Numeric results

For the comparison, the vertical displacement at an upper point of the pillar, is analyzed. A series of calculations have been carried out for a period of five years. Results were taken at the end of one month, one year and at the end of five years, which are presented in Table 2.3. The time evolution of the numerical and analytical solution as a whole for each of the cases of σ_{eff} can be seen in Figure 2.4.

We seek to verify that the numerical model used to obtain the cavern response is valid. This means that if the formulation used by the numerical method, the COMSOL Multiphysics® software [COMSOL AB, 2023], is applied analytically, high convergence results should be obtained.

CASE	σ_{eff}	1 month		1 year		5 years	
		Analytic	Numeric	Analytic	Numeric	Analytic	Numeric
1	5	0.339	0.339	0.443	0.443	0.852	0.852
2	7	0.501	0.501	0.889	0.857	2.578	2.543
3	9	0.695	0.684	1.754	1.680	6.371	5.980
4	11	0.945	0.926	3.308	3.140	13.611	12.700
5	13	1.281	1.250	5.891	5.560	26.044	24.300
6	15	1.734	1.680	9.906	9.300	45.578	42.500

Table 2.3: *Comparison of analytical and numerical results for different σ_{eff} values. The units of σ_{eff} are MPa and the displacements are in mm.*

As can be seen in Table 2.3, the numerical and analytical results have good convergence. The results after a period of one month are identical. The difference between the analytical and numerical results is in hundredths of a millimeter, with the largest difference being 0.054 mm, for values of σ_{eff}= 15 MPa. After the period of one year, the results begin to diverge with greater magnitude, with a difference of 0.606 mm being the largest for σ_{eff}= 15 MPa. In the case of the complete calculation period, differential displacements of 3.078 mm are reached, for the maximum value of σ_{eff}, see Figure 2.4.

As can be seen, as the calculation period increases, as well as the value of σ_{eff}, the results show a growing divergence. This statement is verified in Figure 2.5, where the aforementioned divergence can be seen.

For the lowest values of the σ_{eff} the convergence between results is maintained, while at the highest values the curves begin to separate. As the time range of the response increases, it is seen how the curves increase their separation, reaching the five years with the largest gap in the response.

The finite element mesh has an average element quality of 0.6681 and a minimum element quality of 0.2687. These values refer to the quality of the elements, i.e., if an element has a quality close to 1, it means that this element is optimal. On the other hand, if it is close to 0, it means that the element is very distorted, so the quality is very low.

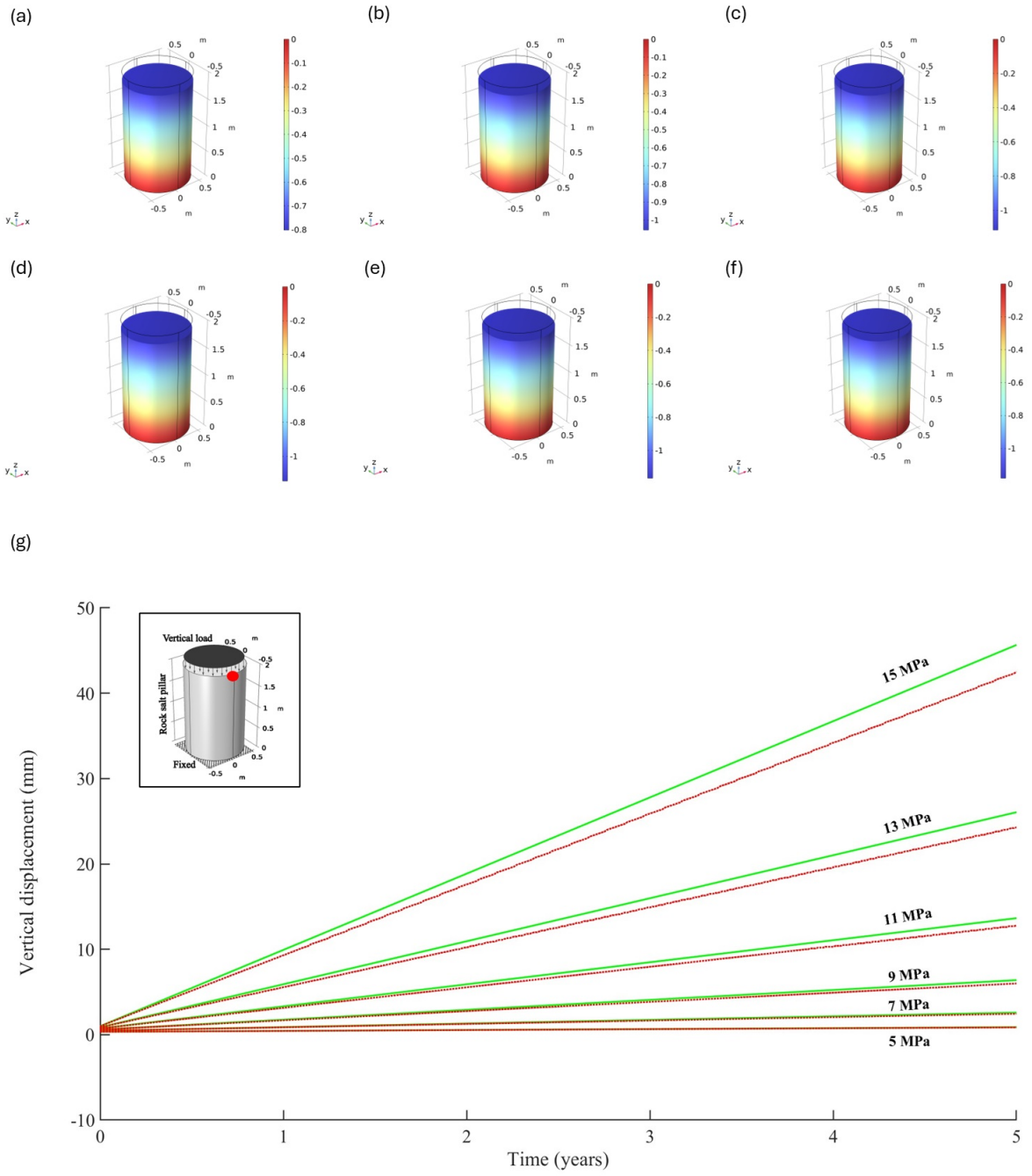

Figure 2.4: *In (a),(b),(c),(d),(e) and (f) we see the response of the salt pillar for an effective stress of 15 MPa for a time period of 0, 1, 2, 3, 4 and 5 years, respectively. In (f) we can see the comparison of the numerical and analytical results for a time period of 5 years.*

The applied mesh causes divergence in the results, Figure 2.4. To solve it, it would be necessary a refinement of the finite element mesh. The mesh used is motivated by the computational cost, since a finer mesh would increase the computational time to a considerable extent.

The gap in the results as presented in Table 2.3 and Figure 2.5 can be expected at higher σ_{eff} values. Since the defined formulation will be applied on a problem with higher

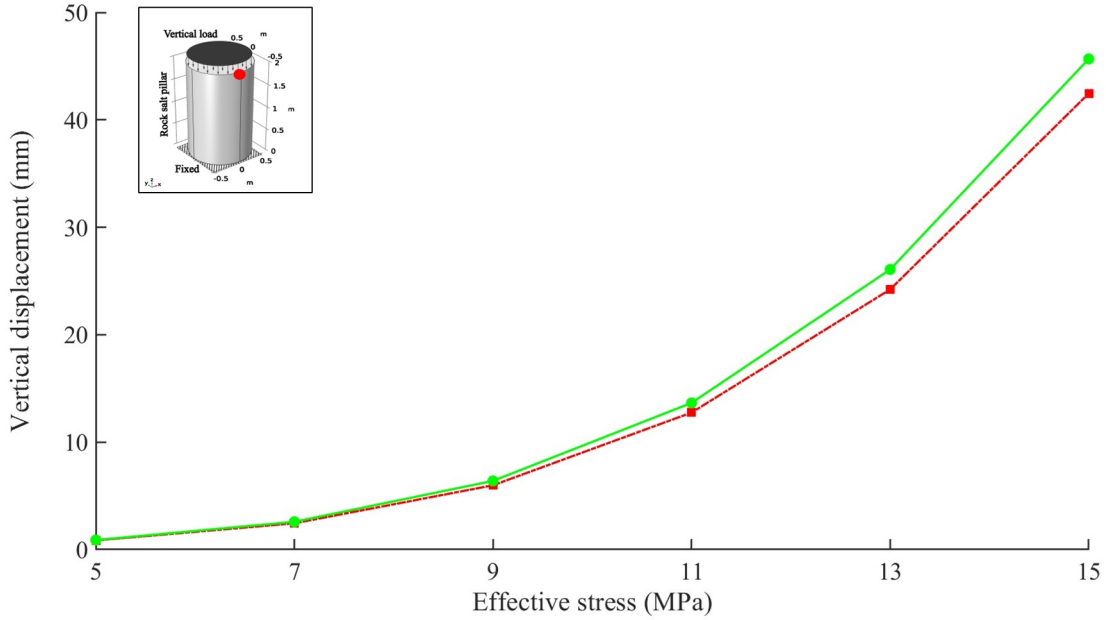

Figure 2.5: *Relationship between effective stress and vertical displacement after a period of five years.*

orders of magnitude dimensions. To summarize, the analytical and numerical results have a good convergence, which verifies the calculations performed and its formulation in the resolution of the solid mechanics problem.

2.5 Conclusions

In this chapter, the numerical model used in the calculations and its formulation have been explained. In particular, the shape and boundary conditions for the modeling of the cavern have been defined, as well as the operating cycles used in the calculations.

The expressed formulation exposes the linear elastic constitutive model used in the numerical simulation, taking into account the time-dependent creep deformation. This formulation has been used in a simplified example to validate the results obtained, which will be presented in later chapters, for the calculation of the cavern response. This example is a pillar made of halite, or salt rock, which has been subjected to a uniaxial load and its response has been obtained through a numerical and analytical analysis.

The comparison shows the validity of the formulation and reinforces the use of numerical simulation when calculating the stability of the cavern. The gap shown in Figure 2.5 could be reduced by mesh refinement and consequently improving the quality of the elements.

Chapter 3

Results and discussion

3.1 Introduction

Among the advantages of using salt caverns for hydrogen storage, we can remark: their low reactivity with hydrogen, which allows it to be recovered from storage with greater purity, and the high watertightness of the salt rock. On the other hand, depending on the depth of the cavern we will need higher storage pressure and a greater amount of cushion gas. For this reason, the structures of the salt caverns have to be analyzed, to optimize their shape and the underground hydrogen storage operations of injection/withdrawal, enabling the maximization of the useful life of the installation and determining the economic viability of this industrial system.

One of the main objectives is to find the conditions for the optimal design of the operating cycles. This working cycles could have a duration of hours, days, weeks, months or years, depending on the purpose of the underground hydrogen storage. For example, if it is a strategic reserve, it will be necessary to design an operational cycle of years. On the other hand, if it is a backup supply for the power grid or as a fuel for the transportation sector, it will be necessary to design an operating cycle of hours.

However, it is important to study the operating cycles to confirm that the safety and stability of the cavern is maintained throughout its useful life, from the point of view of the design prior to its construction.

3.2 Methodology

Another of the main objectives of this study is to test the influence of each of the phases of the operating cycle on the structural stability of the cavern. For this purpose, a series of simulations have been carried out focusing on the vertical displacement at the top of the cavern. This is because both hydrogen injection/extraction operations and cavern construction are performed from this area.

In order to know the influence of the different phases, the simulations shown in Table 2.2 have been carried out. In these simulations, the duration of the phase under analysis is varied in each operating cycle, over a five years period. After the simulation is completed, the response of the cavern to that cycle is obtained. The response of the cavity will be compared with that of a cycle called *reference cycle*, see Figure 3.1. This cycle will consist of a duration of 20 days each for the charge and discharge phases, and a duration of 90

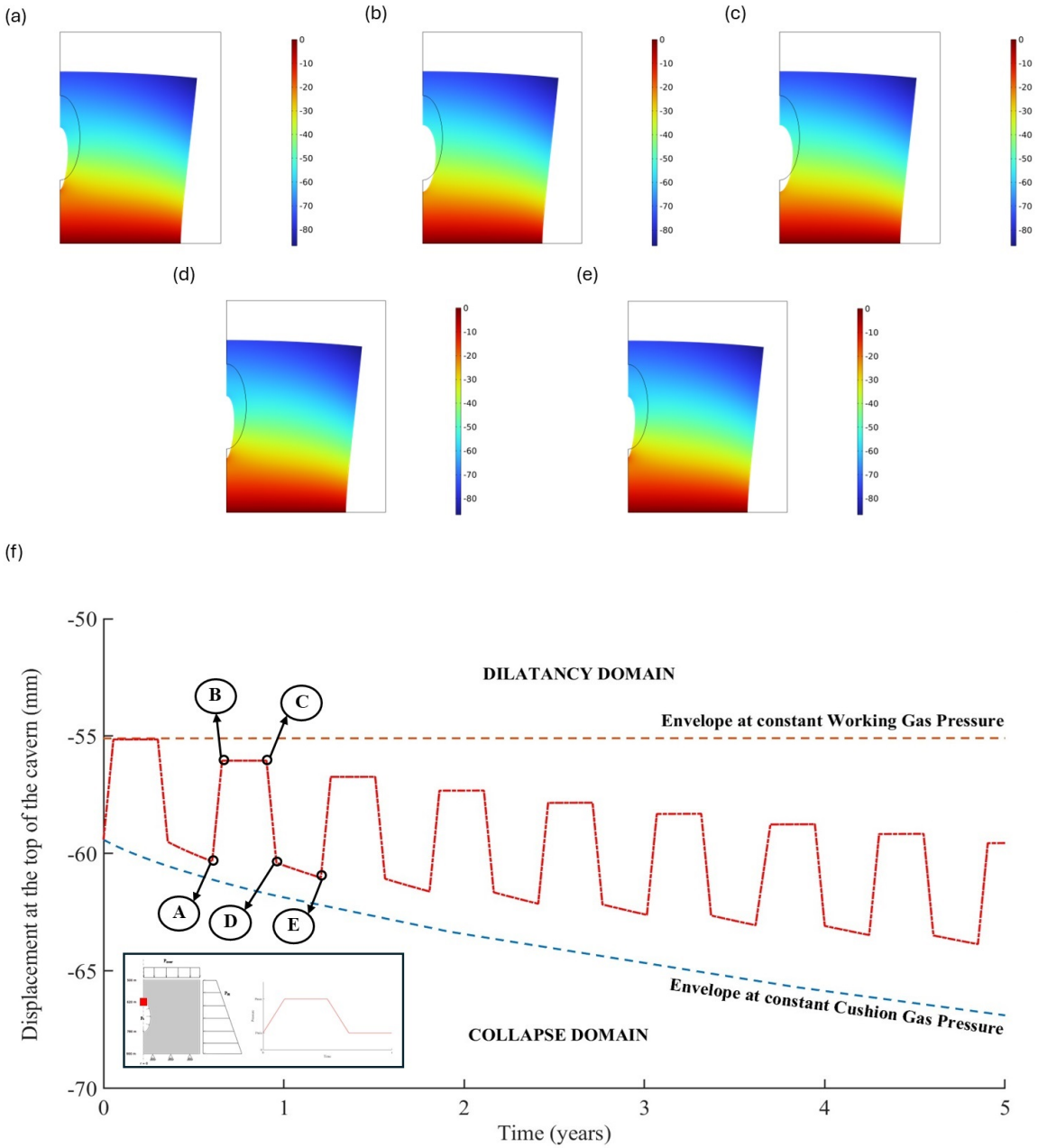

Figure 3.1: *In (a),(b),(c),(d) and (e), we see the plot of the vertical displacement field of the cavity 2D model. Each figure shows the response at the moment marked in (f). In (f) you can see the evolution of the response of the cavern to the reference cycle in a 5 years period.*

days for the holding at Working Gas Pressure (WGP) phase and the same for the holding at Cushion Gas Pressure (CGP) phase. The full time period is 220 days.

The response of the cavern will be limited by the constant WGP envelope and the constant CGP envelope, see Figure 3.1. The first one marks the boundary with the so-called *dilatancy domain* and the second one with the so-called *collapse domain*. This means that if the response envelope of an operating cycle approaches or exceeds the envelope at constant WGP, the halite could fissure and hydrogen losses could occur. On the other hand, if we get too close to or exceed the envelope at constant CGP, the cavern

would lose the necessary sustainability and collapse could occur.

Although both situations seem undesirable, the most unfavorable scenario is the case of approaching the constant CGP envelope. This is because the situation is more unstable and the consequences are more pernicious. Accordingly, in the analysis of results, we will focus on this situation.

3.3 Influence on stability by the phases of operating cycles

3.3.1 Charge phase analysis

The duration of the charge phase has been modified from 20 days at the reference cycle to 40, 60 and 80 days. The complete duration of a single cycle is changed from 220 days to 240, 260 and 280 days. Assuming a maximum increase in duration of 27%, see Figure 3.2.

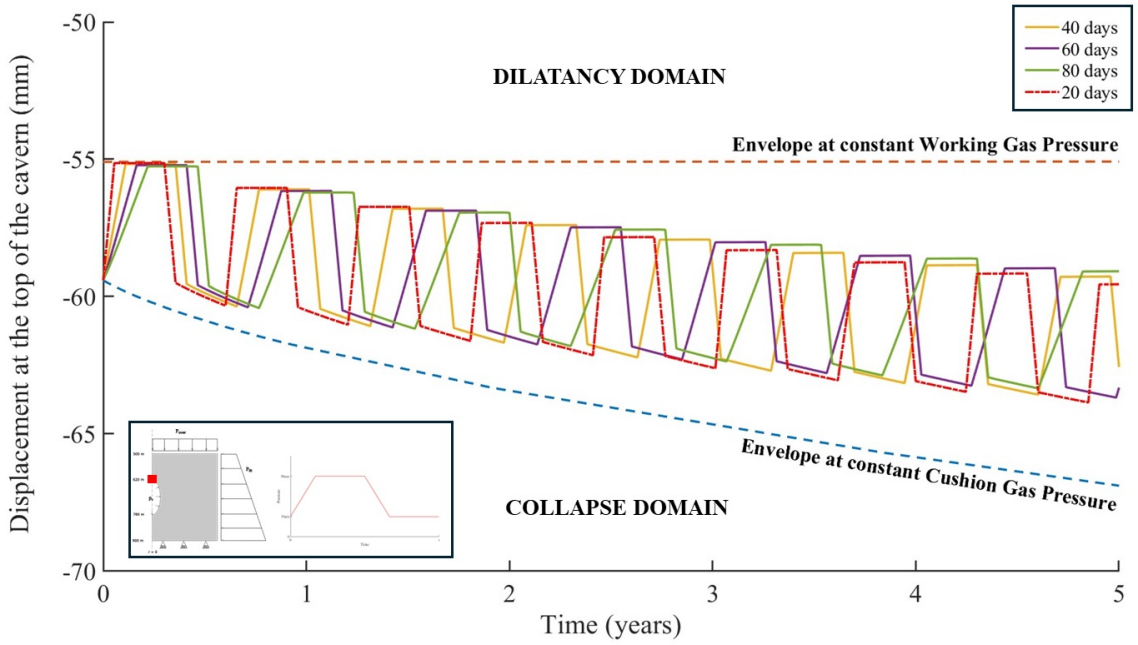

Figure 3.2: *Charge phase analysis. In this figure we can see the comparison of the responses of the new operating cycles where we have changed the time period of the charge phase.*

By making this modification, we begin to see from the outset, the time lag generated in the response of the new operating cycles compared to the reference cycle. The duration of the charge phase increases, so the tendency of the responses moves towards the limit with the dilatancy domain.

It is found that as we extend the duration of the charge phase, the lower envelope of the responses of the different operating cycles separates slightly from the envelope marked by the reference cycle, see Figure 3.2. This means that by modifying the duration of the present phase, we slightly increase the margin that exists with the situation of complete

instability, i.e., the envelope at constant CGP. Although an improvement is shown, it is only slight.

3.3.2 Holding at Working Gas Pressure phase analysis

The duration of the holding at WGP phase has been modified from 90 days at the reference cycle to 68, 45 and 23 days. The complete duration of a single cycle is changed from 220 days to 198, 175 and 153 days. Assuming a maximum decrease in duration of 30%, see Figure 3.3.

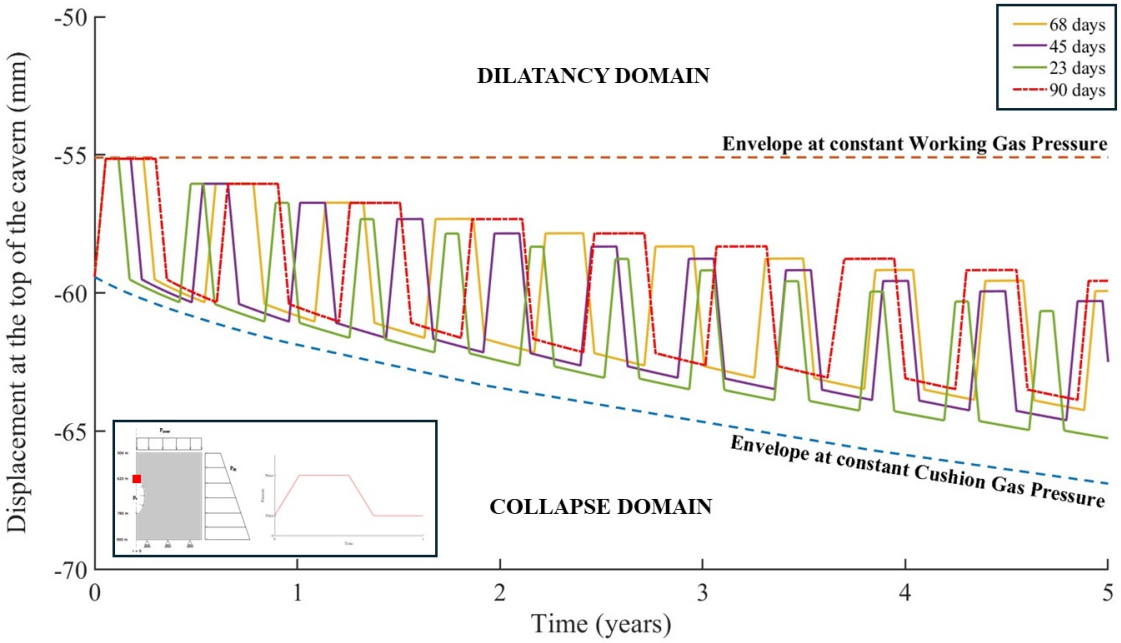

Figure 3.3: *Holding at WGP phase analysis. In this figure we can see the comparison of the responses of the new operating cycles where we have changed the time period of the holding at WGP phase.*

By making this modification, we begin to see from the outset, the time lag generated in the response of the new operating cycles compared to the reference cycle. The duration of the phase decreases, so the tendency of the responses moves towards the limit with the collapse domain.

It is found that as the duration of the phase is reduced, the lower envelope of the response to each cycle becomes increasingly separated from the envelope marked by the reference cycle, see Figure 3.3. This means that by modifying the duration of the present phase, we reduce the margin that exists with the situation of complete instability, i.e., the envelope at constant CGP.

The magnitude of nearing the limit with the collapse domain is very high, so reducing the duration of the holding at WGP in this way can cause serious problems in the useful life of the installation. Even the possibility of the collapse of the cavern.

3.3.3 Discharge phase analysis

The duration of the discharge phase has been modified from 20 days at the reference cycle to 40, 60 and 80 days. The complete duration of a single cycle is changed from 220 days to 240, 260 and 280 days. Assuming a maximum increase in duration of 27%, see Figure 3.4.

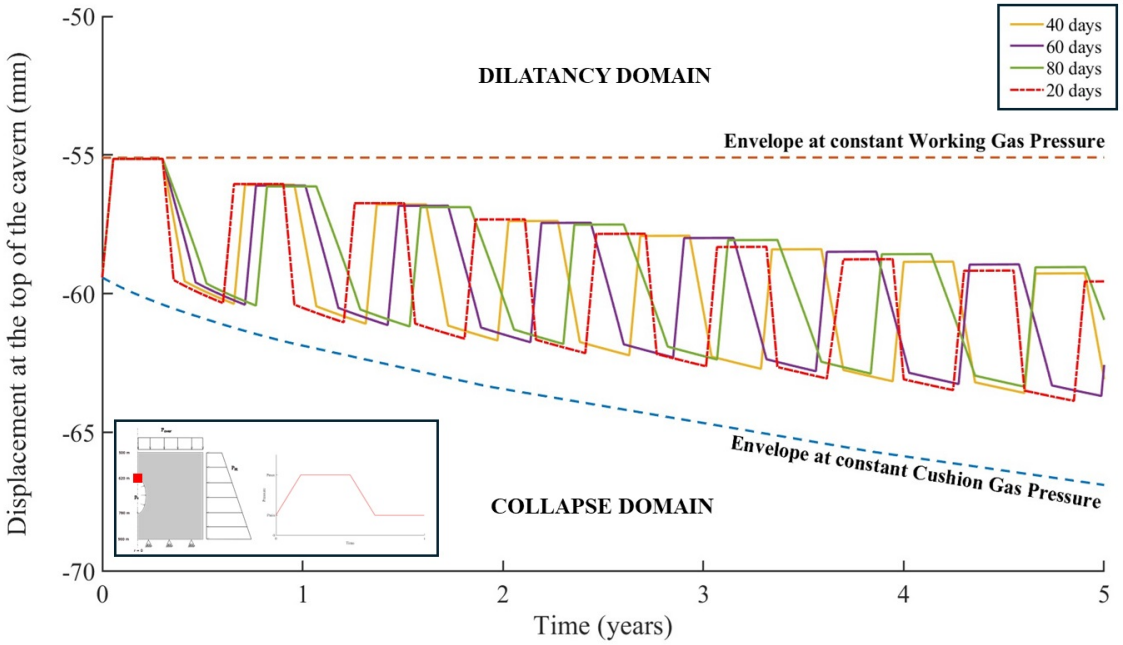

Figure 3.4: *Discharge phase analysis. In this figure we can see the comparison of the responses of the new operating cycles where we have changed the time period of the discharge phase.*

By making this modification, we begin to see from the outset, the time lag generated in the response of the new operating cycles compared to the reference cycle. The duration of the discharge phase increases, so the tendency of the responses moves towards the limit with the dilatancy domain.

As can be seen as the duration of the discharge phase is extended, the lower of the responses of the different operating cycles separates slightly from the envelope marked by the reference cycle, see Figure 3.4. This means that by modifying the duration of the present phase, we slightly increase the margin that exists with the situation of complete instability, i.e., the envelope at constant CGP. Although an improvement is shown, it is only slight. Same behaviour as in the charge phase analysis.

3.3.4 Holding at Cushion Gas Pressure phase analysis

The duration of the holding phase at CGP has been modified from 90 days at the reference cycle to 68, 45 and 23 days. The complete duration of a single cycle is changed from 220 days to 198, 175 and 153 days. Assuming a maximum decrease in duration of 30%, see Figure 3.5.

By making this modification, we begin to see from the outset, the time lag generated in the response of the new operating cycles compared to the reference cycle. The duration

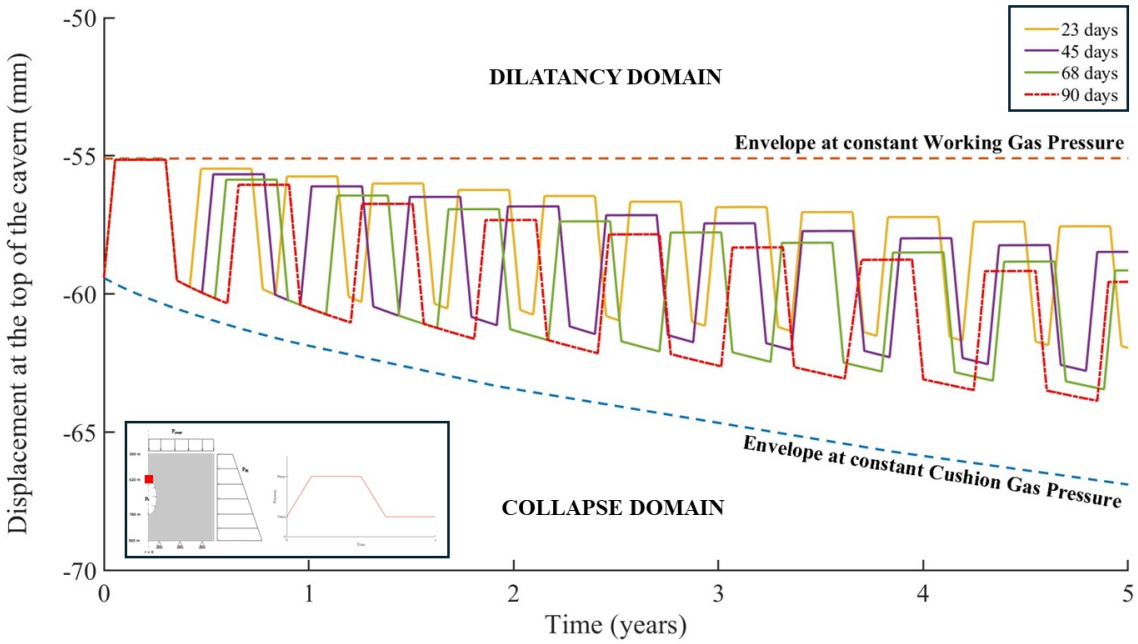

Figure 3.5: *Holding at CGP phase analysis. In this figure we can see the comparison of the responses of the new operating cycles where we have changed the time period of the holding at CGP phase.*

of the phase decreases, so the tendency of the responses moves towards the limit with the dilatancy domain.

It is found that as the duration of the phase is reduced, the lower envelope of the response to each cycle becomes increasingly separated from the envelope marked by the reference cycle, see Figure 3.5. This means that by modifying the duration of the present phase, we increase the margin that exists with the situation of complete instability, i.e., the envelope at constant CGP.

The magnitude of nearing the boundary with the dilatancy domain is very high, so reducing the duration of the holding at CGP phase in this way, benefits the useful life of the installation. If the phase duration is reduced too much, the halite could fissure because the upper envelope of the responses is close to the dilatancy domain.

3.4 Conclusions

In this chapter, the influence of each of the phases that make up the operating cycle on the stability and structural safety of the cavern has been analyzed. It should be remembered that the response of the cavern is obtained through a linear elastic model taking into account creep deformation, i.e., the ultimate strength is not being tested. Optimal service life conditions are sought to increase storage capacity and performance. From the figures presented in section 3.3 the following can be extracted:

- It would be possible to design the operating cycles with the envelopes at constant Working Gas Pressure (WGP) and at constant Cushion Gas Pressure (CGP). But

this would be incorrect because it would underestimate and overestimate the displacements produced.

- The charge and discharge phases have little influence on the deformations during the operating life of the cavern.
- Key to the design of the cavern operation cycles is the duration of the holding at WGP and holding at CGP phases. The change in the duration of these phases is where the biggest differences can be seen.
- It is evident that exists a relationship between the duration of the holding at WGP phase and the holding at CGP phase (3.1). If the ratio remains equal to or greater than 1, we will find that the operating cycle we are working with will have a lower envelope that moves away from the collapse domain, see Figure 3.6.

$$\frac{Time\ at\ WGP\ phase}{Time\ at\ CGP\ phase} \geq 1 \tag{3.1}$$

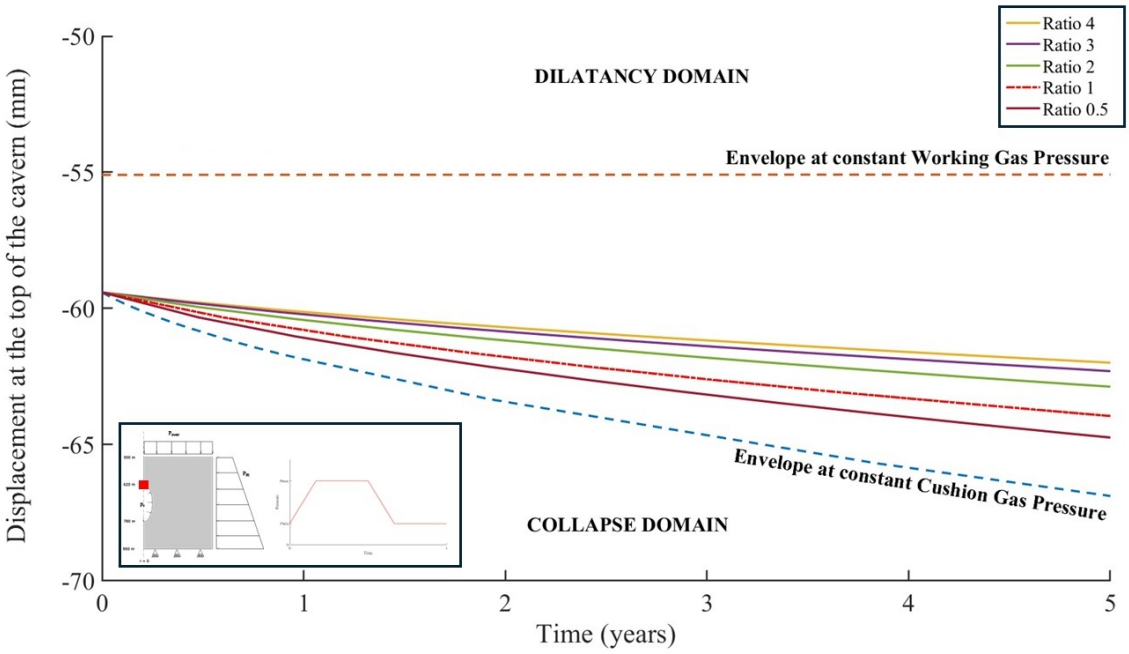

Figure 3.6: *Examples of ratios from expression (3.1). We can see the lower envelope of the responses from those operating cycles.*

As can be seen in Figure 3.6, the lower envelope of the responses is moving away from more unstable situation as we increase the ratio. This confirms the stablished relationship.

- The halite, or salt rock, shows the capacity for self-healing. If there is a period when the cavern is empty for a certain amount of time and immediately when it returns to production, we use the same operating cycle as before this scenario, the storage life will be shortened, as its lower envelope will approach the most unstable

situation. To prevent this from happening, we must fill the cavern to the WGP and keep it filled for the same time as it was empty to recover the level of deformations.

Chapter 4

Conclusions and future research lines

4.1 Introduction

Hydrogen is likely to be the synthetic fuel of the future because of its high calorific value and the possibility of using hydrogen produced from renewable energies. The generation by hydrolysis of water using electricity supplied by renewable energy sources, also known as 'green hydrogen', stands out, which can contribute to changing the global energy model.

Underground hydrogen storage can become a viable option compared to the use of metallic tanks above ground, due to the permeability problems of metallic structures in relation to hydrogen, in addition to the challenges of safety in storage and operations.

In this project, the conditioning and creation of salt caverns have been studied. These can be created by adapting galleries in abandoned salt mines or by building them from the surface through a borehole; this is a possibility due to the low permeability of halite (salt rock). It is expected to efficiently confine hydrogen without leakage.

The mathematical and physical model required for the resolution of the deformable solid problem posed by the study of the stability of a salt cavern has been studied. A numerical model of a cavern of ellipsoidal shape inside a saline stratum at 500 m depth has been proposed. Using COMSOL Multiphysics software [COMSOL AB, 2023], the response of the cavern to different operating cycles has been obtained. The study has focused on the characterization of the influence on the structural stability of each of the phases of the hydrogen injection/extraction cycles.

The conclusions obtained from this work are presented below and possible future reserch lines for its continuation are outlined.

4.2 Conclusions

After what has been exposed in previous chapters of this work, the following conclusions can be drawn:

- Following the results obtained, a rule can be stablished that leads to the optimal design of hydrogen injection/extraction cycles. This rule is shown in the expression (3.1). If we take this design rule into account, we ensure a minimum level of deformations, over the lifetime, far enough away from the collapse domain, see Figure 3.6.

- The phase of the operating cycle that is most detrimental to the integrity of the cavern is the holding at Cushion Gas Pressure (CGP) phase. The lack of gas inside the cavern causes the pressures that keep the cavity walls stable to drop. The longer the time spent in this situation, the shorter the life of the installation.
- It is remarkable the capacity presented by halite for re-healing after being subjected to long periods of low pressures. In this way it is possible to control the deformations or throughout the useful life of the installation.

4.3 Future research lines

Finally, different ideas are put forward that could be carried out in the future based on what has been presented in this project:

- Studies that include volumetric deformation, cavern depth, cavern shape and the distance between other caverns to more accurately design the ratio present in the expression (3.1). This would allow for greater production efficiency.
- Include variables that affect economic-structural performance of the cavern.
- To study more specifically the re-healing capacity of halite. Propose different operating cycles to study its behavior.
- To propose operating cycles that adapt to the hourly energy demand, to define more precisely short cycles and thus be able to design operating cycles with daily applicability.

Bibliography

[AbuAisha and Billiotte, 2021] AbuAisha, M. and Billiotte, J. (2021). A discussion on hydrogen migration in rock salt for tight underground storage with an insight into a laboratory setup. Journal of Energy Storage, 38:102589.

[Alsunousi and Kayabasi, 2024] Alsunousi, M. and Kayabasi, E. (2024). The role of hydrogen in synthetic fuel production strategies. International Journal of Hydrogen Energy, 54:1169–1178.

[Arnold and Sitz, 1984] Arnold, C. and Sitz, P. (1984). Die entwicklung und betriebsführung des stadtgasspeichers im stillgelegten kalisalzbergwerk burggraf-bernsdorf in unterirdische salzkavernenspeicherung. Freiberger Forschungsheft A 699.

[Arnold C. and T., 1998] Arnold C., S. G. and T., F. (1998). Untertägige komplettierung des bergwerksspeichers burggraf-bernsdorf. Erdöl, Erdgas, Kohle, 114:312–316.

[Barták, 1999] Barták, J. (1999). Underground gas storage of haje – pribram. Magazin Tunnel, 2.

[Bauer S. J. and Neal, 1997] Bauer S. J., E. B. L. and Neal, J. T. (1997). Geotechnical studies associated with decommisioning the strategic petroleum reserve facility at weeks island, louisiana: A case history. International Journal of Rock Mechanics and Mining Sciences, 34:3–4.

[Bockris, 2013] Bockris, J. O. (2013). The hydrogen economy: Its history. International Journal of Hydrogen Energy, 38(6):2579–2588.

[Cavendish, 1766] Cavendish, H. (1766). Xix. three papers, containing experiments on factitious air. Royal Society, 56:141–184.

[Colas et al., 2023] Colas, E., Klopries, E.-M., Tian, D., Kroll, M., Selzner, M., Bruecker, C., Khaledi, K., Kukla, P., Preuße, A., Sabarny, C., Schüttrumpf, H., and Amann, F. (2023). Overview of converting abandoned coal mines to underground pumped storage systems: Focus on the underground reservoir. Journal of Energy Storage, 73:109153.

[COMSOL AB, 2023] COMSOL AB (2023). Comsol multiphysics®.

[Crotogino, 2022] Crotogino, F. (2022). 26 - large-scale hydrogen storage. In Letcher, T. M., editor, Storing Energy (Second Edition), pages 613–632. Elsevier, second edition edition.

[Ershadnia et al., 2023] Ershadnia, R., Singh, M., Mahmoodpour, S., Meyal, A., Moeini, F., Hosseini, S. A., Sturmer, D. M., Rasoulzadeh, M., Dai, Z., and Soltanian, M. R. (2023). Impact of geological and operational conditions on underground hydrogen storage. International Journal of Hydrogen Energy, 48(4):1450–1471.

[Foh et al., 1979] Foh, S., Novil, M., Rockar, E., and Randolph, P. (1979). Underground hydrogen storage. final report. [salt caverns, excavated caverns, aquifers and depleted fields].

[for Hydrogen and Technologies, 2003] for Hydrogen, E. C. H. L. G. and Technologies, F. C. (2003). Hydrogen energy and fuel cells: a vision of our future. Office for Official Publications of the European Communities.

[Glamheden and Curtis, 2006] Glamheden, R. and Curtis, P. (2006). Excavation of a cavern for high-pressure storage of natural gas. Tunnelling and Underground Space Technology, 21(1):56–67.

[Jeje et al., 2024] Jeje, S. O., Marazani, T., Obiko, J. O., and Shongwe, M. B. (2024). Advancing the hydrogen production economy: A comprehensive review of technologies, sustainability, and future prospects. International Journal of Hydrogen Energy, 78:642–661.

[Kruck and Rudolph, 2013] Kruck, Crotogino, P. and Rudolph (2013). Assessment of the potential, the actors and relevant business cases for large scale and seasonal storage of renewable electricity by hydrogen underground storage in europe. HyUnder.

[Lankof et al., 2022] Lankof, L., Urbańczyk, K., and Tarkowski, R. (2022). Assessment of the potential for underground hydrogen storage in salt domes. Renewable and Sustainable Energy Reviews, 160:112309.

[Li et al., 2023] Li, D.-P., Liu, W., Fu, P., Li, L., Ban, F.-S., Li, Q.-H., Fan, J.-Y., Jiang, D.-Y., and Zhang, Z.-X. (2023). Stability evaluation of salt cavern hydrogen storage and optimization of operating parameters under high frequency injection production. Gas Science and Engineering, 119:205119.

[Lord et al., 2014] Lord, A. S., Kobos, P. H., and Borns, D. J. (2014). Geologic storage of hydrogen: Scaling up to meet city transportation demands. International Journal of Hydrogen Energy, 39(28):15570–15582.

[Lu, 2010] Lu, M. (2010). Rock engineering problems related to underground hydrocarbon storage. Journal of Rock Mechanics and Geotechnical Engineering, 2:289–297.

[Lubon and Tarkowski, 2020] Lubon, K. and Tarkowski, R. (2020). Numerical simulation of hydrogen injection and withdrawal to and from a deep aquifer in nw poland. International Journal of Hydrogen Energy, 45(3):2068–2083.

[Lysyy et al., 2021] Lysyy, M., Fernø, M., and Ersland, G. (2021). Seasonal hydrogen storage in a depleted oil and gas field. International Journal of Hydrogen Energy, 46(49):25160–25174.

[Moliner et al., 2016] Moliner, R., Lázaro, M., and Suelves, I. (2016). Analysis of the strategies for bridging the gap towards the hydrogen economy. International Journal of Hydrogen Energy, 41(43):19500–19508. The 5th Iberian Symposium on Hydrogen, Fuel Cells and Advanced Batteries (HYCELTEC 2015), 5-8 July 2015, Tenerife, Spain.

[Morris et al., 2019] Morris, L., Hales, J. J., Trudeau, M. L., Georgiev, P., Embs, J. P., Eckert, J., Kaltsoyannis, N., and Antonelli, D. M. (2019). A manganese hydride molecular sieve for practical hydrogen storage under ambient conditions. Energy Environ. Sci., 12:1580–1591.

[Olabi et al., 2021] Olabi, A., saleh bahri, A., Abdelghafar, A. A., Baroutaji, A., Sayed, E. T., Alami, A. H., Rezk, H., and Abdelkareem, M. A. (2021). Large-vscale hydrogen production and storage technologies: Current status and future directions. International Journal of Hydrogen Energy, 46(45):23498–23528. Hydrogen Separation, Production and Storage.

[Ozarslan, 2012] Ozarslan, A. (2012). Large-scale hydrogen energy storage in salt caverns. International Journal of Hydrogen Energy, 37(19):14265–14277. HYFUSEN.

[Panfilov, 2010] Panfilov, M. (2010). Underground storage of hydrogen: In situ self-organisation and methane generation. Transport in Porous Media, 85:841–865.

[Panfilov, 2016] Panfilov, M. (2016). 4 - underground and pipeline hydrogen storage. In Gupta, R. B., Basile, A., and Veziroğlu, T. N., editors, Compendium of Hydrogen Energy, Woodhead Publishing Series in Energy, pages 91–115. Woodhead Publishing.

[Pangborn and Gregory, 1976] Pangborn, J. and Gregory, D. (1976). Hydrogen energy technology—update 1976. International Journal of Hydrogen Energy, 1(3):331–340.

[Pfeiffer and Bauer, 2015] Pfeiffer, W. T. and Bauer, S. (2015). Subsurface porous media hydrogen storage – scenario development and simulation. Energy Procedia, 76:565–572. European Geosciences Union General Assembly 2015 - Division Energy, Resources and Environment, EGU 2015.

[Salmachi et al., 2024] Salmachi, A., Seyfaee, A., Robert, R. J., Hosseini, T., Nathan, G., Ashman, P., Roberts, A., Jafarian, M., and Simon, C. (2024). Underground hydrogen storage: Integrated surface facilities and fluid flow modelling for depleted gas reservoirs. International Journal of Hydrogen Energy, 50:1055–1069.

[Schlapbach and Züttel, 2001] Schlapbach, L. and Züttel, A. (2001). Hydrogen-storage materials for mobile applications. Nature, 414:353–358.

[Suárez Alcántara, 2019] Suárez Alcántara, K. (2019). Un poco de todo sobre el hidrógeno. ciencia, 70:72–80.

[Talman, 2015] Talman, S. (2015). Subsurface geochemical fate and effects of impurities contained in a co2 stream injected into a deep saline aquifer: What is known. International Journal of Greenhouse Gas Control, 40:267–291. Special Issue commemorating the 10th year anniversary of the publication of the Intergovernmental Panel on Climate Change Special Report on CO2 Capture and Storage.

[Tarkowski, 2019] Tarkowski, R. (2019). Underground hydrogen storage: Characteristics and prospects. Renewable and Sustainable Energy Reviews, 105:86–94.

[Thiyagarajan et al., 2022] Thiyagarajan, S. R., Emadi, H., Hussain, A., Patange, P., and Watson, M. (2022). A comprehensive review of the mechanisms and efficiency of underground hydrogen storage. Journal of Energy Storage, 51:104490.

[Ugarte and Salehi, 2021] Ugarte, E. R. and Salehi, S. (2021). A Review on Well Integrity Issues for Underground Hydrogen Storage. Journal of Energy Resources Technology, 144(4):042001.

[Valle-Falcones et al., 2022] Valle-Falcones, L. M., Grima-Olmedo, C., Mazadiego-Martínez, L. F., Hurtado-Bezos, A., Eguilior-Díaz, S., and Rodríguez-Pons, R. (2022). Green hydrogen storage in an underground cavern: A case study in salt diapir of spain. Applied Sciences, 12(12).

[Weast, 1976] Weast (1976). Handbook of chemistry and physics, 57th edn. Chemical Rubber Co., Boca Raton.

[WNA, 2020] WNA (2020). World nuclear association. Accessed on July 9, 2024.

[Zivar et al., 2021] Zivar, D., Kumar, S., and Foroozesh, J. (2021). Underground hydrogen storage: A comprehensive review. International Journal of Hydrogen Energy, 46(45):23436–23462. Hydrogen Separation, Production and Storage.

[Züttel, 2004] Züttel, A. (2004). Hydrogen storage methods. Naturwissenschaften, 91:157–172.